RELIABLE ACOUSTIC PATH (RAP) TOMOGRAPHY AT THE ALOHA CABLED OBSERVATORY

A THESIS SUBMITTED TO THE GRADUATE DIVISION OF THE UNIVERSITY OF HAWAI‘I AT MĀNOA IN PARTIAL FULFILLMENT OF THE REQUIREMENTS FOR THE DEGREE OF

MASTER OF SCIENCE

IN

OCEAN AND RESOURCES ENGINEERING

DECEMBER 2017

By

Vincent Varamo

Thesis Committee:

Bruce Howe, Chairperson

Eva Nosal

Zhenhua Huang

Acknowledgments

I would like to thank the Office of Naval Research for funding the project *Acoustics at Station ALOHA: RAP Tomography* under award N000141512091. I also would like to thank my thesis advisor Bruce Howe for making my studies at UH Manoa possible and all the help he provided through the years.

Abstract

Using a mobile ship platform (R/V *Kilo Moana*) with an acoustic source transmitting to a fixed bottom hydrophone at the ALOHA Cabled Observatory (ACO), we are investigating the feasibility of Reliable Acoustic Path (RAP) Tomography. This will allow the spatial mapping of a path integrated sound speed (temperature) over a 60 km diameter "teacup" volume of the ocean. This can be considered an extension of an inverted echosounder (from a vertical to near horizontal path) combined with the precise positioning and timing of seafloor geodesy, where their noise (sound speed variation) is our signal. As a first step in this pilot project, transmissions were sent using an array of transducers at 3.5 kHz. Receptions at the hydrophone were recorded as the vessel approached and departed from ACO. Actual travel times were compared with estimated travel times that were calculated using CTD measurements. The next test employed user-generated (LFM sweeps and M-sequences) signals and an improved experimental setup to ensure a precise and accurate time of transmission. This experiment provided a more consistent travel time that agreed better with estimated times, when compared to the earlier pilot test. For an upcoming cruise with dedicated ship time, this setup will be used again. The vessel will traverse circular and radial paths around the hydrophone to obtain multiple different acoustic paths in the volume. Subsequent analysis of the data is expected to resolve the tidal cycle at ACO, increase positioning accuracy of the bottom mounted hydrophone, and perform RAP Tomography.

Table of Contents

Page

List of Tables

List of Figures

1. Background

Measuring oceanic properties, dynamics, and overall patterns is an area of research interest for many scientists. There are numerous subfields and specializations, with most the research requiring ample amounts of oceanic data. In the past most, if not all, data were collected on-site (in-situ) often requiring the use of a ship(s) and the labor of scientists. Technology has been helping trend away from these antiquated methods by allowing the autonomous collection of continuous data stream with little to no human interference needed. The goal of this research is to help eventually lead to a path towards this independence, where acoustic sources and receivers can be deployed indefinitely transmitting and collecting data. To get to this point, we have begun by sending shipboard acoustic transmissions down to a hydrophone located on the seafloor; we anticipate the ship being replaced by a robotic autonomous surface vehicle (ASV). The purpose for sending these shipboard acoustic transmissions through the water column is to perform reliable acoustic path (RAP) tomography.

Acoustic signals can take several different pathways from the transmitter to the receiver. For these experiments, an acoustic transmission can be received in a direct path, a bottom-surface bounce, a bottom-surface-bottom-surface bounce, and so on. The reliable acoustic path is the direct path taken, ensuring a minimum loss of energy from attenuation and scattering. Attenuation is the absorption of the acoustic signal as it travels further from the source and the scattering is attributed to the bottom/surface bounces (Medwin 2005). This results in the strongest reception of all possible paths and will be the most accurate/precise for timing purposes. Since the sound speed field of the ocean is fairly uniform and constant, sending an acoustic transmission from the vessel at a specified range and initial launch angle guarantees a direct path arrival at the bottom mounted hydrophone (**Figure 1**).

Ocean acoustic tomography is the spatial mapping of the ocean's sound speed. This is done by recording the travel times along different acoustic ray paths. A simple calculation is made to find the average sound speed for each ray path (distance traveled divided by time). By increasing the number of crossing paths the spatially dependent sound speed field can be resolved using linear inverse theory. Using this technique allows for an indirect measurement of the oceans

temperature variation and to a lesser extent subsurface currents (Munk, Worcester and Wunsch 1995).

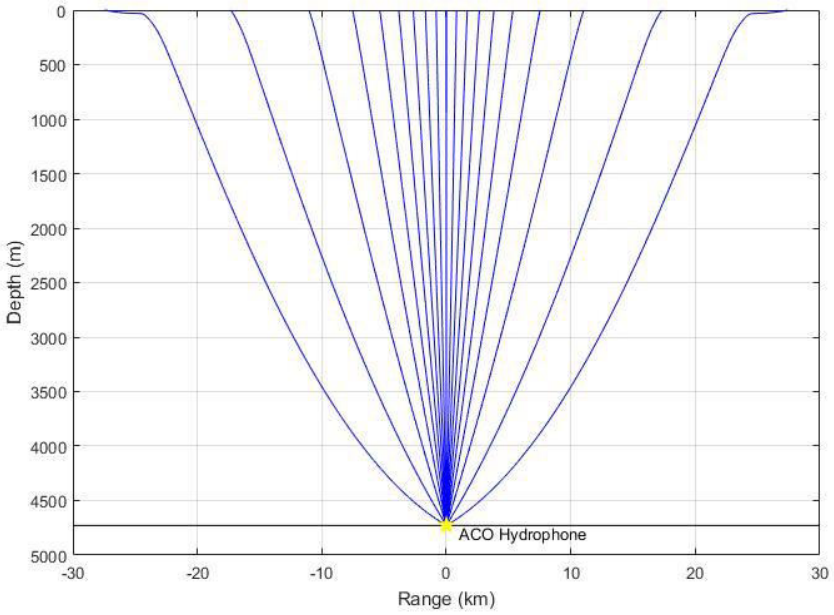

Figure 1. Reliable acoustic paths for ranges extending outwards of ~30 km. Each pathway corresponds to a different initial launch angle and was calculated using August 2015 HOTS CTD (conductivity, temperature, depth) data. The largest launch angle and maximum radius are depicted by the acoustic paths on the left and right that enclose the others. Note: X and Y axis are not scaled equally.

The goal of these experiments is to send acoustic signals up to a 30 km radius (60 km diameter) and map the oceans sound speed of this "teacup" volume (**Figure 1**). The setup of these tests can be considered an extension of the inverted echosounder combined with the precise positioning and timing of seafloor geodesy. An inverted echosounder is a bottom mounted instrument that pings an acoustic signal vertically and records the returning surface bounce to determine the round trip travel time, and thus depth averaged sound speed (temperature). In our case we will have this same vertical ray path (only one-way) and extend this out to a near horizontal ray path when reaching the desired maximum radius. The limiting radius is directly dependent on the water column sound speed field and is theoretically determined using Snell's law. The largest launch angle with respect to the vertical from the transducer that allows a direct path can be used to establish the desired radius (**Figure 1**).

Seafloor geodesy uses an acoustic master and slave to measure seafloor movement over time. One implementation is to measure movement that occurs along a seafloor fault. Acoustic transponders are deployed along each side of the fault line and the master transponder(s) transmits a known signal for which the slave listens for and transmits back to the master after a set time delay (Osada, et al. 2008). Using the round trip travel time helps remove any effect a current may have, because it will cancel out as the ray path moves in both directions (Burgmann and Chadwell 2014). For our project we cannot use this technique, as our signals will only be transmitted from the vessel down to the hydrophone with no return. Fluctuations in this travel time correspond to temperature changes in the acoustic path and is considered noise that needs to be corrected for in the geodesy case (McGuire and Collins 2013). For our purposes, this "noise" is the variable of interest (fluctuations due to water velocity fluctuations is minimal in comparison).

Another geodesy application is to measure absolute plate motion over time. The same technique above cannot be used, since sound speed measurements are only accurate to about +/- 0.05 m/s. The transponders are deployed over large distances and cannot provide the same level of accuracy to provide meaningful data. For this application, transponders are mounted to the seafloor and communicate with a GPS tracked source at the sea surface (Spiess, et al. 1998). The main problem here, similar to our project, is the sound speed variation due to the surface mixed layer. To remove these effects the transponders are spaced out in a circular fashion with a radius of the water depth. This orientation allows the sound speed variation along the water column and subsequent travel time perturbations to cancel out with proper use of the circular geometry. Making these measurements over a span of 24 hours allows for a mean position accuracy of 1.5 cm and over a span of 3-4 days allows for less than 1 cm mean position accuracy (Burgmann and Chadwell 2014). Currently, we do not have the capabilities of positioning the ACO hydrophone with this method, but we can estimate a new position using the acoustic receptions available (see **Section 8**). In future experimentation, provided more GPS surface tracked sources, a similar approach could be taken to the one above.

On a recent and upcoming cruises the R/V *Kilo Moana* will travel to the ALOHA Cabled Observatory (ACO). The first cruise took take place January 22-26 2017. This cruise was part of the Hawaii Ocean Time-Series (HOTS) program that has been conducting near-monthly ocean

measurements at Station ALOHA since 1988. The second cruise will be part of the ACO maintenance operations that plan to use *Lu'ukai*, a remotely operated vehicle (ROV), to help retrieve malfunctioning equipment and deploy new instrumentation (June 2017). While these are their primary goals, it will also be used as a cruise of opportunity for sending shipboard acoustic transmissions down to ACO.

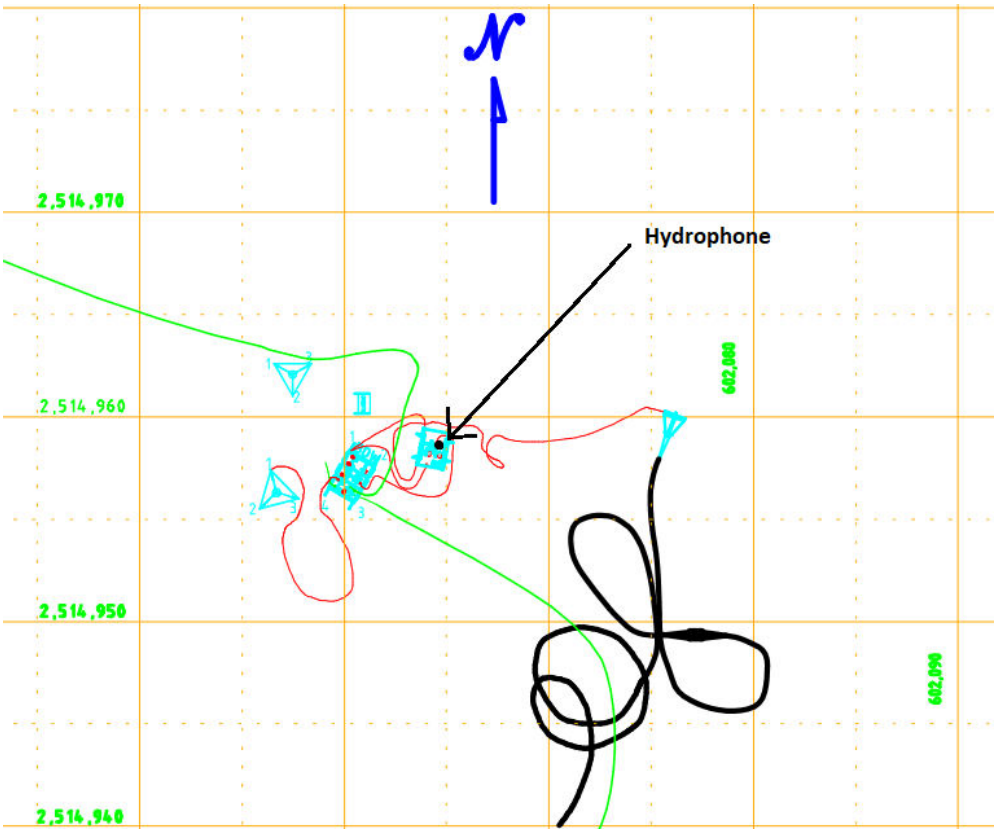

Figure 2. ACO bottom configuration with the current estimated hydrophone position. Estimated position is 22.738894 N 158.006009 W, or UTM zone 4Q 602,064.188 m E 2,514,958.188 m N.

The Aloha Cabled Observatory is located about 100 km north of Oahu, Hawaii (22 45' N, 158 W) at a depth of 4728 m. It was initially deployed in February 2007 with a hydrophone proof module. It is directly connected through a telecommunications cable to a shore station at Makaha. In June 2011, an 8-port node was installed. There is an array of instruments located here including an ADCP, CTD, pressure sensor, fluorometer, and the hydrophone used here that samples at 96 kHz (**Figure 2**).

Figure 3. HEM pressure case that the hydrophone is mounted to; it is inside the PVC case.

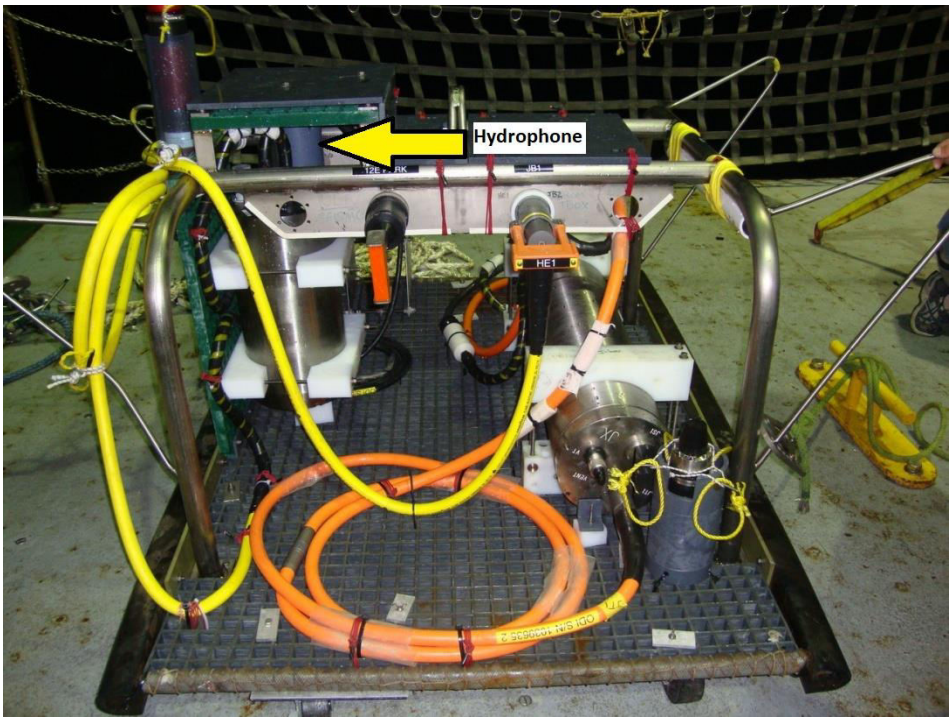

Figure 4. Starboard side view of the Junction Box before deployment. The HEM pressure case is on the left positioned vertically and the hydrophone is under the protective fiberglass gridding.

The hydrophone is mounted to a HEM (hydrophone experiment module) pressure case (**Figure 3**) and this case is placed vertically in the Junction Box frame (**Figure 4**). The Junction Box's (JB) location relative to the other instruments at ACO is given in **Figure 2**. The starboard side of the JB is directed almost due North, so the hydrophone is located near the center of the JB relative to N-S and about 30 cm East.

On the R/V *Kilo Moana* there is a 4x4 transducer array located in a coffer dam on the hull of the ship (**Figure 5**). The transducers were produced by Massa (TR-1075A) and are rated with a 100 Ω impedance at 4kHz. They allow a maximum input of 600 W of power at 30 percent duty cycle or 200 W of power at 100 percent duty cycle (**Appendix B**) (Massa Sonic 2016). According to Massa Sonic, the transducer has approximately a 50 percent efficiency leading to a 195.6 and 190.8 dB re 1 µPa at 1 m, respectively (600 W and 200 W). Previous tests have been conducted using this current setup of transducers (results described in **Section 3 and 4**), but for the upcoming experiments only one transducer will be used.

Figure 5. Housing and interior view of the 4x4 transducer array located on the hull of the R/V *Kilo Moana.* The coffer dam keeps the transducers under water to reduce risk of cavitation and to improve the coupling to the ship's steel hull.

The main goals we seek to accomplish through the experiments will be to resolve a tidal cycle(s) at ACO, estimate a new corrected position for the bottom mounted hydrophone at ACO, and map the sound speed of the ocean surrounding ACO. Resolving a tidal cycle will help ensure the acoustic timing measurements are consistent with sea surface fluctuations to be expected according to known tidal models. Estimating a new hydrophone position will provide more accurate sound speed inversion calculations and help others who use the hydrophone data with a better representation of its position on the seafloor. Finally, mapping the ocean sound speed allows for an indirect measurement of its temperature properties. Provided this mapped sound speed has a detailed resolution, ocean events can be seen and tracked through time. This opens up a possibility of leaving autonomous sources (e.g., mounted on a wave glider)near the sea surface to communicate with the bottom hydrophone(s) and directly monitor the ocean in real-time with no human interaction needed.

Section 2 describes the ACO data acquisition system in which the ACO hydrophone collects and stores the audio data to be analyzed. **Section 3** describes the first experiment conducted onboard the R/V *Kilo Moana* and outlines how an arrival time is determined. **Section 4** looks at the data collected and analyzed for the second experiment as the vessel approached and departed from ACO. **Section 5** describes the details for the current experiment setup and the signals that are being used. **Section 6** goes over the latest experiment conducted and discusses the data collected and analyzed. **Section 7** introduces the sound speed inversion problem in a two-dimensional framework with a sample simulation. **Section 8** looks at the method that will be used for estimating a new hydrophone position in subsequent inversion simulations. **Section 9** continues the sound speed inversion problem and introduces depth dependence into the problem. Then the hydrophone position uncertainty is included to perform an inversion to solve for both the sound speed field and hydrophone position. **Section 10** describes the plan for the upcoming ACO cruise and discusses possible transmission schedules that can be used to achieve future goals of the project.

2. Hydrophone Data

The hydrophone located at ACO provides real-time data to the server at the Makaha cable station and can be streamed live at ACO's webpage. The audio is originally sampled at 96 kHz, but is also digitally filtered to 24 kHz for expedited downloading times for users not interested in the higher frequency acoustics. The data is packaged into 5-minute files and archived for both frequencies.

Each hydrophone data file is usually not exactly 5 minutes, but is typically 5 minutes ± 10 ms in length. For each of the 96 kHz files, 2048 data points are collected and immediately after the last point is stored a time header is created (representing the time of this 2048 data point), and then another 2048 data points are collected. This process (known as FIFO) is repeated until the timing header approaches the end of the 5 minute interval (**Figure 6**). The header contains timing information that is accurate to the sub-microsecond level and is expressed in seconds from January 1, 1970. The 0.1 microsecond precision comes from a 10 MHz time counter that is controlled by a GPS clock which puts out a pulse per second to reset the time counter.

Figure 6. Symbolic representation of the how the hydrophone's 96 kHz data is stored. The blue rectangles correspond to the first 2048 data points collected. The red rectangles represent the headers containing the timing information. The green rectangles correspond to the next 2048 data points collected.

The 24 kHz data files are used in this study and when the 96 kHz are subsampled the placement of the timing headers for the 24 kHz are subsequently changed. For each of these, the timing header is corresponds to and is recorded after the 512th data point is stored and then another 3584 data points are placed after the header. Again, this process is repeated until the timing header nears the 5 minute mark (**Figure 7**).

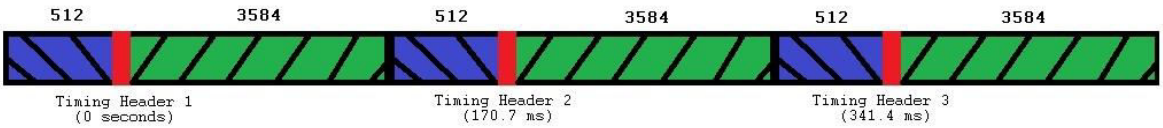

Figure 7. Similar to **Figure 6**, except for the hydrophone's 24 kHz data storage. The blue rectangles correspond to the first 512 data points collected. The red rectangles represent the headers containing the timing information. The green rectangles correspond to the subsequent 3584 data points collected.

For both the 96 kHz and 24 kHz files, the time is linearly interpolated for every data point using the timing headers that bookend that particular section of the dataset. For the data points that come before the first timing header and for the data points that come after the last timing header, the previous and subsequent 5 minute data files must be used to linearly interpolate for these points. When plotting the 96 and 24 kHz together there is a very small lag (~0.05 ms) between the two and was determined using the maximum cross correlation between the two records(**Figure 8**). An infinite impulse response (IIR) filter is used to sub-sample the data and potentially could be the cause of this time lag.

The lag between the 24 and 96 kHz data is consistent throughout each record. So, subtracting 0.05 ms from the 24 kHz timing record will give a true interpretation for the data. **Figure 9** shows the corrected 24 kHz data record overlaid the 96 kHz.

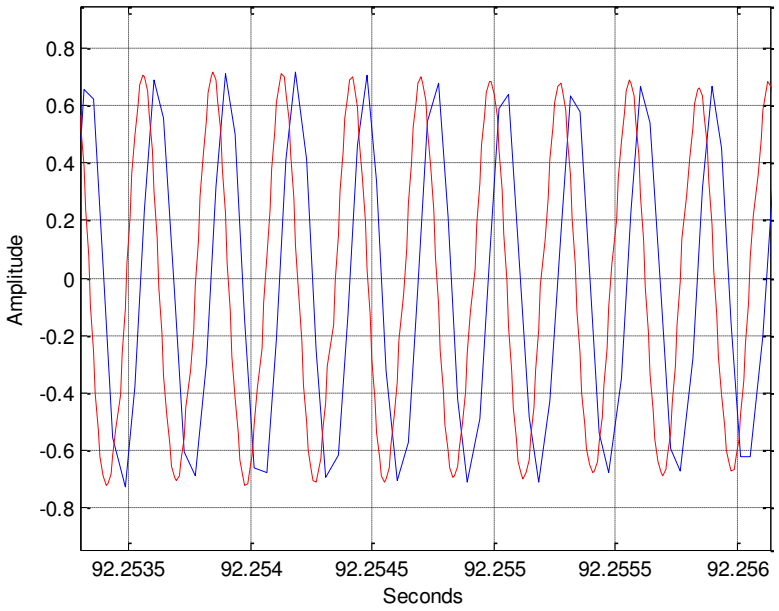

Figure 8. Plot of 96 kHz (red) and 24 kHz (blue) sample of a 3.5 kHz CW acoustic recording taken from September 20, 2015 at 00:35:00 am UTC. The 24 kHz data is lagging relative to the 96 kHz data by approximately 50 μs. The x-axis corresponds to the seconds from the start of the data file and the y-axis represents the amplitude of the signal.

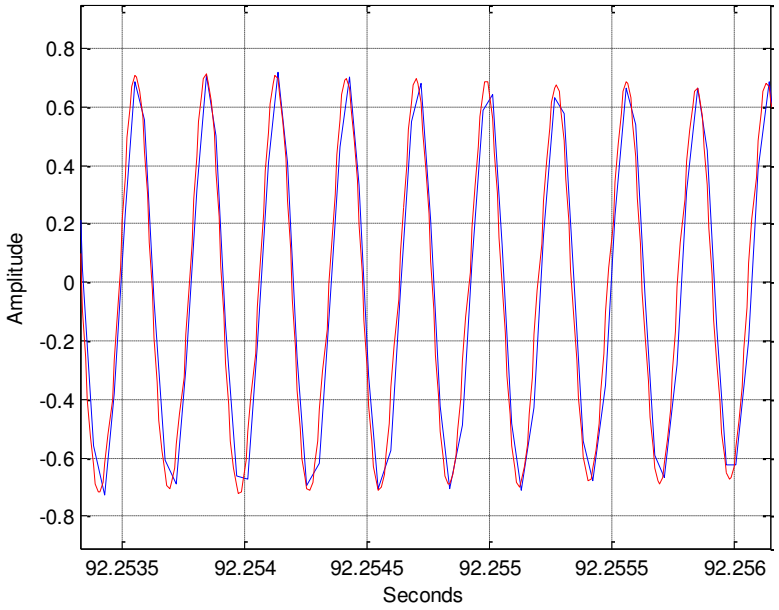

Figure 9. Plot of 96 kHz (red) and time corrected by 50 μs 24 kHz (blue) sample of a 3.5 kHz CW acoustic recording taken from September 20, 00:35:00 am UTC. The x-axis corresponds to the seconds from the start of the data file and the y-axis represents the amplitude of the signal.

3. Preliminary Test Results - First Experiment

Two pilot tests were conducted in the early stages for the RAP tomography project. For both experiments a 4x4 array of transducers were directly connected to a Knudsen Chirp 3260 echosounder. The echosounder is controlled by an onboard software package that includes pre-programmed acoustic signals. There are two allowable frequencies (3.5 kHz and 12 kHz) and two usable waveforms (CW and Chirp). A GPS timing device (Tekron TTM 01-E) was connected to the echosounder to trigger an acoustic transmission on the exact GPS second. The Tekron is programmable to send a pulse to the echosounder at any desired interval. Once the echosounder receives the signal from the Tekron there is a varying small delay to when it ultimately triggers the transducers. Setup is depicted in **Figure 10**.

From September 16-21, 2015, the R/V *Kilo Moana* was set to test and use the ROV (*Lu'ukai*) for the deployment of new instrumentation for ACO. During a period of ROV maintenance, the onboard transducer array and software were tested briefly. During this test the R/V was stationary and located almost directly above the hydrophone (4728 m). Both the continuous waveform (CW) and linear frequency modulated (Chirp or LFM) signals were used. A CW is a signal set to a fixed frequency for its entire duration, and a chirp is a signal that linearly increases from a lower frequency to a higher frequency during its transmission.

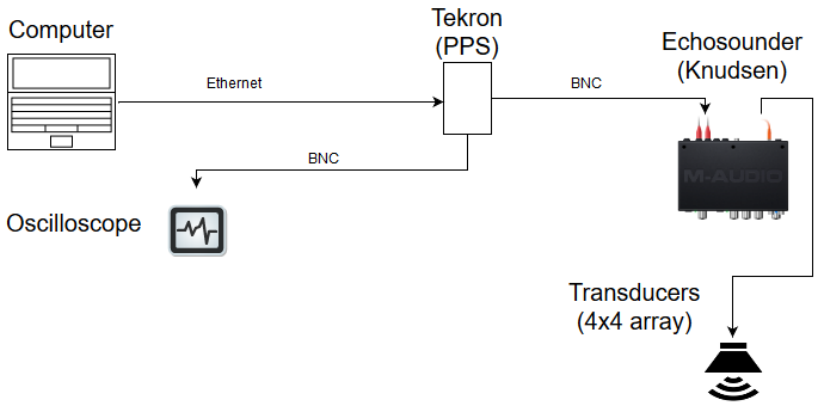

Figure 10. Diagram of the experimental setup for the first two tests conducted using the Knudsen echosounder and 4x4 transducer array.

On September 20, 12:36:05 am, the echosounder onboard the R/V *Kilo Moana* was programmed to transmit a CW tone (or a "simple ping") every 12 s, with a transmission length of 16 ms, and a frequency of 3.5 kHz. The 5 minute data record for 12:35:00 am is plotted in **Figure 11** (the first three receptions pictured are from a separate programmed transmission set and can be ignored).

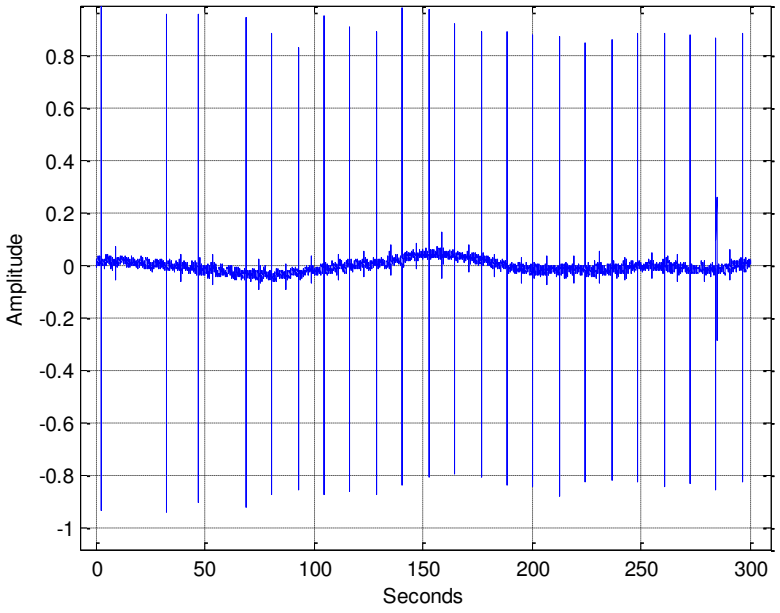

Figure 11. Plot of 5 minute ACO hydrophone data on September 20, 00:35:00 am UTC.

Zooming in on a specific reception (**Figure 12**), the signal appears to be 16 ms and consistent with what was programmed in the software for the onboard echosounder. There is some reverberation, likely due to an interfering bottom bounce and/or leakage after each reception, but it is clear where the initial signal begins and ends for each.

A zero crossing analysis was performed for each reception to determine the tonal frequency. This was done by calculating for a piecewise polynomial using the spline function in MATLAB, providing an equation to calculate the signals amplitude at any point during the reception. With the piecewise polynomial and the fzero function in MATLAB, the times at which there is a zero crossing can be found. The time between every other zero crossing is the period and the inverse of the period corresponds to the frequency (**Figure 13**).

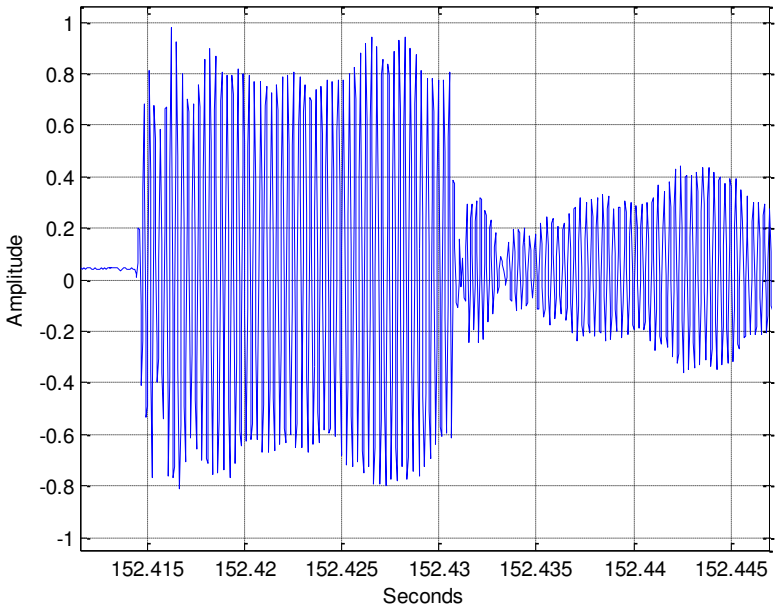

Figure 12. Sample of one CW transmission on September 20 at approximately 00:37:32 am UTC.

The same process shown in **Figure 13** is applied to all receptions and their mean frequency is found at each zero crossing (**Figure 14**). Looking at **Figure 13** and **Figure 14**, the frequencies are much more irregular and jump around substantially near the beginning and end. The frequencies recorded for the middle zero crossings are much more stable and represent the signals received better. The Figures confirm the 3.5 kHz CW that was input into the echosounder onboard.

To find the exact time of a signal's arrival a cross correlation between a replica pulse and the actual arrival is computed. When the cross correlation reaches a maximum value this is the location for the time of arrival (granted the cross correlation peak is sharp enough). Since we do not have the exact waveform the echosounder produces, a replica pulse must be generated (**Figure 15**). The frequency for the replica pulse is a constant 3.5 kHz and confirmed to represent the signal well by the zero crossing analysis.

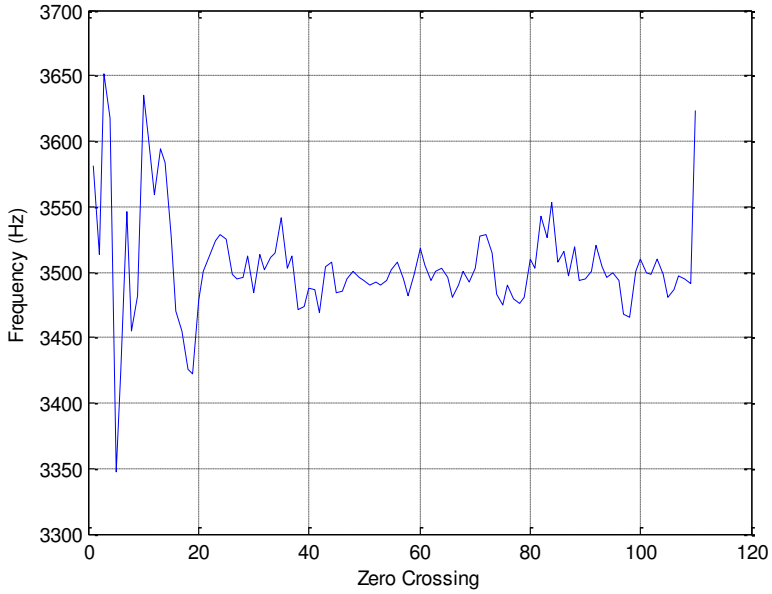

Figure 13. The running frequency for signal received in Figure 9. The x-axis corresponds to the zero crossing number. For a 16 ms pulse at 3.5 kHz the number of zero crossings should be exactly 112.

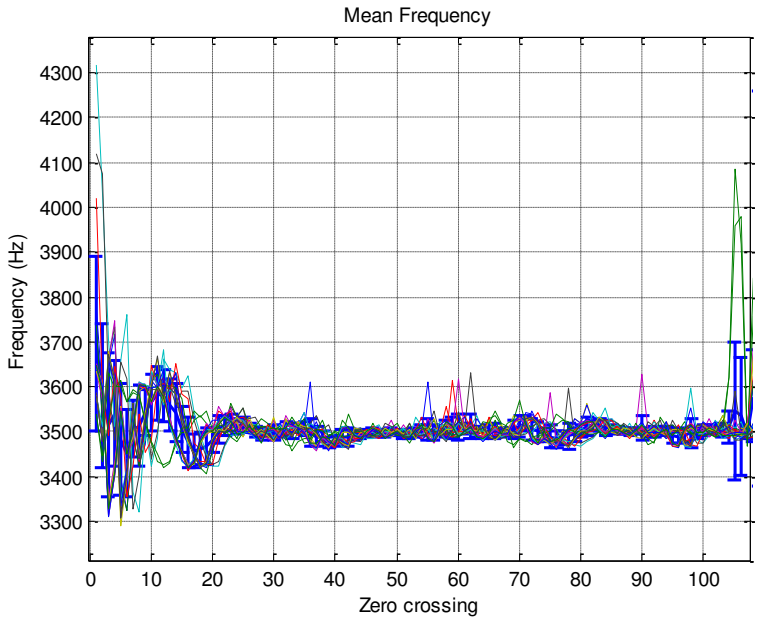

Figure 14. The running mean frequency and standard deviation for all signals received in Figure 5 (blue) overlaid on the individual mean frequencies. The x-axis corresponds to their zero crossing number.

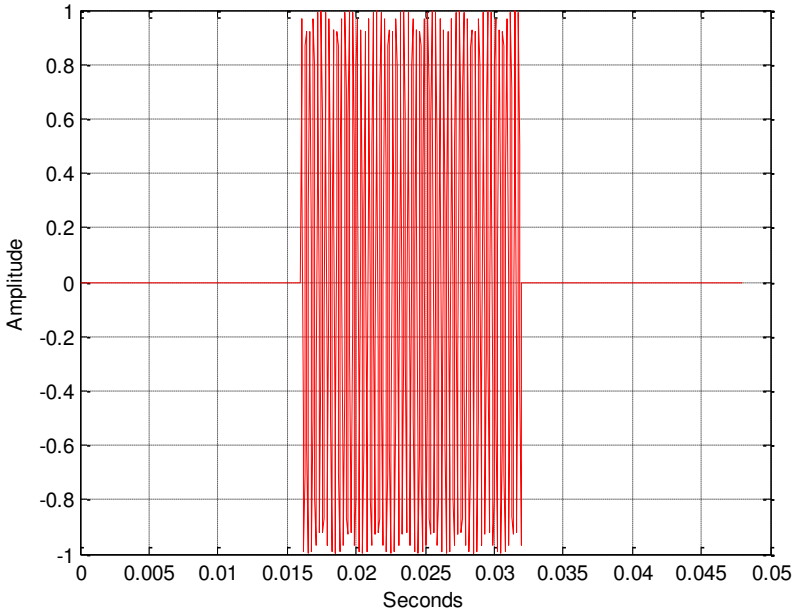

Figure 15. Replica pulse for a CW tone with a pulse length of 16 ms and frequency of 3.5 kHz. Small amplitude variation is due to data points not occurring exactly on the peaks of the cycle.

The replica pulse created in **Figure 15** is used to compute a cross correlation with the data in **Figure 11**. **Figure 16** shows a specific cross correlation between the replica pulse and the acoustic reception in **Figure 12**. The complex demodulation of the cross correlation is also overlaid on the plot and was calculated using the Hilbert transform function in MATLAB. The Hilbert transform returns the analytic signal of the cross correlation, which provides a better representation for the location of the maximum value of the cross correlation. A band-pass filter was not used because it provided no change in estimated travel time or received SNR.

The maximum value of the magnitude of the complex demodulation is used to find the time of arrival for the received signal. Looking at **Figure 16** we find this location and **Figure 17** validates this calculation as we overlay the replica pulse over the reception (at the complex demodulations maximum value) and see they line up very well.

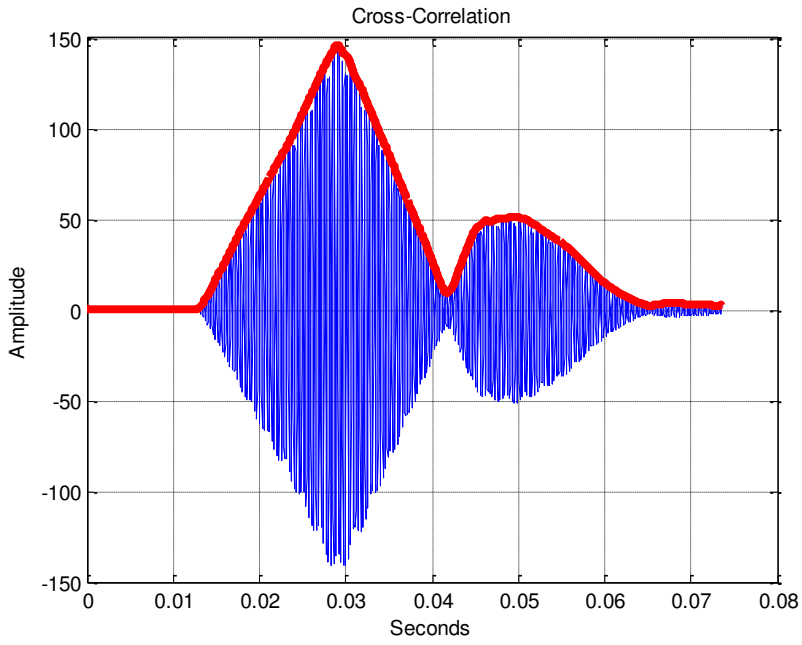

Figure 16. Cross correlation (blue) and its complex demodulation (red) between the replica pulse in Figure 12 and the actual transmission received in Figure 9. The x-axis represents relative seconds, showing the initial triangular peak's length is approximately 32 ms. This is expected because the cross correlation will continue to increase until they match (16 ms) and then decline back to zero (32 ms).

The total travel time of each signal sent from the transducers to the hydrophone is established, now that both the time of acoustic transmission (neglecting the jitter present for the echosounder) and arrival is known. This jitter occurs during the time between when the GPS pulse from the Tekron is received by the echosounder and when the echosounder sends the signal to the transducers below deck (0.4-1.4 ms). These travel times can be compared to estimated travel times calculated using data collected in August 2015 on a HOTS cruise. With CTD casts made nearby ACO a sound speed profile is calculated using the TEOS Gibbs-SeaWater Oceanographic Toolbox (McDougall and Barker 2011). This sound speed profile is then used to estimate an acoustic path and corresponding travel time from the R/V *Kilo Moana* to the hydrophone. The equations used to trace the ray path are given in *Sounds in the Sea* (Medwin 2005) and begin with the ray parameter (a), which is a geometric property of the acoustic ray and depends on the initial launch angle (θ_o) and initial sound speed (c_o). The ray parameter is a constant as the acoustic ray propagates through the water column according to Snell's law.

$$a = \frac{sin\theta_0}{c_0} = constant \quad (1)$$

The ray angle at any depth interval (θ_n) can then be determined by

$$sin\theta_n = ac_n \quad (2)$$

where c_n is estimated from the sound speed profile by the CTD cast. **Equation (3)** is used to determine the ray arc length (s_n) traveled at each depth interval

$$s_n = (z_{n+1} - z_n)tan\theta_n \quad (3)$$

where z_n represents the depth interval. The travel time at each depth interval (t_n) is calculated by

$$t_n = \frac{z_{n+1} - z_n}{c_n cos\theta_n} \quad (4)$$

and the total travel time is the summation over all the depth intervals. A correction needs to be added for the depths and sound speed in **Equations (1)-(4)**. Since we are in a spherical domain, the curvature of the Earth plays a role in ray tracing and subsequent travel times. Using basic Snell's law and assuming a flat Earth is sufficient at small ranges, but becomes significant as you get further away. Two simple equations can be used to correct for this

$$z' = z\left(1 + \frac{z}{R_E} + \frac{z^2}{3R_E^2}\right) \quad (5)$$

$$c' = c\left(1 + \frac{z}{R_E} + \frac{z^2}{R_E^2}\right) \quad (6)$$

where z' and c' represent the corrected depths and sound speeds (Dushaw and Colosi 1998). For example using the sound speed profile from **Figure 35** and **Equations (5)** and **(6)**, at 25 km the travel time will be 7 ms less when taking into account the Earth's curvature compared to assuming a flat Earth. Note: Instrument depths must be converted into the z' notation when computing the sound speeds and time estimations, but are given as their actual depths after these calculations are made.

The R/V *Kilo Moana's* position is tracked using POS MV data collected onboard (**Appendix D**), with the transducers offset from this position to be corrected for. **Figure 18** shows the difference between the actual and estimated travel times for **Figure 11**.

It was concerning that there was such a large discrepancy (~85 ms) between actual and estimated travel times. While the preliminary results do not seem to be accurate, they are precise which gives a good indication that there is a recurring error present when calculating for the acoustic travel times. When looking over error sources and corrections to be made for this experiment setup (**Table 1**) the possible cumulative error is small when compared to the mean error in **Figure 18**. Upon further inspection, it was found that the echosounder is triggered on the falling edge of the pulse provided by the Tekron rather than the leading edge. This pulse width was not recorded for this first test, so it is highly likely that this is the large source of timing error present. For the second test (**Section 4**), the pulse width was 100 ms and is consistent with the error present in that data (we believe it was not changed). For the upcoming experiment this will no longer be an issue due to the change in how we determine the time of acoustic transmission.

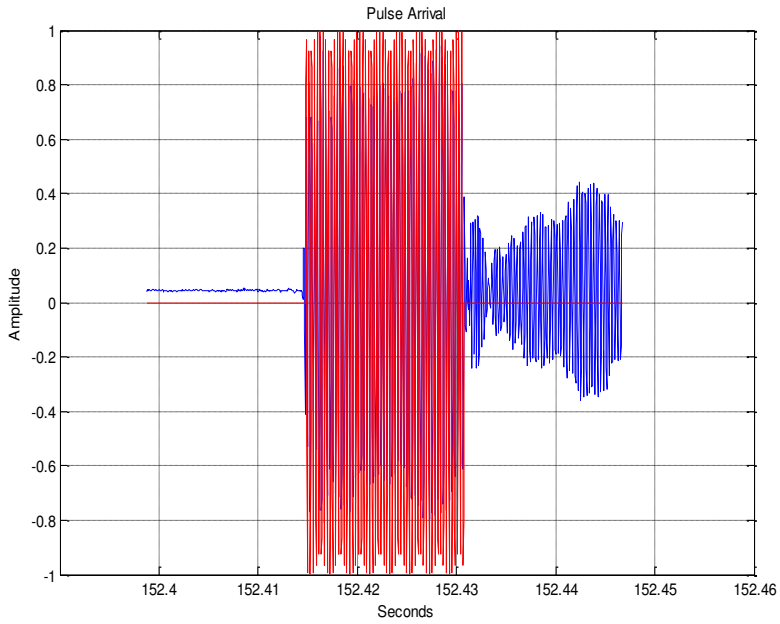

Figure 17. Replica pulse (red) and the actual transmission received (blue). The time of arrival was calculated from the maximum of the complex demodulation in **Figure 16**.

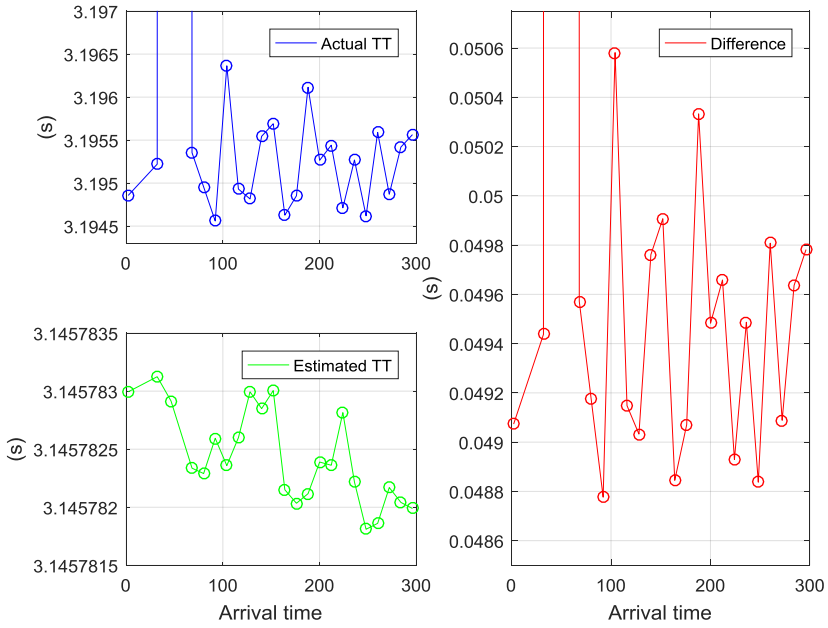

Figure 18. Difference (red) between actual (blue) and estimated (green) travel times. Estimated travel times were calculated from CTD casts taken during a HOTS cruise in August 2015. The third data point can be neglected as this transmission took place in between the setup of the two different transmission cycles described earlier.

Another variable that needs to be taken into account is the sea surface time dependent vertical displacement due to tidal forces. **Figure 20** shows the predicted tide level at ACO for January 2017. The figure shows the spring and neap tides influencing the total sea level change. For this particular month at the peak spring tide the difference between the extreme high and low tide is 0.89 m. Provided the model/prediction given in **Figure 20** is accurate, this would correspond to about a 0.59 ms difference in acoustic travel time between the two extremes.

It is also important to note the seasonal changes the water column at ACO experiences, particularly in the upper mixed layer. This plays a large role in determining what the initial transmitting launch angle was from the transducer that was recorded by the hydrophone (**Figure 19**). When the R/V *Kilo Moana* is at short ranges these small changes in sound speeds will not impact the travel time significantly, but at larger ranges the accuracy of the in situ CTD measurements become increasingly more important for timing.

Similar testing and analysis was completed for the echosounders Chirp signal. It was found that the processing gain received from the Chirp was significantly less than with the CW. Since Knudsen does not provide the exact waveform produced by the echosounder the replica pulse was much harder to replicate in the case for the Chirp. Attempts were even made to use a sample reception as the replica pulse, but the processing gain was still much less than the CW. Being limited to these two signals and given their results, it was decided for the next test to solely use the CW waveform.

Table 1. All sources of error are calculated assuming the R/V *Kilo Moana* is located at the ranges 5, 10, and 25 km. The POS MV position uncertainty (for the preliminary experiments) was approximately 1 m. The time it takes for the echosounder to receive the pulse trigger to when it actually sends the signal to the transducer array varies from 0.4 to 1.4 ms. The location of the transducer relative the POS MV (20.96 m) provides the most error on actual travel time and increases with range. This is only applicable for the preliminary experiments, because the POS MV system now uses a transformed coordinate system to represent the transducers. The hydrophone timing is accurate to 0.1 microseconds using the 10 MHz counter. The travel time precision (**Equation (10)**) assuming a SNR for the ranges to be 25, 20, and 10 dB, respectively, is given for a CW pulse.

	Effect on travel time (ms)		
Errors/Uncertainties for Preliminary Experiments	**5 km**	**10 km**	**25 km**
POS-MV positioning uncertainty (1 m)	0.4893	0.6477	0.6928
Trigger delay inside the echosounder	0.4000 - 1.4000		
Location of transducer relative to POS-MV (20.96 m)	10.1373	13.2749	13.6480
Hydrophone timing	0.0001		
Travel time precision (pulse width)	3.2000	3.5777	5.0596

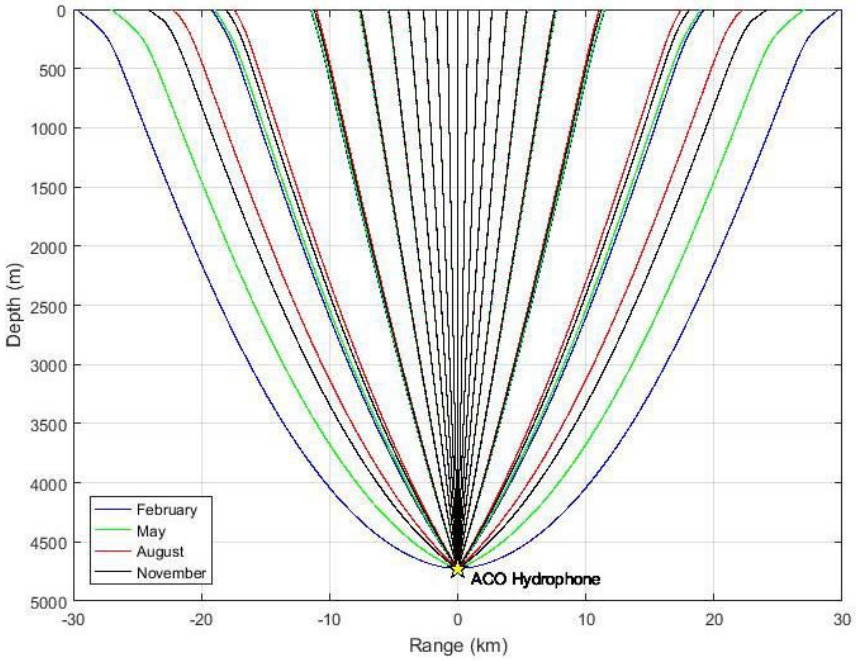

Figure 19. Surface ranges for the same launch angles for respective months. Sound speed field used for each month was derived from HOTS CTD casts taken in 2015.

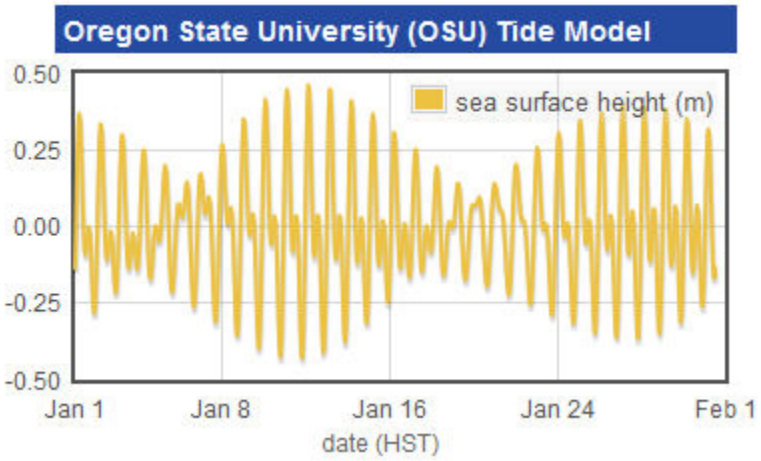

Figure 20. Tidal fluctuation at ACO for the month of January 2017. Data and graph is provided by Oregon State University's tide model. Largest difference between extreme high and low tides is approximately 0.89 m.

4. Preliminary Test Results - Second Experiment

On February 8, 2016, the R/V *Kilo Moana* embarked on a five day HOTS cruise. On the approach and departure from ACO the onboard echosounder and transducer array were used for the RAP Tomography project. The CW tone was transmitted every 15 s, with a transmission length of 16 ms, and a frequency of 3.5 kHz.

During the approach, the array was turned on as the R/V *Kilo Moana* passed Kaena Point. Clear receptions began to appear in the hydrophones data record when the R/V *Kilo Moana* was approximately 25 km away. The transmissions continued after reaching ACO for about five hours until they were subsequently turned off. **Figure 21** shows the vessels distance from ACO through time and the respective cross correlation amplitudes calculated using the hydrophone data.

The same analysis used earlier to determine the actual and estimated travel times were applied. Again, an error occurred due to the large pulse width of the Tekron (set to 100 ms). To correct for this, 100 ms was subtracted from the actual travel times and then compared with the estimates (**Figure 22**). There are a few irregularities/jumps that happen to occur when the vessel slows down/stops its current motion and when it begins to move after being stationary. This suggests some measurement errors are arising due to vessel acceleration, as the ship heading had no correlation with travel time differences (exact reasoning is still unknown). There is also substantial jitter in the data record, which is most likely the result of the varying trigger delay in the echosounder (**Table 1**).

Looking closer through the hydrophone data and the resulting cross correlation/complex demodulation values, smaller amplitude arrivals that do not correspond to the direct ray path occur. When the vessels range decreases the direct path amplitudes increase, as do these recurring smaller arrivals (**Figure 23**). These points correspond to the acoustic ray paths that have undergone bottom and surface bounces to ultimately reach the hydrophone. A good assumption to determine which peak corresponds to the ray path with one (BS), two (BSBS), etc. bottom/surface bounces is to look at its relative amplitude level. The arrival peak that has the largest amplitude (not counting the direct path) will correspond to the BS ray path, while the second largest corresponds to the BSBS ray path, and so forth.

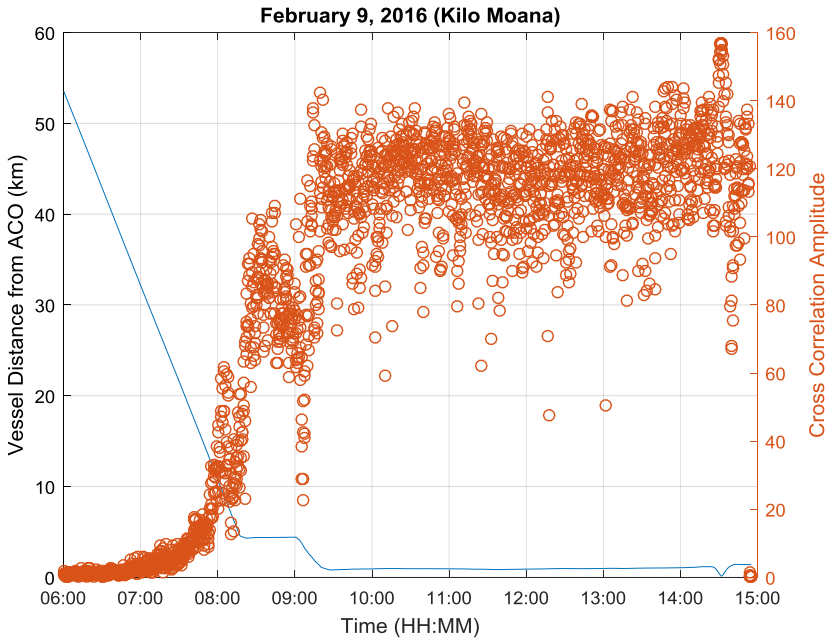

Figure 21. Plot of the R/V *Kilo Moana's* distance from ACO (blue) and the cross correlation amplitudes (red) for the hydrophone data on February 9, 2016.

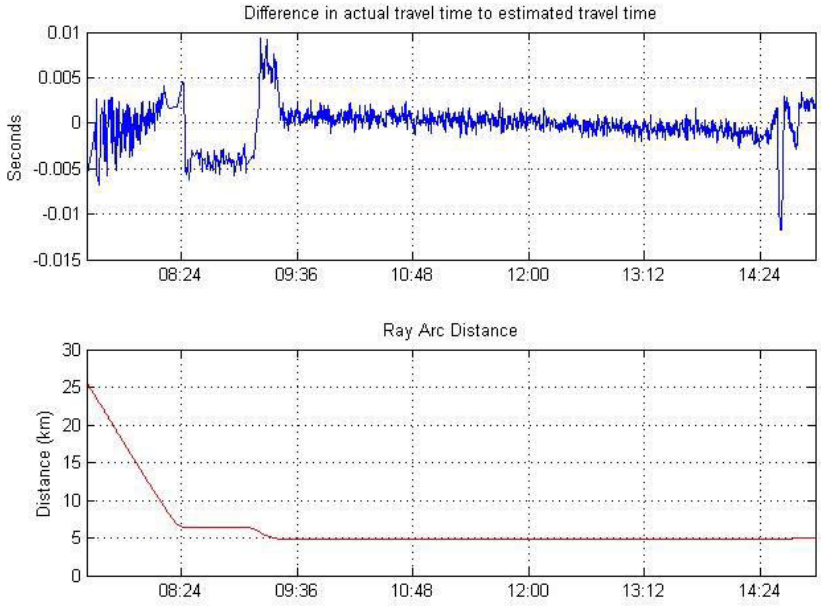

Figure 22. (Top) Plot of the difference in travel time between the actual (100 ms corrected) and estimated travel times. (Bottom) Plot of the corresponding distance for each ray path.

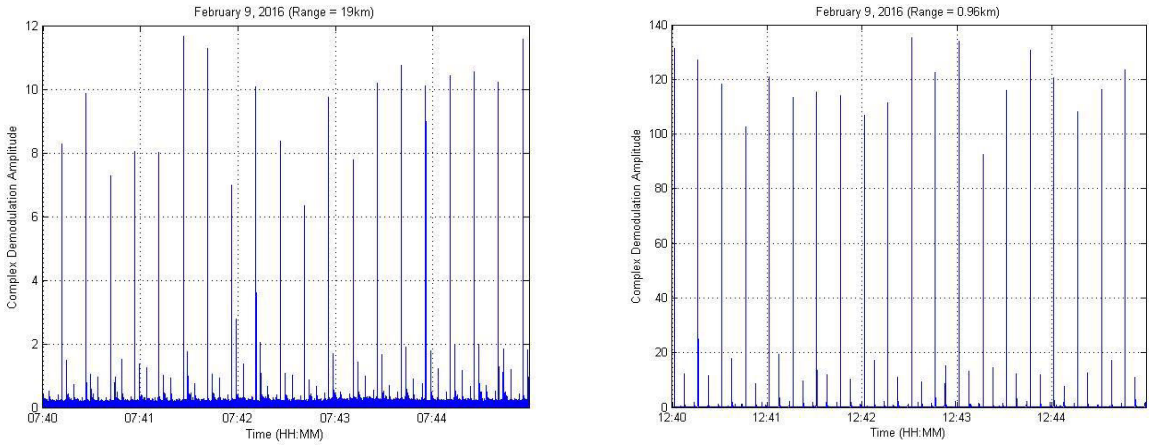

Figure 23. (Left) Complex demodulation values for hydrophone data when the R/V was about 19 km away. (Right) Values when the R/V was about 0.96 km from the hydrophone. Note: Bottom-surface arrivals are seen by the smaller amplitude peaks that occur one round trip travel time later then the RAP path.

A more sophisticated approach is taken in **Figure 24**. The complex demodulation values are converted into a signal to noise ratio (SNR). This is calculated by dividing the complex demodulation values by the median of itself. **Figure 24** expresses the SNR in decibel form plotted versus time and distance. Overlaid lines represent the estimated travel times for different ray paths. The estimated travel times were calculated using a similar approach described earlier (Snell's law), while assuming a reflection angle that matches the incident angle when the acoustic ray has a bottom or surface bounce and a constant seafloor depth that matches the hydrophone (4728 m). It is also important to note this figure is copy and pasted from 0 to 15 s to produce the 15 to 30 s portion. This was done to show the continuous trend for each arrival and also is used to justify changing the transmission interval to 30 s in later experiments (to prevent overlapping arrivals).

Another potential problem to consider is the effect an acoustic ray path with a single bottom bounce to the hydrophone has on the data collected. Since the hydrophone is mounted on the Junction Box (**Figure 4**) there is ~1.5 m between it and the seafloor. So if an acoustic transmission takes place directly overhead, the travel time difference between the RAP path and this single bottom bounce would be 2 ms (assuming a local sound speed of 1500 m/s). When the range increases this time difference will decrease (20 km surface range corresponds to a time

difference of 0.46 ms). When examining the hydrophone data this single bottom bounce does not appear to be influencing the RAP reception, even when at/near directly overhead. The RAP reception is most likely too strong and the bottom bounce reception cannot be seen.

On February 12, 2016, the crew finished up with their primary objectives at Station ALOHA and began its return voyage. The array was turned on when the R/V *Kilo Moana* was about 11 km from ACO and remained on until they reached Kaena Point. The setup was identical to the approach and no new insight was gained due to the similarities between the two.

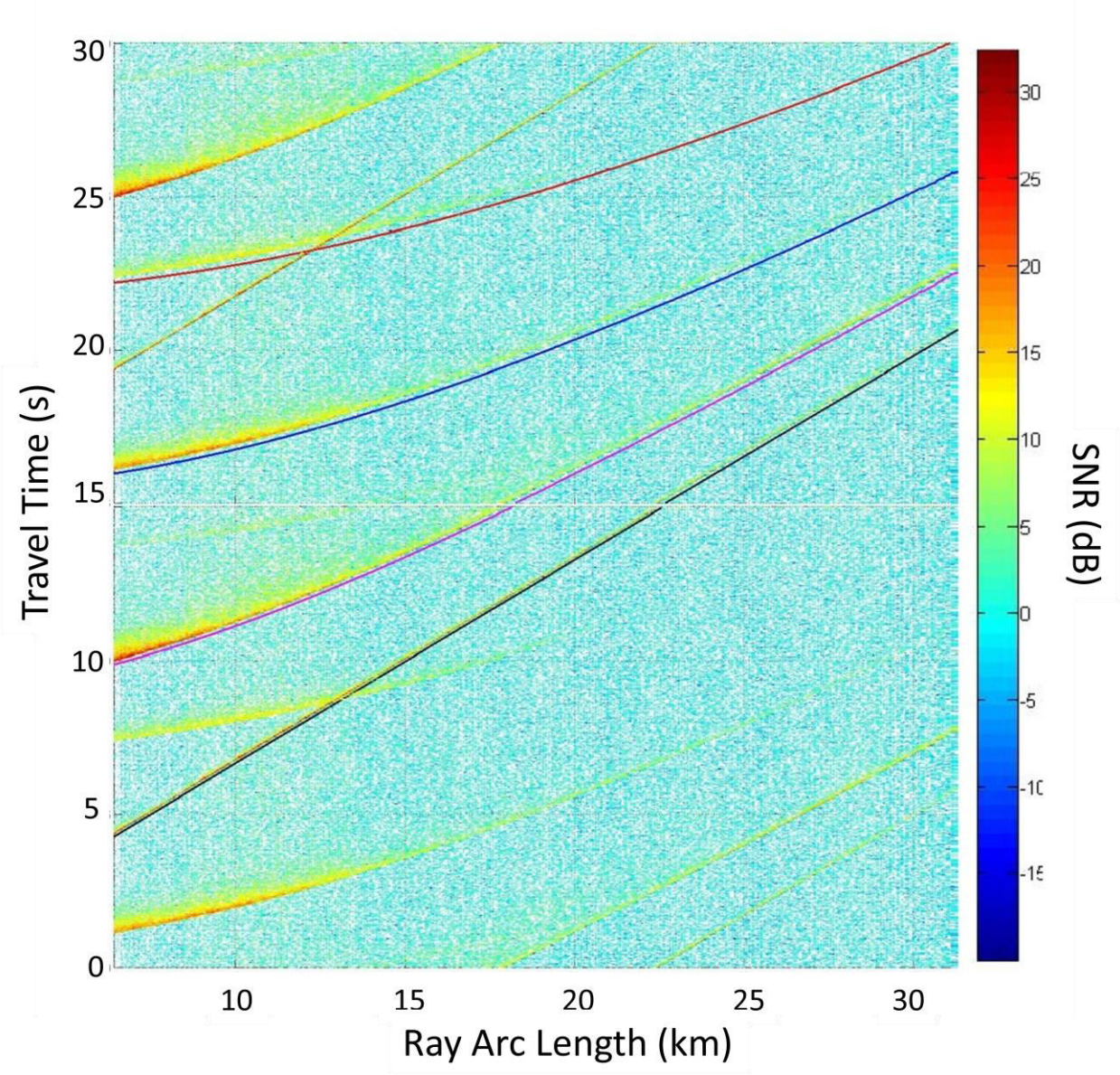

Figure 24. SNR (dB) versus time and distance. The zero time on the y-axis corresponds to the time of acoustic transmission. The x-axis corresponds to the ray arc length of the direct ray path (the minimum value is the hydrophone water depth). The direct (black), BS (pink), BSBS (blue), and BSBSBS (red) curves are their respective estimated travel times. Note: The portion from 0-15 s is copy and pasted above to produce the 15-30 s portion, since the transmission interval was every 15 s.

5. Second Experiment Setup

After analyzing the data from these previous experiments it was apparent the experiment setup needed some improvement. The most significant upgrade that needed to be made was the measurement for the time of acoustic transmission. Between the ambiguity on when the Knudsen echosounder was triggered from the Tekron to the varying jitter as it relays power to the transducers, made for difficult and imprecise time measurements.

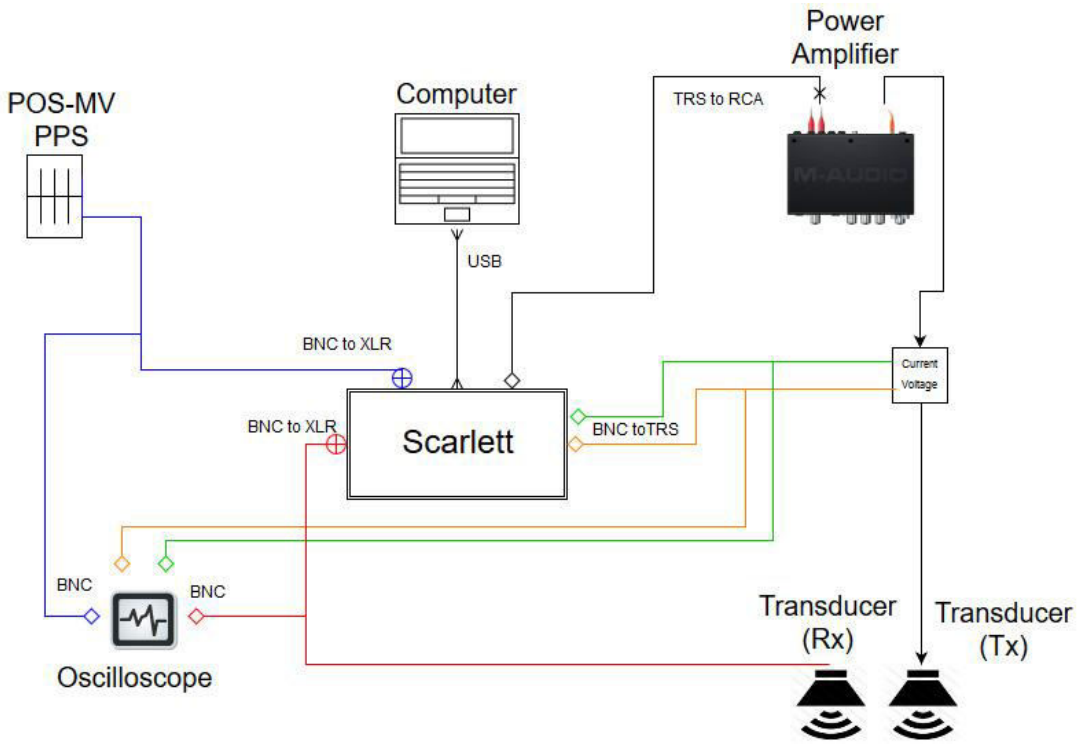

Figure 25. Diagram of the new experimental setup. Connector types are shown.

In the new configuration, measurements will be recorded through an audio interface (Focusrite Scarlett 6i6, **Appendix E**) connected to an onboard laptop computer via USB. The Scarlett will also be relaying the computer generated acoustic transmission to the power amplifier (Proel HPX2800, **Appendix F**). The output of the power amplifier goes first through a circuit to measure the voltage and current (**Figure 26**; recorded by the Scarlett) then goes directly to transducer #9

in **Figure 5**. Once the signal is sent, a reference transducer (transducer #10, located outboard of the transmitting transducer) receives the transmission. This signal is then input to the Scarlett to ensure the waveform matches the one produced by the laptop and to increase accuracy for time of transmission. The Scarlett also has an input designated for the PPS that is generated by the POS-MV onboard, directly linked to the primary GPS receiver (**Figure 25).** All of the Scarlett inputs and outputs are available for real-time viewing with an oscilloscope.

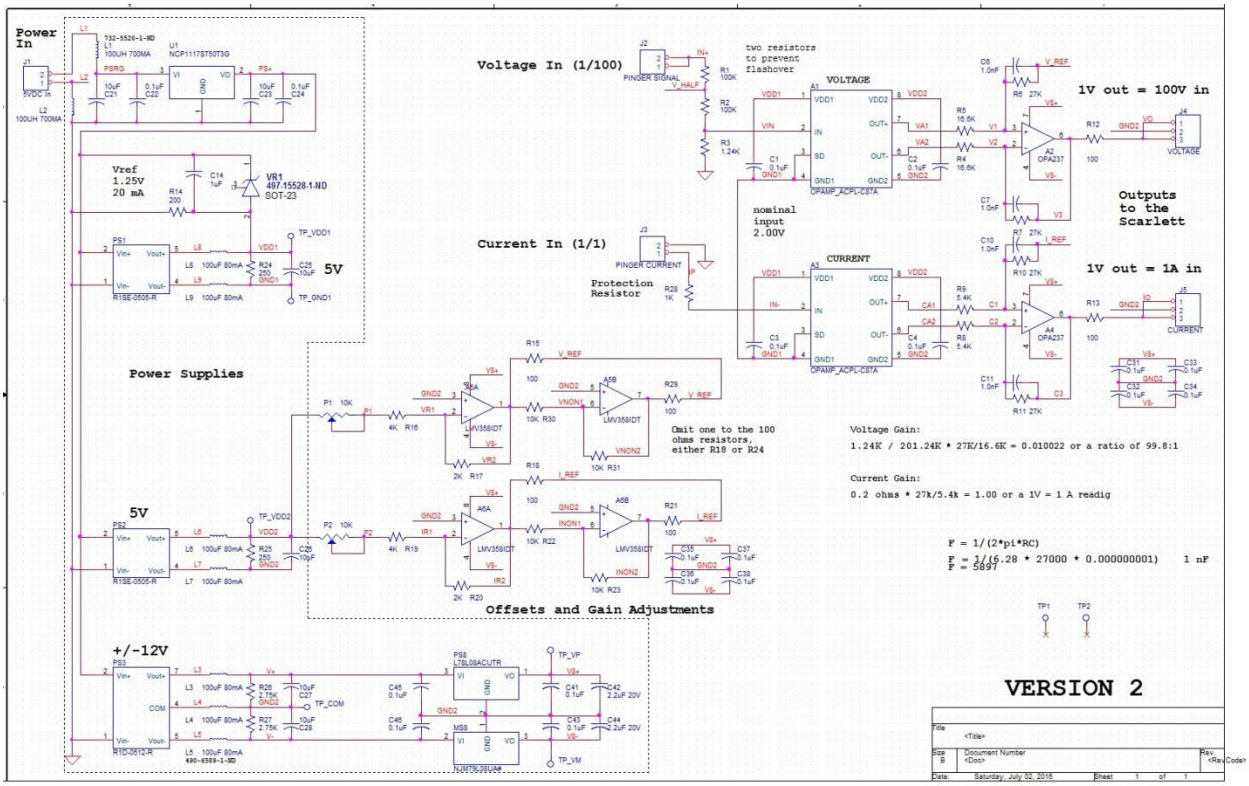

Figure 26. Schematic for the interface module that allows for voltage and current measurements along the cable in **Figure 25**. The interface module outputs the voltage at a 1:100 ratio (100 V in - 1 V out) and the current is output at a 1:1 ratio (1 A in - 1 V out).

The laptop communicates with the Scarlett through Matlab and C code and receives all the data that is input into it (reference hydrophone, PPS, voltage, and current). The laptop will be set and synchronized with a NTP server to get relatively accurate timing information (within +/- 100ms). We will obtain the exact time for all Scarlett recorded data using the offset between the

computer's integer second with the PPS. **Figure 27** illustrates the time correction made for a sample transmission using a PPS.

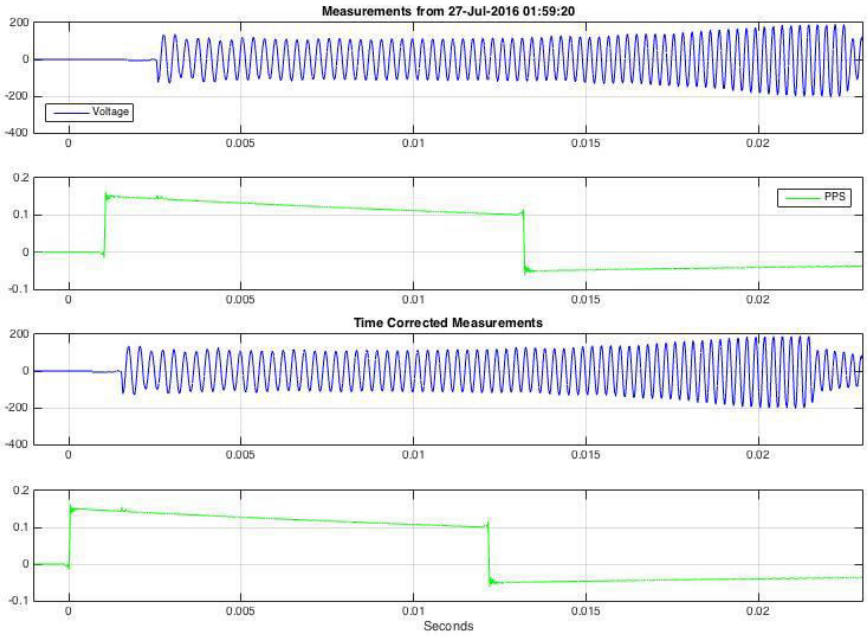

Figure 27. (Top two plots) Measurements of the voltage (blue) and the PPS (green) during a sample transmission. The x-axis in seconds is relative to 27-Jul-2016 1:59:20 UTC according to computer time. (Bottom two plots) Time corrected measurements for voltage and PPS during a sample transmission. The x-axis in seconds is relative to 27-Jul-2016 1:59:20 UTC according to GPS time.

The sample rate for the Scarlett is 44.1 kHz, quickly leading to large data files. To prevent the laptop's memory from being overloaded and to keep the file sizes manageable, the sampling/transmitting will be separated into 15 minute intervals. In between these intervals the laptop takes about 2-3 minutes to transfer the data in computer memory from the past 15 minutes to an external hard drive. During this period, there will be no sampling or acoustic transmissions, leaving this 2-3 minute gap every 15 minutes (**Figure 29**).

The delay between when the start of the voltage transmit signal is measured and when the transducer actually transmits the acoustic signal is inferred from comparing the transmit voltage

waveform and the reference hydrophone waveform. **Figure 28** shows a sample record of the timing between the transmitting and reference transducers. The mean delay between them over a course of transmissions is 0.73 ms (little variation). The centers of the two transducers are separated by 0.184 m, corresponding to ~0.123 ms travel time (assuming transmission through water), leaving us with a system delay of 0.607 ms. Since the transducers are the exact same model and run through the same length of cable, it is safe to assume the delay on the transmitting and receiving side are equal. Dividing the entire system delay in half, the transmission delay is 0.304 ms. This constant 0.304 ms will be added to each acoustic transmission time.

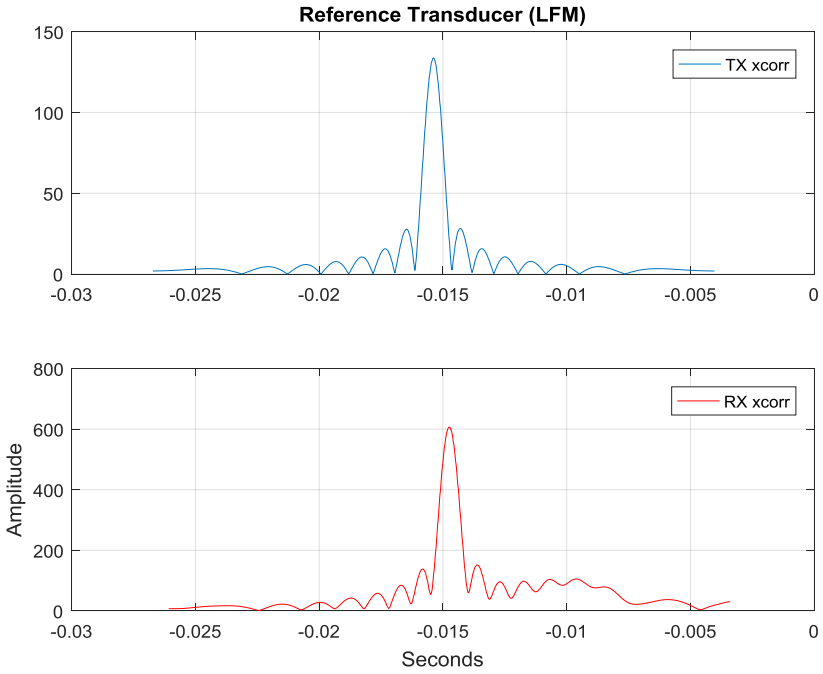

Figure 28. Sample plot between the main transducers time of LFM transmission (top) and the reference transducers time of reception (bottom). The mean delay between the two is 0.73 ms. Time axis is relative to computer time during a series of transmissions.

Bypassing the pre-existing onboard echosounder electronics allows for this improvement in accurate/precise time measurements, but also provides more flexibility with what signals can be sent. With the acquisition of the Scarlett and power amplifier any desired waveform can be generated with the onboard laptop and transmitted. Then when it comes to the signal analysis a

replica pulse will no longer needed to be empirically estimated, because the exact signal will be known and confirmed using the data provided by the reference transducer. This provides a large advantage over the old setup, as it was difficult to get a replica pulse that provided a large processing gain and to correctly pick the beginning of the reception when using Knudsen's Chirp signal during the first experiment.

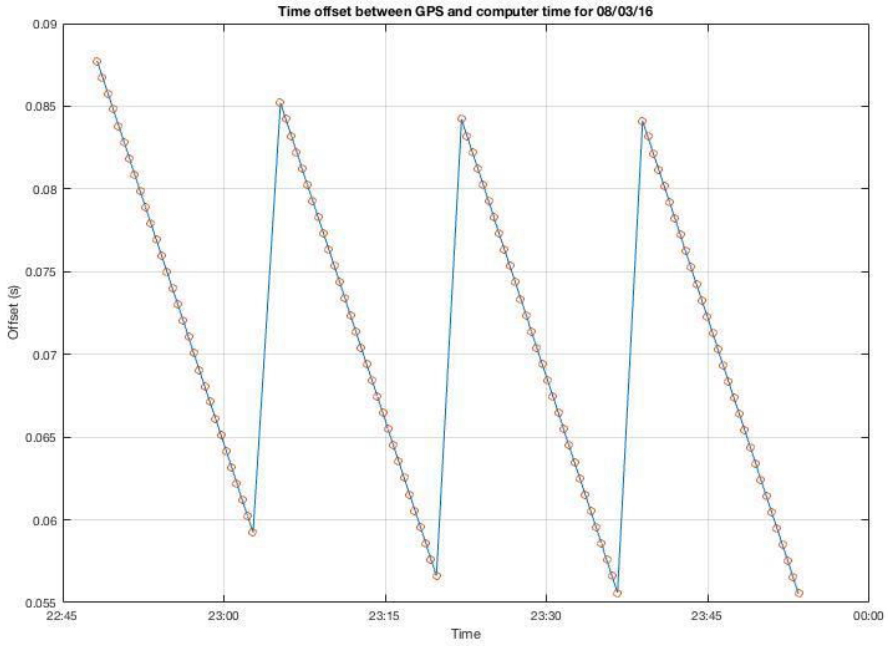

Figure 29. Time offset between GPS and computer time for a laboratory test occurring over approximately an hour (red circles represent the offset during a transmission). Acoustic transmissions were sent every 30 seconds over a 15 minute interval. The Scarlett time drifts about 30 ms every 15 minutes, after which the laptop collects the data for about 2-3 minutes and then continues sampling/transmitting. The computer time drifts about 4 ms over a 45 minute period when looking at the time offset between samples collected during the first and last 15 minute interval.

For the next cruises, the primary signals to be tested are a LFM sweep and M-sequence both with a center frequency of 4134.375 Hz, 1378.125 Hz bandwidth, and ~22.5 ms duration (**Appendix A**). This cycle will be repeated every 30 s to allow enough time between each transmission for no overlapping of the direct, BS, BSBS, or BSBSBS ray path arrivals (similar to **Figure 24**). The

signal duration was selected in order to have the waveform remain insensitive to Doppler shift from vessel movement (maximum velocity of 12 knots), but also provide a long enough pulse to provide sufficient processing gain (PG).

$$PG = 10\log(BW * t) \quad (7)$$

where BW is bandwidth and t is signal duration and describes the ratio of the spread bandwidth to the baseband bandwidth (Munk, Worcester and Wunsch 1995).

To find the SNR at various ranges the sound pressure level (SPL) must be calculated

$$SPL = 170.8 + 10logP + DI \quad (8)$$

where P is the acoustic power (W) and the directivity index (DI) is given as 2.65 dB vertically below and the beam pattern is nearly constant (due to single transducer) from Massa (2016). The transducer (Massa TR-1075A) is rated for 600 W at 2% duty cycle and the DI depends on the wavelength transmitted and radius of transducer head. Taking into account cable loss, impedance mismatch, and transducer efficiency the actual power output is approximately 30% of the input (Massa Sonic 2016), resulting in a 180 W acoustic output. The SPL comes out to be 196.0 dB re 1 μPa at 1 m and we can find the received level (RL) at any range

$$RL = SPL - (NL + 10\log(BW)) - VL - TL \quad (9)$$

where NL is the noise level, 10 log(BW) is the width of the noise band, VL is the volume loss (attenuation), and TL is transmission loss (here spherical spreading) (Medwin 2005). For a ray arc length of 30 km the RL is 10.6 dB.

The SNR is the sum of the RL and PG. At 30 km ray arc length this comes out to 25.5 dB, which should be a sufficient amount of SNR for a reception at the hydrophone. See **Table 2**. The RMS travel time error (σ_t) depends on this SNR and the signals complex demodulation pulse width (**Equation (10)**).

$$\sigma_t = \left[(\Delta\omega_{rms})\sqrt{SNR}\right]^{-1} \quad (10)$$

Table 2. Expected SNR for the LFM and M-sequence transmissions at a range of 30 km.

Source Level (SPL)	196.0 dB re 1 μPa at 1 m
Spreading loss (TL)	-89.5 dB
Attenuation (VL)	-4.5 dB
Received signal intensity	102.0 dB re 1 μPa
Noise (NL)	60.0 dB re 1 μPa/(Hz)$^{1/2}$
Bandwidth (1378.125 Hz)	31.4 dB
Receiver noise level	91.4 dB
Processing gain (PG)	14.9 dB
SNR	25.5 dB

Here $\Delta\omega_{rms}$ is the RMS bandwidth of the generated pulse and is given by

$$(\Delta\omega_{rms})^2 = \frac{\int_{-\infty}^{\infty} f^2 |P_z(f)|^2 df}{\int_{-\infty}^{\infty} |P_z(f)|^2 df} - \left[\frac{\int_{-\infty}^{\infty} f |P_z(f)|^2 df}{\int_{-\infty}^{\infty} |P_z(f)|^2 df}\right]^2 \quad \textbf{(11)}$$

where $P_z(f)$ is the frequency spectrum for the signal (Rihaczek 1985). Over the frequency spectrum for these two signals (LFM and M-sequence) $P_z(f)$ can be considered to be a constant (see TVR response, **Appendix B**). Also, the limits from **Equation (11)** can be reduced to the frequency over which the signal is being sent. In doing so the second term simplifies to zero and we are left with

$$(\Delta\omega_{rms})^2 = \frac{4\int_{f_o-B/2}^{f_o+B/2} (f-f_o)^2 df}{\int_{f_o-B/2}^{f_o+B/2} df} = \frac{B^2}{3} \quad \textbf{(12)}$$

where the center frequency f_o is included and a factor of 4 is derived from the variance of the frequency spectrum function (Rihaczek 1985)(Munk, Worcester and Wunsch 1995). Since the signals have a bandwidth of 1378.125 Hz, the RMS bandwidth is calculated to be 795.661 Hz (**Appendix A**). Assuming a particular reception provides a SNR of 10 dB then we can expect a rms travel time precision of 0.4 ms. If SNR is 20 dB, the precision is 0.13 ms.

6. HOTS Cruise Experiment

On January 22, 2017 the R/V *Kilo Moana* embarked on a four day HOTS cruise to Station ALOHA. This was used as yet another cruise of opportunity and allowed for the first at sea test of the new (second) experimental setup described in **Section 5**. Acoustic transmissions began as the vessel approached ACO and remained running for the next 40 hours. During this period, the LFM and M-sequence waveforms (**Appendix A**) were sent using a 30 s interval between each transmission. At this point transmissions were ordered to cease operation until further notice.

Upon termination, we learned that the use of the onboard Knudsen echosounder would still be permitted, but we could no longer use the LFM or M-sequence signals. So we modified the current setup (**Figure 25**) and replaced the power amplifier with the Knudsen echosounder (**Figure 30**). While this was somewhat similar to the preliminary experiments performed in **Sections 3 and 4**, it remedied the transmission timing issues that were occurring due to jitter in the echosounder.

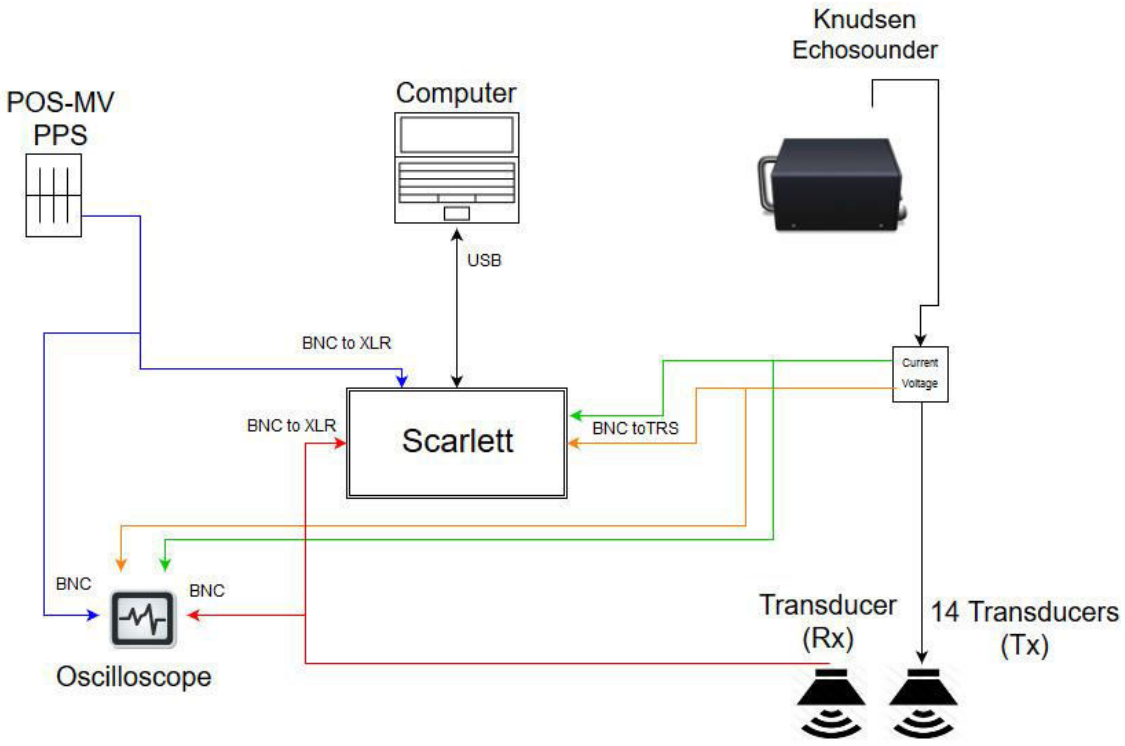

Figure 30. Experimental setup for the last portion of the January 2017 HOTS cruise.

Acoustic transmissions resumed approximately 19 hours after they were initially halted, and continued to run for the next 10 hours until the R/V *Kilo Moana* was outside of the ACO's hydrophone 30 km RAP radius. During this time, the Knudsen CW and Chirp signals were sent with a duration of 16 ms and a 20 s interval between each transmission (longest allowable interval). The CW was a simple 3.5 kHz sine wave and the Chirp had a center frequency of 3.5 kHz with a bandwidth of 3 kHz.

In total, acoustic transmissions were sent for approximately 50 hours during the entirety of the cruise. See **Appendix C** for the time log of acoustic transmissions. Although the preliminary experiments used the CW as the main transmitting signal, it was determined to no longer include them for the purposes of our project, the main reason being the poor travel time resolution compared to the other three signals. The RMS bandwidth for a CW is the inverse of the signal duration, which is 62.5 Hz for this case. Using **Equation (10)**, the travel time precision for a CW signal with a SNR of 10 dB is only 5.1 ms. Compared to the LFM, M-sequence, and Chirp travel time precision of 0.4 ms, 0.4 ms, 0.2 ms (larger bandwidth), respectively for the same SNR. For these reasons the CW transmissions sent during this experiment will not be used. Also, all receptions with less than a SNR of 7 dB were deemed unusable and too weak to include.

Upon first inspection of the POS-MV (GPS) data, there is a clear segment of time where the GPS coordinates for the R/V *Kilo Moana* were invalid. **Figure 31** shows the vessels altitude and altitude errors for the duration of the cruise. There is a clear portion where the altitude values seem to jump and oscillate irregularly and the altitude errors confirm that the data collected at these points are unusable. **Figure 32** follows the same format except showing the vessels latitude and longitude values along with their errors. The time interval above with large errors in altitude correspond to the same time of large errors for latitude and longitude. It is unknown what exactly caused the higher levels of errors, but it occurred after the ship was stationary for a long duration and the errors begin to return to their baseline values once the ship moved to the SE. For the rest of the data analysis, transmissions that took place during this six hour segment will be ignored. **Table 3** summarizes the transmissions received at the hydrophone for each signal.

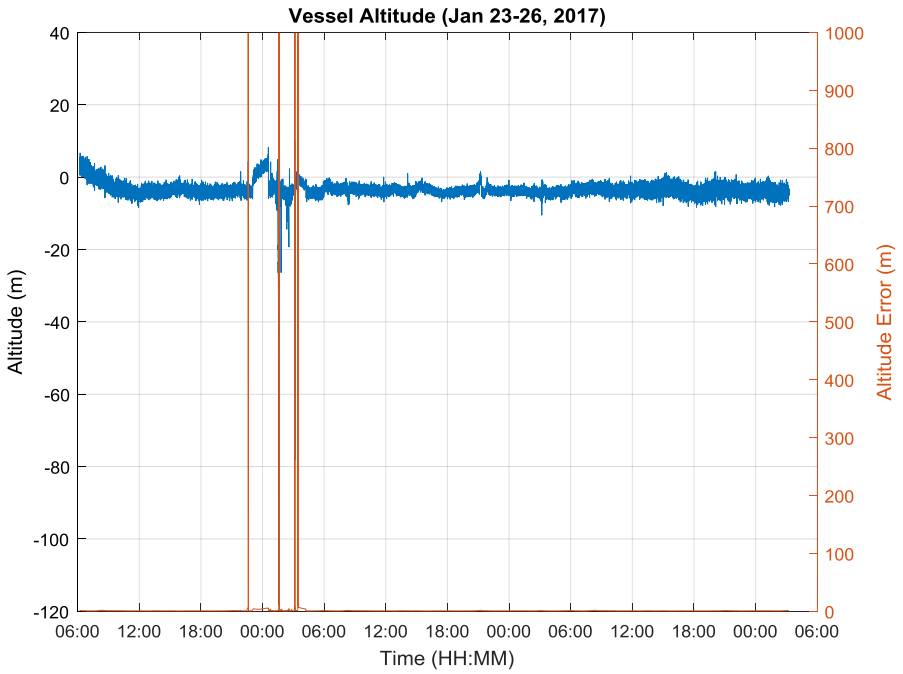

Figure 31. Vessel altitude (blue) and the associated errors for each point (red) during the January 2017 HOTS cruise.

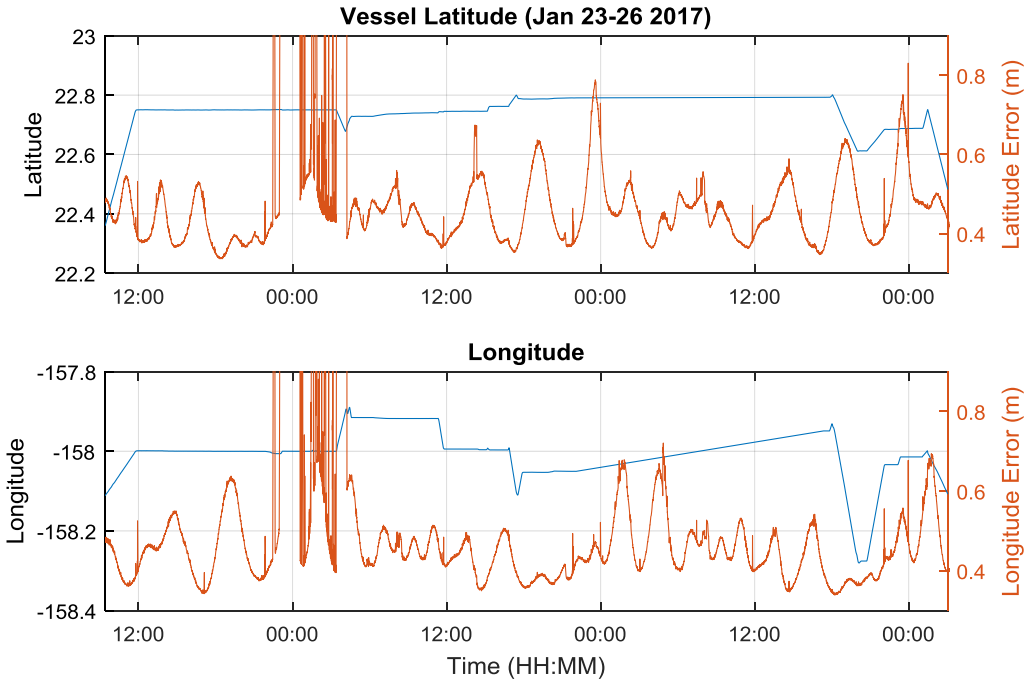

Figure 32. Vessel latitude/longitude (blue) and the associated errors for each point (red) during the January 2017 HOTS cruise.

Table 3. Number of transmissions received for each signal and their associated duty cycle.

	LFM	M-sequence	Chirp
Number of Transmissions	1864	924	592
Duty Cycle	0.075%	0.075%	0.080%

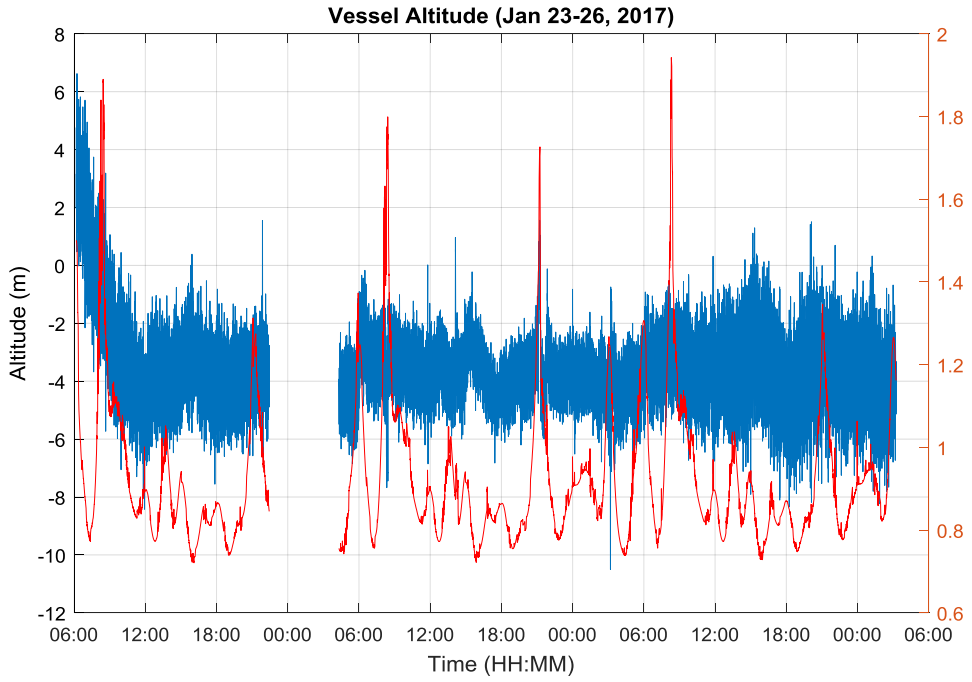

Figure 33. Vessel altitude (blue) and the associated errors for each point (red) with the large errors from **Figure 31** removed (~6 hours of data).

Figure 33 shows the corrected version and plot for the vessel's altitude and errors while at ACO. The altitude errors hovered around 0.9 m and were too large to be able to successfully resolve a tidal cycle(s) during the cruise. For future cruises the altitude (and latitude/longitude) errors will be significantly less (see **Appendix D**). With this segment of data removed, the remaining hydrophone receptions can begin to be examined. The exact time of acoustic transmissions are determined using the voltage measurements between the power amplifier/echosounder and the transducer(s) (see **Section 5**). The time of arrival is determined by cross correlating the hydrophone data (collected on shore) with a replica pulse; the time associated with the demodulated correlation peak maximum is the measured arrival time (see **Section 3**). **Figure 34** shows the measured acoustic travel times for each transmission and provides a good first check

to ensure each record is consistent with others that are at or near the same distance for the duration of the experiment. The travel times extend out in a parabola-like fashion since they are plotted with respect to surface distance. They would become a straight line if plotted with respect to their ray arc length instead.

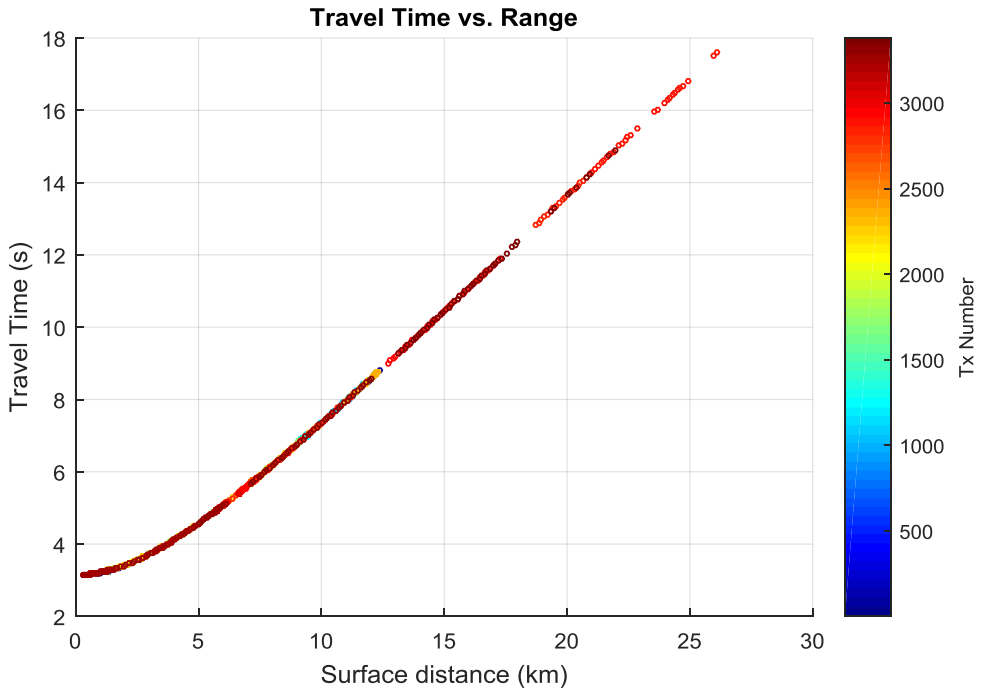

Figure 34. Plot of the measured travel time with respect to the vessels surface distance for each acoustic transmission during the January 2017 HOTS Cruise. The color represents the transmission number, with the dark blue being the first one sent and the dark red being the last (early ones are hidden).

With the acoustic travel times determined, comparisons can be made between them and estimated travel times. Estimated times are calculated using a sound speed profile (**Figure 35**) derived from a CTD cast that was conducted near ACO (similar to **Sections 3** and **4**). The plot for **Figure 36** shows the difference between the actual and estimated travel times through the course of the cruise. The first gap in the data corresponds to the time when the POS-MV was producing bad GPS data. The second gap corresponding to the downtime when switching transmissions over from the setup in **Figure 25** (LFM and M-sequence) to the setup in **Figure 30**

(CW and Chirp). At first glance there is a clear pattern that occurs from when the vessel is stationary compared to when it is traversing around ACO. When the R/V *Kilo Moana* is stationary the travel time differences more or less remain constant at a particular value, as expected. As soon as the ship begins to move again there is a linear change in the travel time differences until the vessel comes to another standstill. While this holds true for most of the data there is one particular section that seems to deviate more than the others.

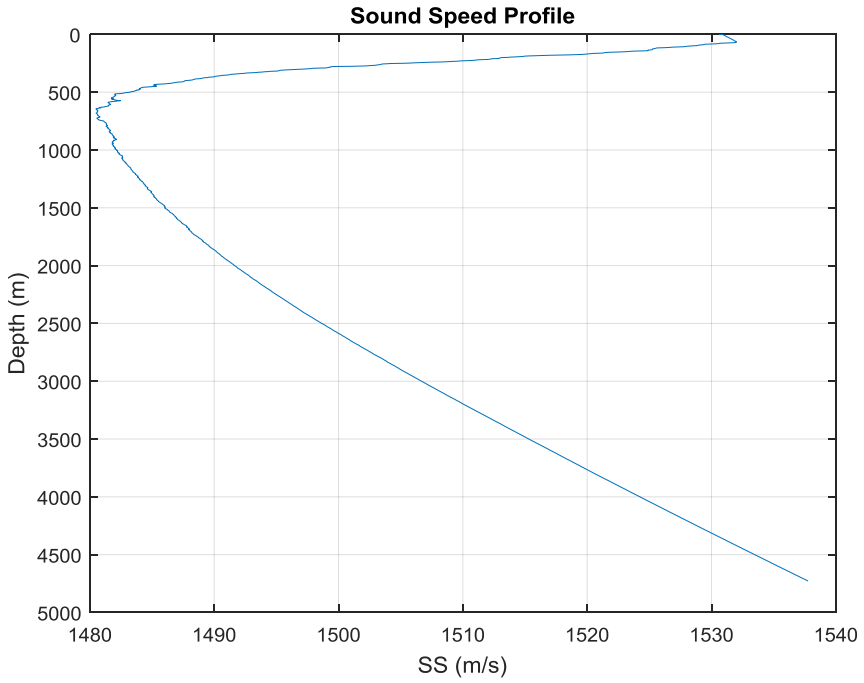

Figure 35. Sound speed profile at Station ALOHA derived from a CTD cast during the January 2017 HOTS cruise.

Figure 37 takes a closer look at the section just after the first gap in **Figure 36**. During this time the ship was stationary and was approximately 9 km from the ACO hydrophone. It is apparent that the travel time difference is fluctuating between two different values and they are separated by about 4 ms. To get a better idea of what is causing this discrepancy **Figure 38 A** and **B** each look at an acoustic reception (top plot) and their corresponding cross correlation (bottom plot) during this period. The receptions are labeled with the time of arrival (red circle), surface distance from the hydrophone, and the type of signal received. The cross correlations maximum values are labeled by the red circle as well and the amplitude is given in SNR (dB). In both **A** and **B** there are two major peaks for the cross correlation and are separated by approximately 4 ms. We see in **Figure 38 A** the first peak is slightly larger than the second, while in **B** it is the opposite. Using this it becomes clear why the travel time differences were alternating between two values during this time and the first peak will be selected as the true arrival time for all receptions here. It is still unknown what caused this (the second peak) and why this occurred only during this segment of the cruise, as there were other data points from this same range that did not have these dual cross correlation peaks.

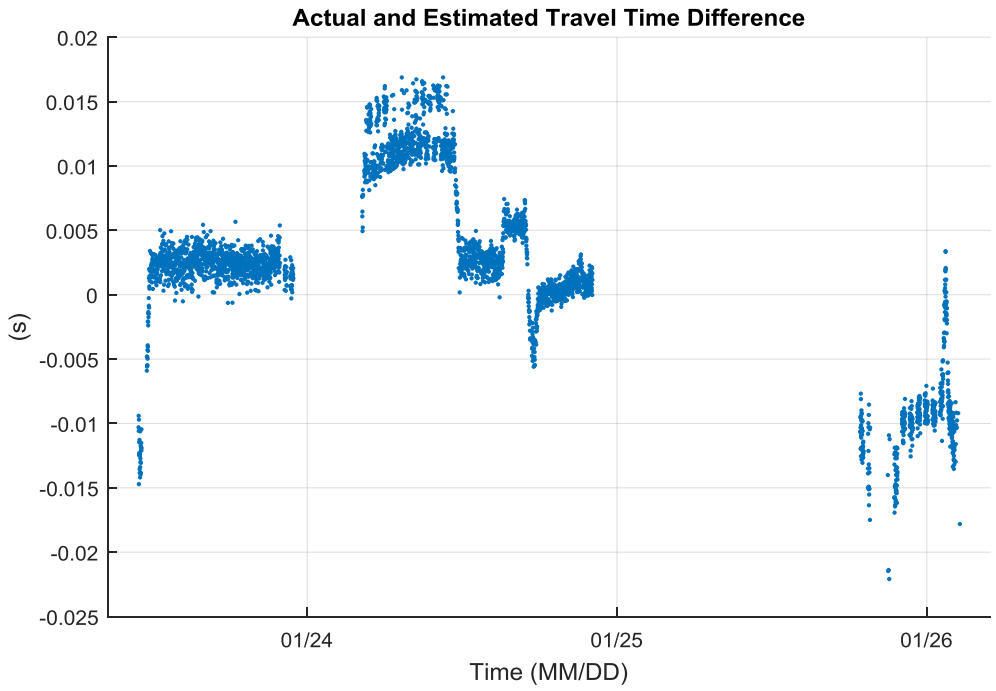

Figure 36. Actual vs. estimated travel times for all acoustic transmissions on the January 2017 HOTS cruise.

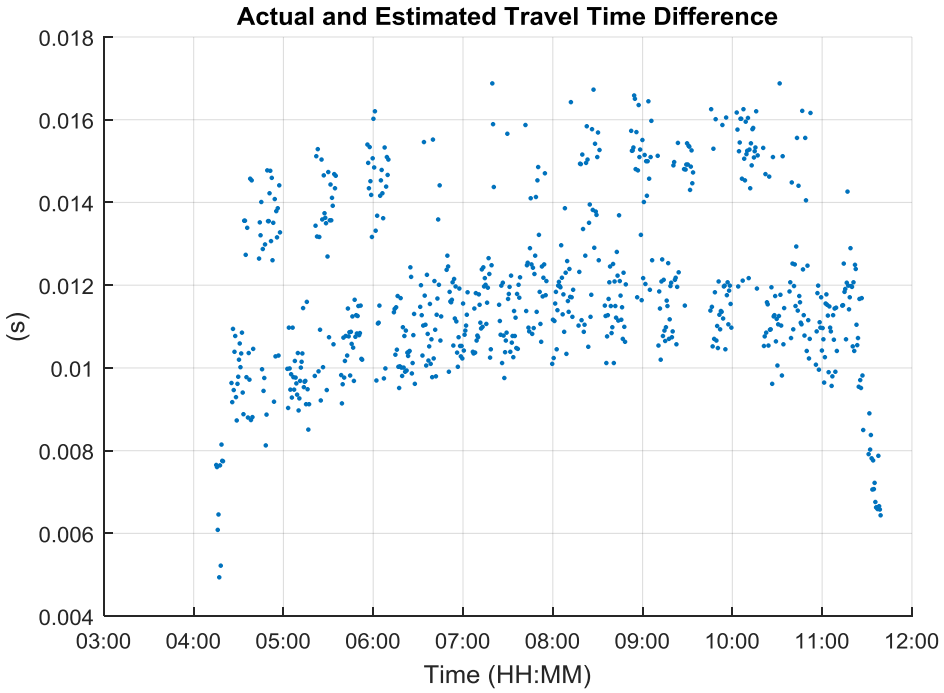

Figure 37. Zoomed in view of the section from **Figure 36** on January 24, 2017.

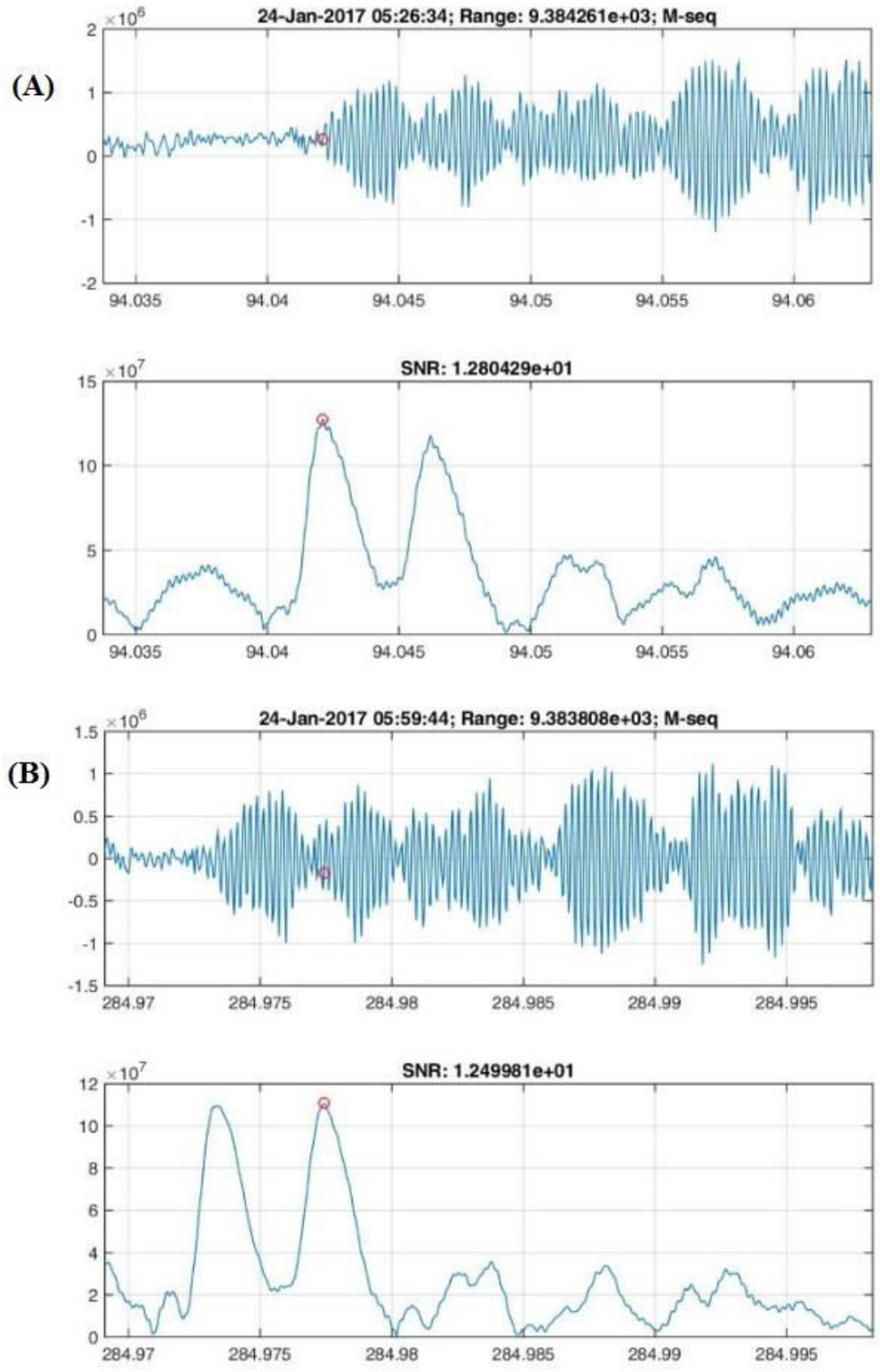

Figure 38. Sample plots of M-sequence arrivals (top) and their cross correlation amplitudes (bottom) used to compute the travel time differences in **Figure 37**. The x-axis represents the number of seconds into a 5-minute audio file and the y-axis represents amplitude (arbitrary).

The top plot in **Figure 39** shows the corrected version for the difference between actual and estimated travel times. The lower plot shows the R/V *Kilo Moana's* position during the course of the experiment. For both plots the color represents the transmission number and can be used to match a travel time difference with a vessel location. The travel time perturbations were largely positive when the vessel was located to the East of the hydrophone. While the travel time perturbations were predominately negative when the vessel was to the South and Southwest of the hydrophone. These results suggest that the true sound speed field is slower to the East and faster to the South and Southwest of the hydrophone, when compared to the estimated sound speed field in **Figure 35**.

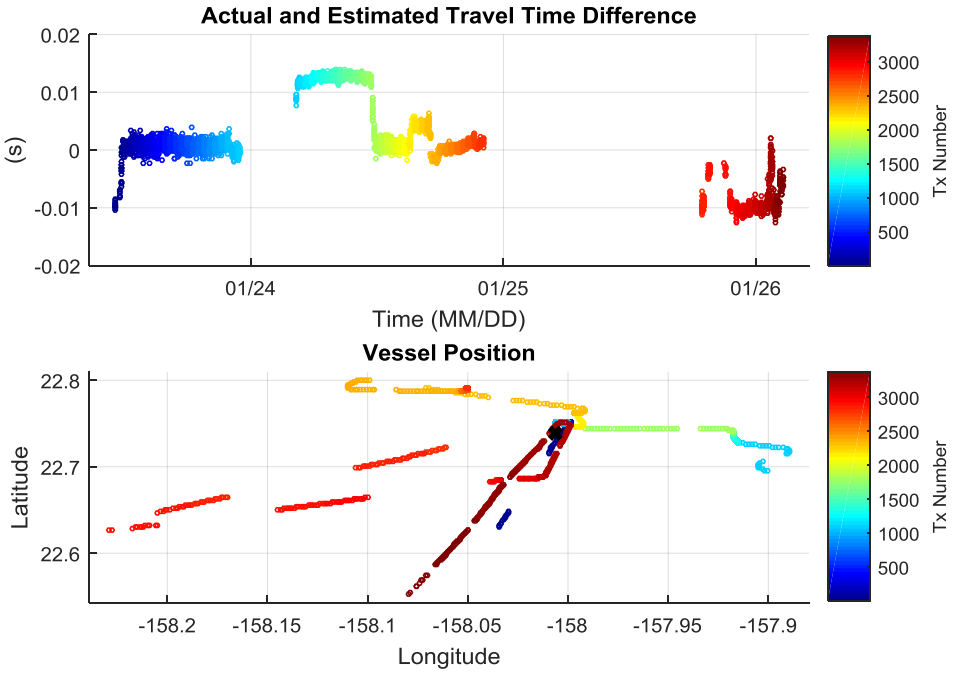

Figure 39. (Top) Plot of corrected actual vs. estimated travel times. (Bottom) Plot of the vessel's position during the cruise. The color scale represents the transmission number for both plots.

Figure 40 shows the travel time difference with respect to surface distance. Again, the color represents the transmission number and can be paired with the vessel's latitude and longitude from **Figure 39**. The actual and estimated travel times are very similar when the ship is

above/near the hydrophone. As the distance increases between the two, the time differences increase as well. This would be expected for a simple. range independent sound speed perturbation because any difference in the estimated sound speed field with the true field will increase the travel time difference the further the acoustic ray must travel, just due to simple geometrical considerations. The maximum time differences, coincidentally, follow a somewhat parabolic pattern out to 10 km, implying these acoustic paths have the same magnitude of sound speed difference between the estimated sound speed field, but with opposite sign. The line of points scattered around zero travel time difference out to this range correspond to when the vessel was West-Northwest of the hydrophone. Also, when the vessel was greater than 15 km from the hydrophone during its departure from Station ALOHA (moving SSW) the travel time differences begin to converge back to 0. These areas of the ocean seem to be well represented by the estimated sound speed field. **Figure 41** uses the travel time differences to compute a corresponding sound speed difference (δc) for each transmission. For this initial, simple interpretation, the true sound speed is averaged along the ray path and the estimated is the depth averaged sound speed for the a priori field (c_o = 1512 m/s). The calculation is given by

$$\delta c = -\frac{{c_o}^2}{s}\delta t \tag{13}$$

where s is the total ray arc length and δt is the travel time difference. We see the sound speed difference has the opposite sign of the travel time difference, as the points are reflected across the x-axis between the two figures. Also, using the sound speed difference turns the parabolic shape of **Figure 40** (out to ~10 km) into straight lines, because this sound speed difference has a cumulative effect on the travel time as the range increases. Transmissions made past 5 km range during the end of the cruise (red dots), begin to approach zero difference between the estimated and measured sound speeds along the ray path. This is expected, because in **Figure 40** the time difference past 5 km remains constant and even begins to decrease as the distance increases (>10 km). Therefore the sound speed difference averaged over the ray path will decrease.

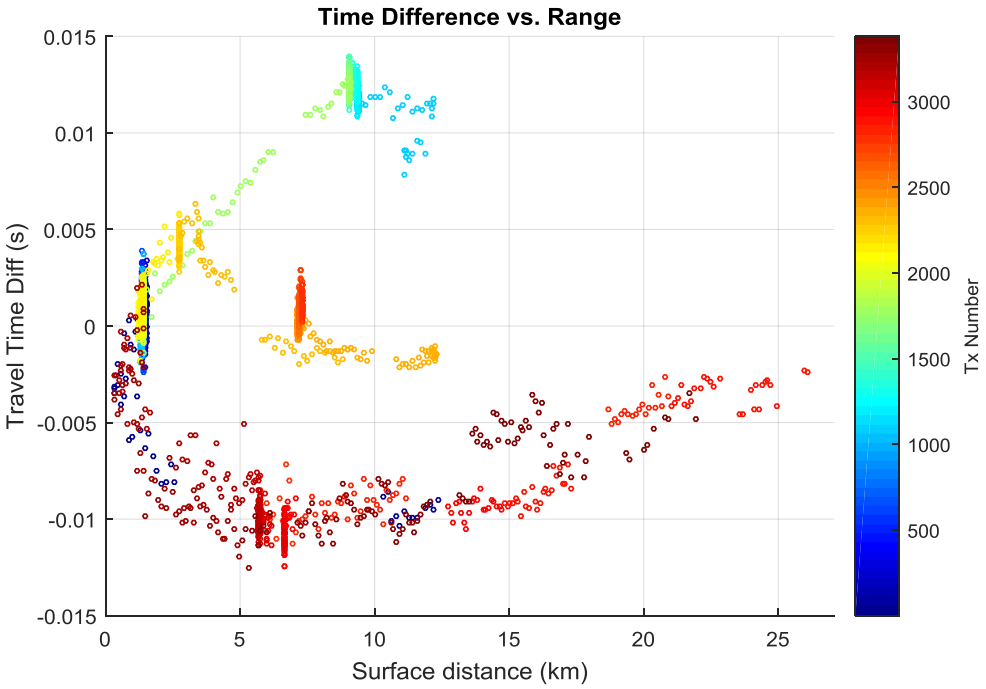

Figure 40. Difference between actual and estimated travel times with respect to range. The color represents the number of transmission.

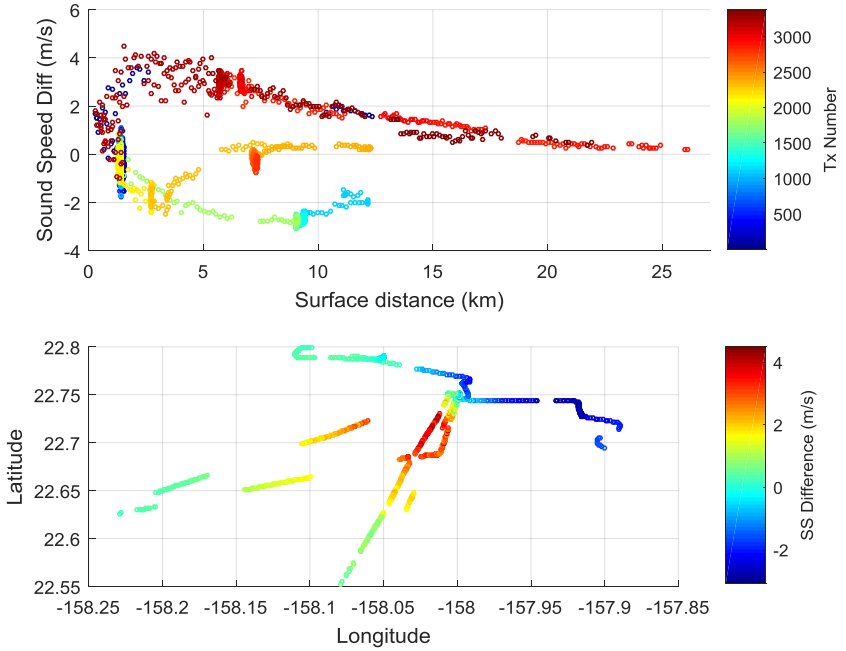

Figure 41. Difference between the true and estimated sound speeds with respect to range (top) and latitude/longitude (bottom), derived from **Figure 40**.

Figure 42 compares the SNR for each transmission and shows the corresponding signal that was used. The Chirp has a much larger SNR at short ranges (<2 km). This should be expected, since fourteen transducers were driven to send this narrow beam signal compared to just the one transducer for the LFM and M-sequence. From about 3 km to 12 km all three signals follow the same linear decrease in SNR and provide similar results at each range. Around 12 km there are no more LFM and M-sequence receptions that produce a SNR over the 7 dB threshold. Only during the initial approach was the R/V *Kilo Moana* outside of this range when transmitting these two signals. It will be interesting to see with the next test whether this was a onetime occurrence or 12 km is in fact the limiting range when using one transducer with these signals. **Figure 42** seems to suggest we could possibly get receptions beyond this range, since the Chirp follows the same SNR pattern and hovers around 10 dB from about 12 km to 25 km; the main difference being the Chirp had over triple the amount of transmissions at these long ranges when compared to the LFM and M-sequence combined.

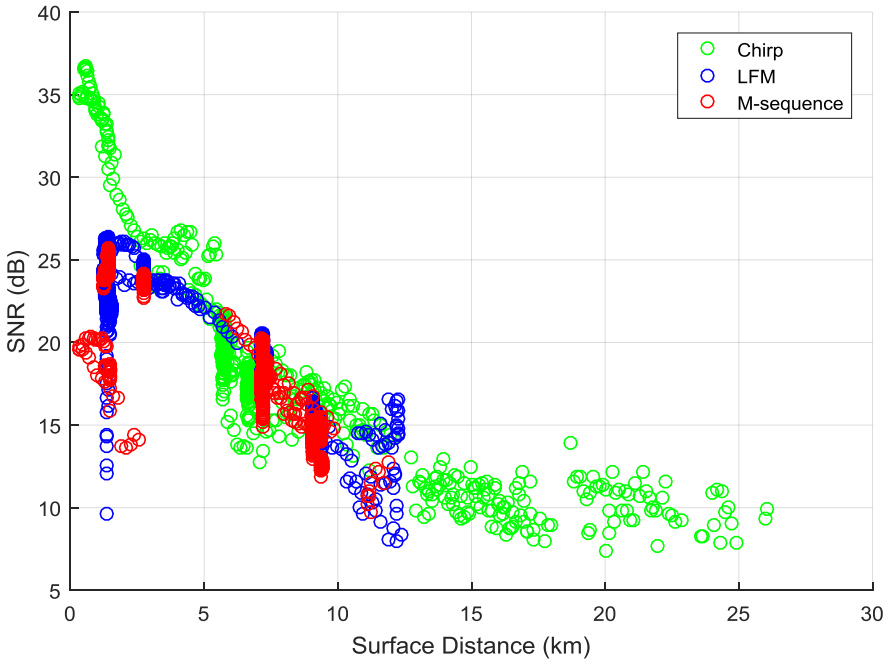

Figure 42. SNR vs. surface distance for each reception. The SNR cut-off for each type of transmission was 7 dB. Low SNR values near 0 km range correspond to BS reflected arrivals.

7. Inverse Simulations (2-D)

To resolve the sound speed field at ACO many acoustic transmissions at many ranges and azimuths will be needed. Provided enough ray paths are available, calculations can be made to provide an estimate (with error bars) for the sound speed field. The following sections go through this process of solving for a sound speed field (and hydrophone position) given a priori information and simulated data.

The total travel time (d) from an acoustic source to receiver over a ray path (Γ) is given by

$$d(t) = \int_{\Gamma} \frac{ds}{c(x,y,z,t)} + n \tag{14}$$

where s is the ray arc length, c is the sound speed, and n is the noise/error along the ray path. The sound speed and subsequently the travel time is subject to change over time. So long as the change in sound speed is much less than the original sound speed, **Equation (14)** can be linearized around this sound speed (c_o) by

$$d'(t) = \int_{\Gamma} -\frac{c'(x,y,z,t)ds}{c_o(x,y,z)^2} + n \tag{15}$$

where d' is the travel time perturbation and c' is the sound speed perturbation (Cornuelle 1985).

$$c'(x,y,z,t) = c(x,y,z,t) - c_o(x,y,z) \tag{16}$$

With the linearization for the travel time perturbation, **Equation (15)** can be rewritten in matrix form as

$$d' = \boldsymbol{G}m + n \tag{17}$$

where **G** is the observation matrix and **m** is the sound speed perturbation. Using an a priori sound speed (c_o), the ray arc lengths and subsequent travel time perturbation can be calculated along a ray path (**G** and d' are known). With this information, a sound speed perturbation can be estimated ($\hat{m}$) using stochastic linear inverse theory.

$$\hat{m} = \boldsymbol{G}^{-g} d' \tag{18}$$

Here $\mathbf{G}^{-\mathbf{g}}$ represents the generalized inverse for the observation matrix (**Equation (19)**) (Munk, Worcester and Wunsch 1995). It is an extension to the least-squares inverse, as it includes information about model errors (a priori sound speed uncertainty) and data errors (travel time uncertainty).

$$\boldsymbol{G^{-g} = PG^{T}(GPG^{T} + C_{d})^{-1}} \tag{19}$$

For **Equation (19)** P represents the model uncertainty and $\mathbf{C}_d$ are the data errors due to travel time uncertainty. This allows the user to have more control during the inversion by accounting for known sources of error. If P were equal to the identity matrix and $\mathbf{C}_d$ was a zero matrix, the generalized inverse would match that of least-squares. In other words, the a priori sound speed uncertainty would be constant, spatially uniform, and independent, and there would be no travel time errors (Munk, Worcester and Wunsch 1995).

Using the information above, a sound speed field for the surrounding area of ACO can be estimated using data collected from the experiment(s) conducted. For this time independent 2-D model, the field is separated into a discrete array of M pixels that represent the depth averaged sound speed for each. **Equation (15)** becomes

$$d' = \sum_{i=1}^{M} -\frac{c'(i)\Delta xy(i)}{c_o(i)^2} + n \tag{20}$$

where the integral becomes a summation due to the discretization of the sound speed field, the a priori sound speed and perturbation are no longer time dependent, and Δxy represents the horizontal distance a ray travels in a pixel i.

An example of this 2-D model is detailed below using a simulated ocean sound speed field (**Figure 43**) derived using a Gaussian covariance matrix (a priori model error)

$$\boldsymbol{P} = \begin{bmatrix} \Delta c^2 * \exp\left(-\frac{pixel_{11}}{\sigma^2}\right) & \cdots & \Delta c^2 * \exp\left(-\frac{pixel_{M1}}{\sigma^2}\right) \\ \vdots & \ddots & \vdots \\ \Delta c^2 * \exp\left(-\frac{pixel_{1M}}{\sigma^2}\right) & \cdots & \Delta c^2 * \exp\left(-\frac{pixel_{MM}}{\sigma^2}\right) \end{bmatrix} \tag{21}$$

where M is the number of pixels, Δc is the a priori sound speed uncertainty (here 1 m/s), $pixel_{ij}$ is the distance between the center of two respective pixels, and σ is the Gaussian covariance length. Here the diagonal terms are equal to Δc^2 (variance of sound speed uncertainty) and the off-diagonal terms represent the sound speed correlation between pixels separated by the distance pixel_{ij}. The a priori sound speed uncertainty (Δc) for this particular simulation is arbitrarily chosen, because an eddy passing through the water column is capable of causing a depth averaged sound speed difference of approximately 1 m/s. The covariance length (σ) is also arbitrarily chosen to be 20 km for this model. This is a conservative estimate as ocean scale lengths are typically longer, on the order of 100 km or more, so it allows for more variability in the model area of, for instance, submesoscale variability. The simulated sound speed perturbations are generated with

$$m = chol(\boldsymbol{P}) * rand_{norm} \tag{22}$$

where chol(**P**) represents the Cholesky decomposition of the Gaussian covariance matrix and $\text{rand}_{\text{norm}}$ is a vector of random normally distributed numbers with a mean of 0.

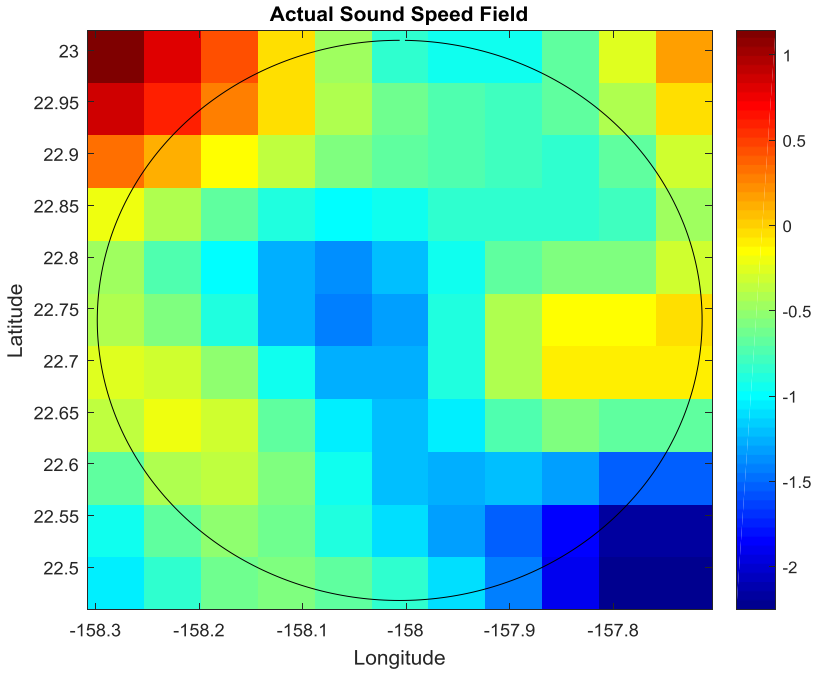

Figure 43. Sample simulation of an 11x11 ocean sound speed field. The color bar represents the sound speed perturbation (m/s) from the a priori field.

Acoustic transmissions can now be sent through this simulated ocean. **Figure 44** shows the transmission paths from the vessel to the hydrophone for this example. **Figure 45** shows the travel time perturbation (*d*), which is the difference between the actual travel time through the sound speed field and the estimated travel time through the a priori sound speed field (1506 m/s). For this particular example, the distribution of the simulated sound speed field produces travel time perturbations that are all positive just by coincidence and is not a property that would hold for other examples.

Using the acoustic paths in **Figure 44**, the appropriate observation matrix can be formed by the following

$$\boldsymbol{G} = \begin{bmatrix} -\frac{\Delta xy_{11}}{{c_o}^2} & \cdots & -\frac{\Delta xy_{1M}}{{c_o}^2} \\ \vdots & \ddots & \vdots \\ -\frac{\Delta xy_{N1}}{{c_o}^2} & \cdots & -\frac{\Delta xy_{NM}}{{c_o}^2} \end{bmatrix} \quad \textbf{(23)}$$

where N represents the number of transmissions and c_o represents the constant a priori depth averaged sound speed used. With **Equation (19)**, the generalized inverse includes a travel time error ($\mathbf{C}_d$) and for these simulations we assume a constant RMS error of 0.2 ms.

With the travel time perturbation (*d*) and the generalized inverse ($\mathbf{G}^{-\mathbf{g}}$) computed, an estimated sound speed field can be calculated using **Equation (18)**. **Figure 46** (bottom left) shows the estimated sound speed field and **Figure 46** (top right) shows the difference between the true and estimated sound speed field. As expected, the model replicates the true sound speed field much better within the circle where the acoustic transmissions took place. Looking at this more in-depth **Equation (24)** is used to compute the a posteriori covariance matrix for the model's sound speed estimates (Tarantola 1987).

$$\boldsymbol{P}_{post} = (\boldsymbol{I} - \boldsymbol{G}^{-g}\boldsymbol{G})P \quad \textbf{(24)}$$

Here I represents the identity matrix and $\mathbf{G}^{-\mathbf{g}}\mathbf{G}$ represents how well the model is able to resolve the field. The a posteriori errors become a weighted reduction of the a priori errors determined by this model resolution matrix ($\mathbf{G}^{-\mathbf{g}}\mathbf{G}$). Confirming the previous results, **Figure 46** (bottom right) shows the RMS a posteriori errors for the model and the largest errors occur outside of the region with transmissions.

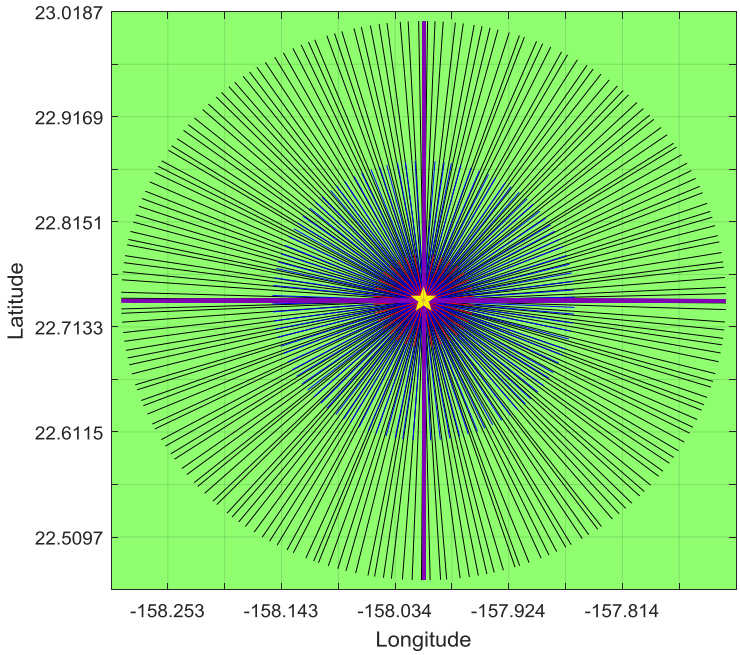

Figure 44. Acoustic transmission paths for sample case at 5 (red), 15 (blue), and 30 km (black). Also, included are transmissions for paths traversed across the entire diameter of the area of interest (purple).

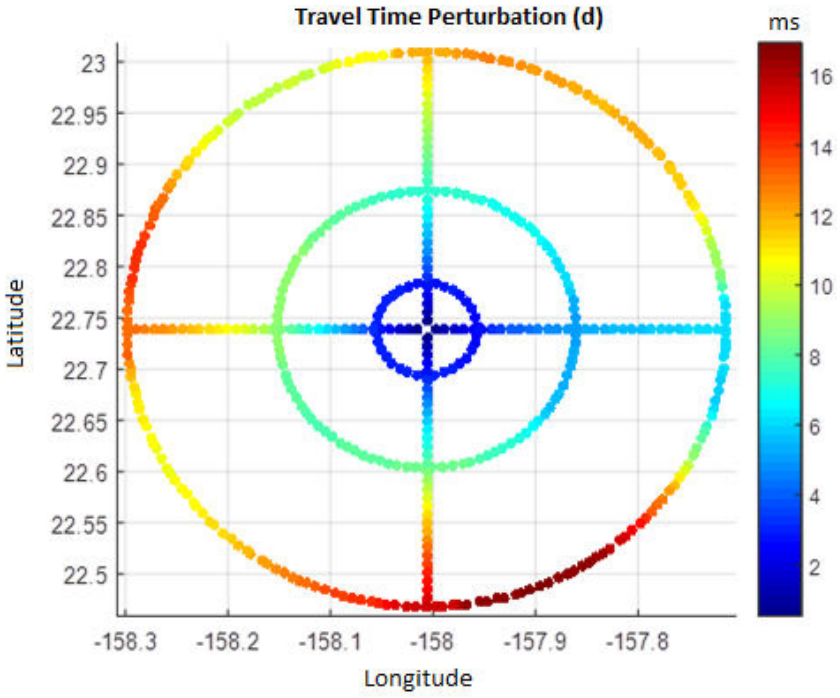

Figure 45. Travel time difference between the actual and estimated travel times for each acoustic transmission.

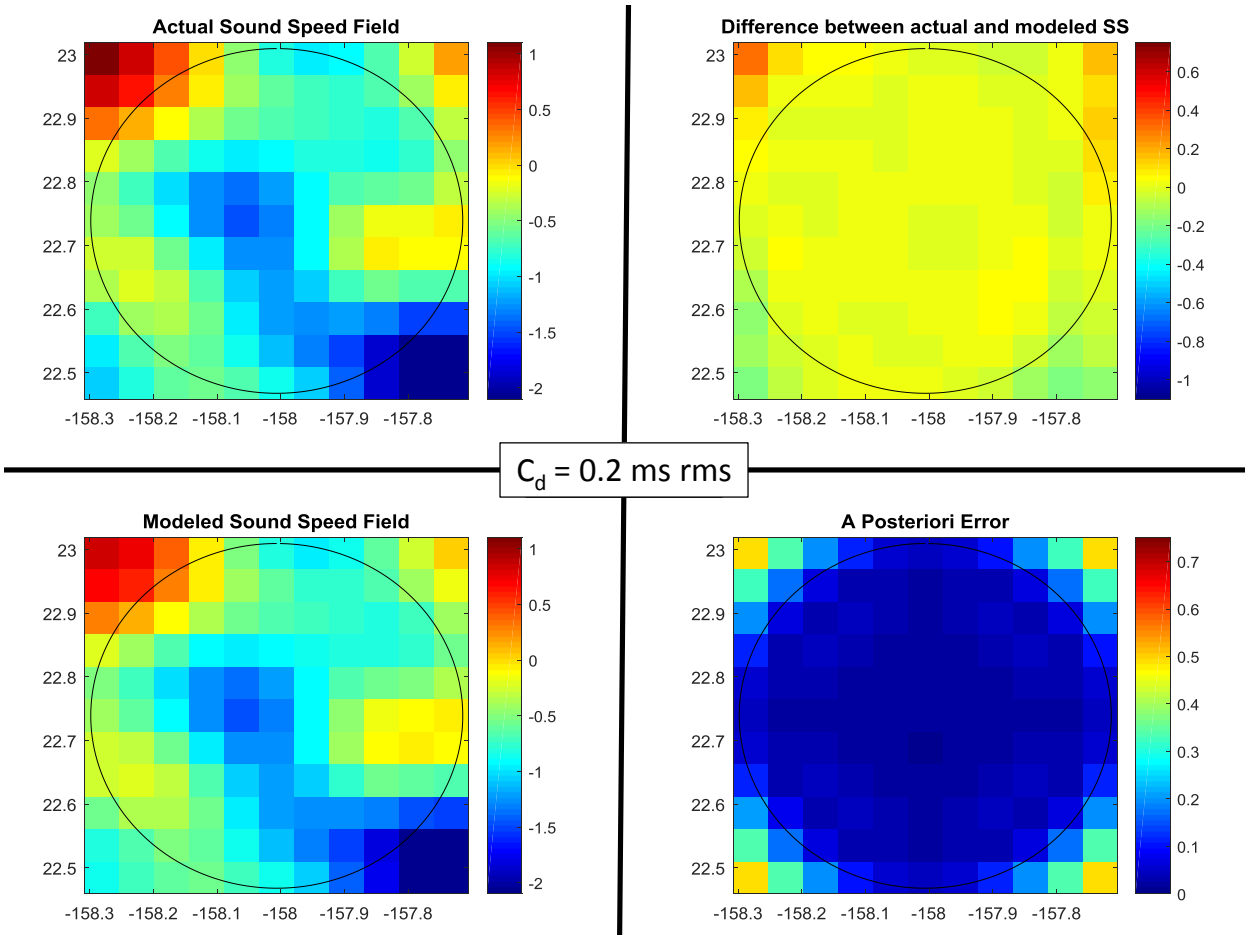

Figure 46. (Top Left) Simulated ocean sound speed field. (Bottom Left) Estimated sound speed field for the ocean simulation. The color bar represents the sound speed perturbation from the a priori field (m/s). (Top Right) Difference between simulated and estimated sound speed field (m/s). (Bottom Right) A posteriori error (m/s) for the estimated sound speed field.

8. Hydrophone Positioning

The locations of the instruments deployed at ACO have been continuously calculated using ship-based coordinates during ROV dives through time (**Figure 2**). The instruments position estimates are accurate enough for most purposes, but when attempting to perform RAP Tomography we need the hydrophone's position accuracy down to the centimeter level.

To find a "new" best estimate for the hydrophone position stochastic linear inverse theory, **Equations (17)-(19)**, can again be used. For this problem *d* again represents the travel time perturbation, or the time difference between actual and estimated travel times due to a hydrophone offset from the original estimate. **G** (observation matrix) relates the travel time data to the bottom mounted hydrophone position (**Figure 47**) (assuming the ship position uncertainty is very small relative to the hydrophone position uncertainty).

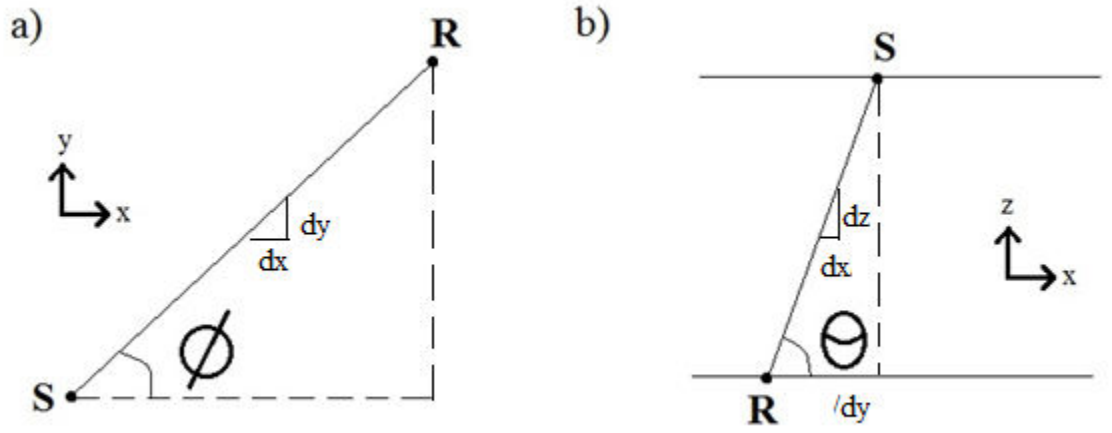

Figure 47. a) Phi represents the angle of the acoustic sources position (S) to the receiver (R) with respect to the x-y direction (on the sea surface). b) Theta represents R's angle with respect to S with respect to the x-z direction (water column). (dx, dy, and dz show the small increments between the source and receiver)

It is a Nx3 matrix, where N is the number of acoustic transmissions and 3 corresponds to the three dimensions. m is a 3x1 vector representing the difference between the true and estimated

position for x, y, and z. The change in travel time with respect to the horizontal position is given below

$$\frac{\partial d}{\partial X} = \frac{\partial d}{\partial R} \cdot \frac{\partial R}{\partial X} \tag{25}$$

$$\frac{\partial d}{\partial Y} = \frac{\partial d}{\partial R} \cdot \frac{\partial R}{\partial Y} \tag{26}$$

where

$$\frac{\partial R}{\partial X} = cos\phi \tag{27}$$

$$\frac{\partial R}{\partial Y} = sin\phi \tag{28}$$

from **Figure 47**, which relates the source and receiver surface position. The remaining terms that need to be included in the observation matrix take into account the received ray angle (θ_r) and sound speed at the receiver (c_r) (Cornuelle 1985). Equations **(29)** and **(30)** are the ray parameters.

$$\frac{\partial d}{\partial R} = \frac{cos\theta_r}{c_r} \tag{29}$$

$$\frac{\partial d}{\partial Z} = \frac{sin\theta_r}{c_r} \tag{30}$$

With **Equations (25)-(30)** the observation matrix can be derived

$$\boldsymbol{G}_x = \begin{bmatrix} \frac{cos_1\phi \cos_1\theta_r}{c_r} \\ \vdots \\ \frac{cos_N\phi \cos_N\theta_r}{c_r} \end{bmatrix} \tag{31}$$

$$\boldsymbol{G}_y = \begin{bmatrix} \frac{sin_1\phi \cos_1\theta_r}{c_r} \\ \vdots \\ \frac{sin_N\phi \cos_N\theta_r}{c_r} \end{bmatrix} \tag{32}$$

$$\boldsymbol{G}_z = \begin{bmatrix} \frac{\sin_1\theta_r}{c_r} \\ \vdots \\ \frac{\sin_N\theta_r}{c_r} \end{bmatrix} \quad (33)$$

$$\boldsymbol{G} = [\boldsymbol{G}_x \quad \boldsymbol{G}_y \quad \boldsymbol{G}_z] \quad (34)$$

Equation (34) shows the observation matrix to estimate a new hydrophone position. ϕ and θ represent the source and receivers relative angles to one another (**Figure 47**) (Cornuelle 1985) (Van Uffelen, et al. 2016).

Instead of using a Gaussian covariance matrix for the a priori model error (**P**), we use an uncertainty for the hydrophone's x, y, and z position in a diagonalized matrix.

$$\boldsymbol{P} = \begin{bmatrix} \Delta x & 0 & 0 \\ 0 & \Delta y & 0 \\ 0 & 0 & \Delta z \end{bmatrix} \quad (35)$$

Equation (19) and subsequently **Equation (18)** can be used to find the new hydrophone position estimate.

9. Inverse Simulations (3-D)

The 2-D ocean model discussed in the previous section provides a good first order approximation of the true sound speed field for a given area. To provide a more accurate representation of the sound speed field, a third dimension must be included to represent the ocean's depth. Including a depth dependence provides a better understanding of the amount of time and distance an acoustic ray travels through a given volume.

With the 2-D model an acoustic ray may travel the same horizontal distance in two separate pixels. When the ray arc length is taken into account, the distance the acoustic ray actually travels in both pixels is not necessarily equal (in fact it is highly unlikely that they are). Also in the 2-D model, as the acoustic ray travels from the source to receiver it is assumed the sound speed is constant with no depth dependence (**Equation (23)**). This simplification removes an important property of the ray trace that influences the travel time an acoustic ray spends in a certain pixel. For instance, if the ray is traveling within the SOFAR channel at a certain location it will spend a longer time at that pixel when compared to others. Therefore, more information is known about that particular pixel than the others it traveled through for that transmission.

The 3-D model is setup almost identically to that in **Section 7**, with the only difference being the observation matrix (**Equation (36)**).

$$\boldsymbol{G} = \begin{bmatrix} \sum_{z=d_{11}}^{d_{12}} -\frac{s_1(z)}{c_o(z)^2} & \cdots & \sum_{z=d_{M1}}^{d_{M2}} -\frac{s_1(z)}{c_o(z)^2} \\ \vdots & \ddots & \vdots \\ \sum_{z=d_{11}}^{d_{12}} -\frac{s_N(z)}{c_o(z)^2} & \cdots & \sum_{z=d_{M1}}^{d_{M2}} -\frac{s_N(z)}{c_o(z)^2} \end{bmatrix} \quad (36)$$

The observation matrix is now depth dependent where d_{11} and d_{12} represent the depths at which the acoustic ray is in that pixel, $s(z)$ represents the arc lengths for a particular transmission, and $c_o(z)$ represents the a priori sound speed profile.

Using the new observation matrix, from **Equation (20)** and following the same steps from **Section 7**, the estimated sound speed field again is a depth averaged value. Each depth the

acoustic ray travels through has an equal weight on the travel time perturbation. In reality though, the sound speed variation does not occur evenly or even throughout the entire water column. In this case, most of the travel time perturbation can be attributed to a particular section or depth range for the acoustic ray. In the next paragraphs, the depth weighting is discussed.

Figure 48 shows 114 different sound speed profiles that were taken at/near ACO and at all different times of the year, from 1988 through 2017. Without even taking into account seasonal variability, it is clear that there is little to no variation in the sound speed below 2000 dbar. So it would be safe to assume when an acoustic ray travels below this depth it will provide almost no information for that particular location and it will have almost no effect at that point on the travel time perturbation. To get a better idea where most of the variation is occurring, an average sound speed profile is calculated for each month to remove any seasonal variability.

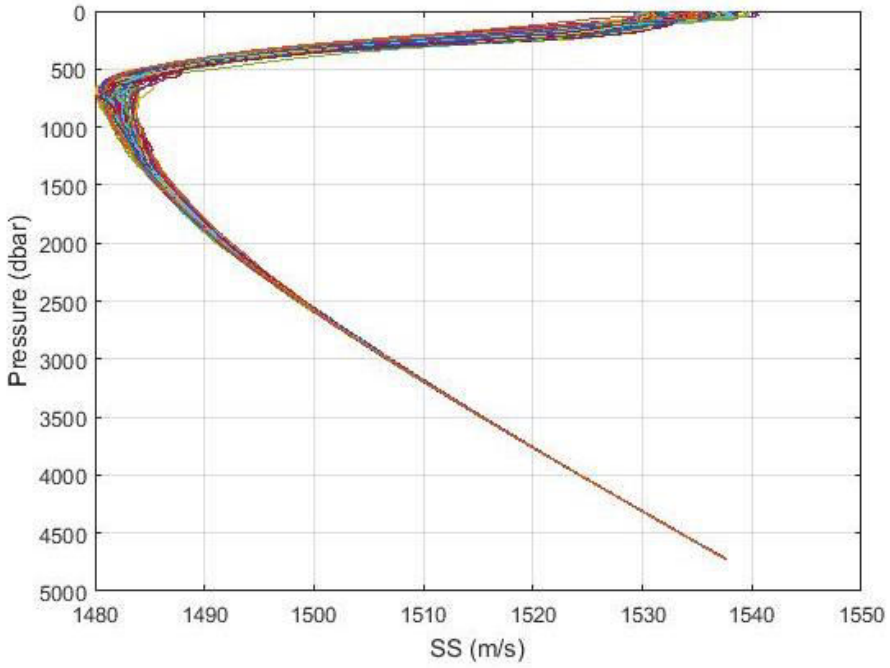

Figure 48. Sound speed profiles derived from 114 different HOTS CTD casts.

Figure 49 shows the offsets for each sound speed profile from these mean profiles. We see the largest sound speed anomalies occur around the 250 dBar mark and nominally exponentially

decay with depth. **Figure 50** plots the RMS values for the sound speed anomalies. Again, we see a maximum peak at 250 dBar of about 4 m/s RMS, which would correspond to a 1 ˚C change in the water temperature (Munk, Worcester and Wunsch 1995). Seeing these two figures we should expect the travel time perturbation to be heavily weighted at this depth when compared to deeper depths. Empirical orthogonal functions (EOFs) can be calculated using this data and included in the observation matrix to perform these weightings.

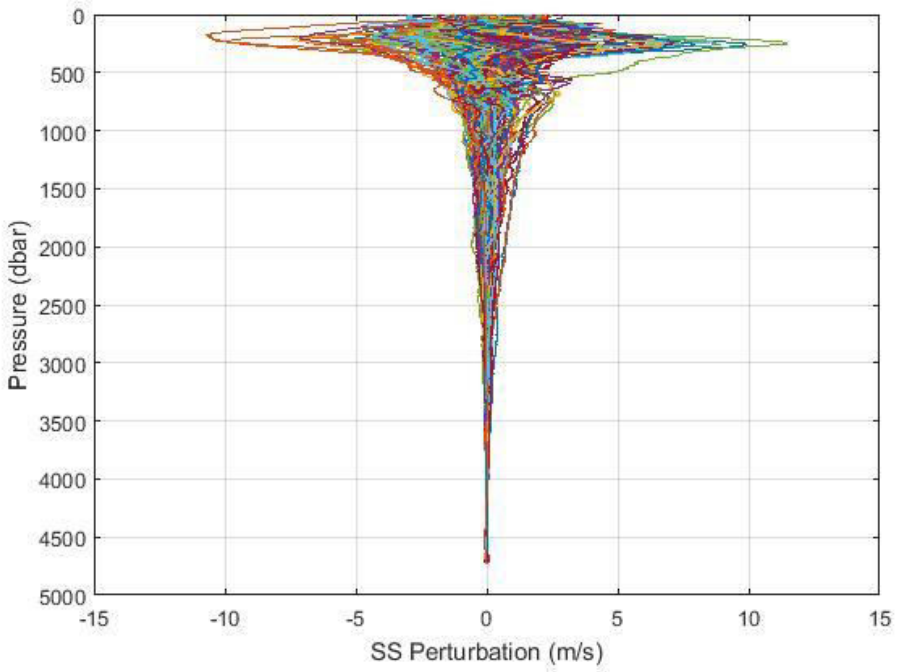

Figure 49. Sound speed perturbations (anomalies) for the profiles in **Figure 48**. All perturbations are relative to a monthly average.

To find the EOFs, a covariance matrix (**A**) for the sound speed anomalies (δc; length of the vector given by the number of points in the vertical) must first be formed by

$$\boldsymbol{A} = \frac{1}{N} < \delta c \delta c^T > \quad (37)$$

where *N* is the number of sound speed profiles (in this case 114). The covariance matrix is then used to find eigenvectors (v; also called Empirical Orthogonal functions or EOFs) that provide a solution for **Equation (38)**.

$$\boldsymbol{A}v = \lambda v \tag{38}$$

Here the eigenvalue (λ) is just a scalar, so the covariance matrix transforms an eigenvector into a scalar multiple of itself. Another way to view this is provided by

$$(\boldsymbol{A} - \lambda \boldsymbol{I})v = 0 \tag{39}$$

where **I** is an NxN identity matrix. Both **Equations (38) and (39)** do not have a unique solution and there are generally an infinite number of orthogonal eigenvectors and eigenvalues that satisfy them (North, et al. 1982).

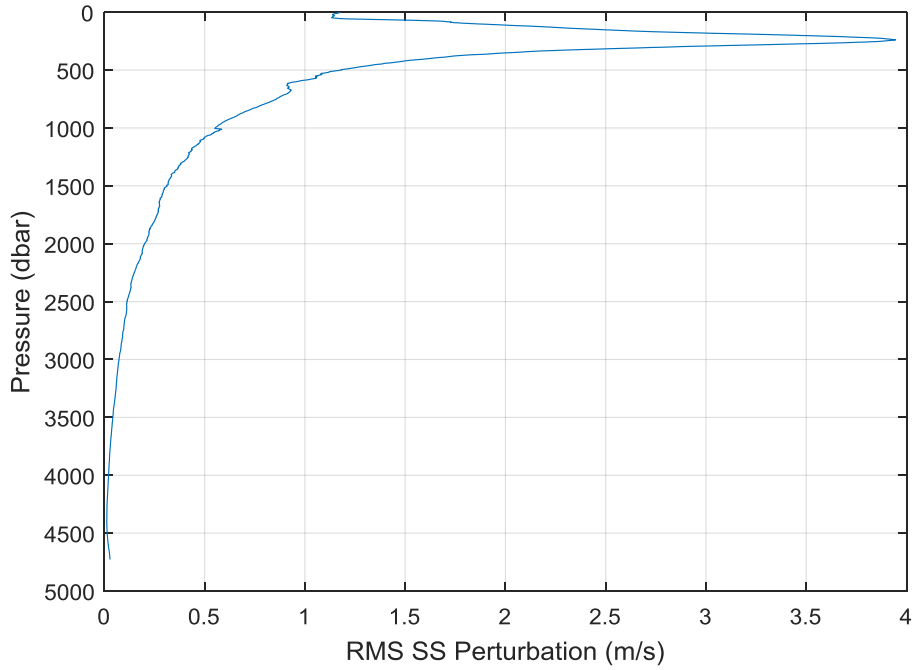

Figure 50. RMS sound speed perturbations (anomalies) from **Figure 49**.

For the purposes of this model we only concern ourselves with the first mode EOF. The first mode is the eigenvector and eigenvalue that represents the largest fraction of the data anomalies

variance. **Figure 51** plots the computed first mode eigenvector for the sound speed anomalies. This eigenvector represents about 68% of the variance in the sound speed. **Figure 52** takes a look at the second modes eigenvector, which only represents 9.6% of the variance and its integral over the entire depth is near zero. This would cause the effects of the travel time perturbation to cancel out over an acoustic path since we do not have resolution in the z direction (need crossing ray paths).

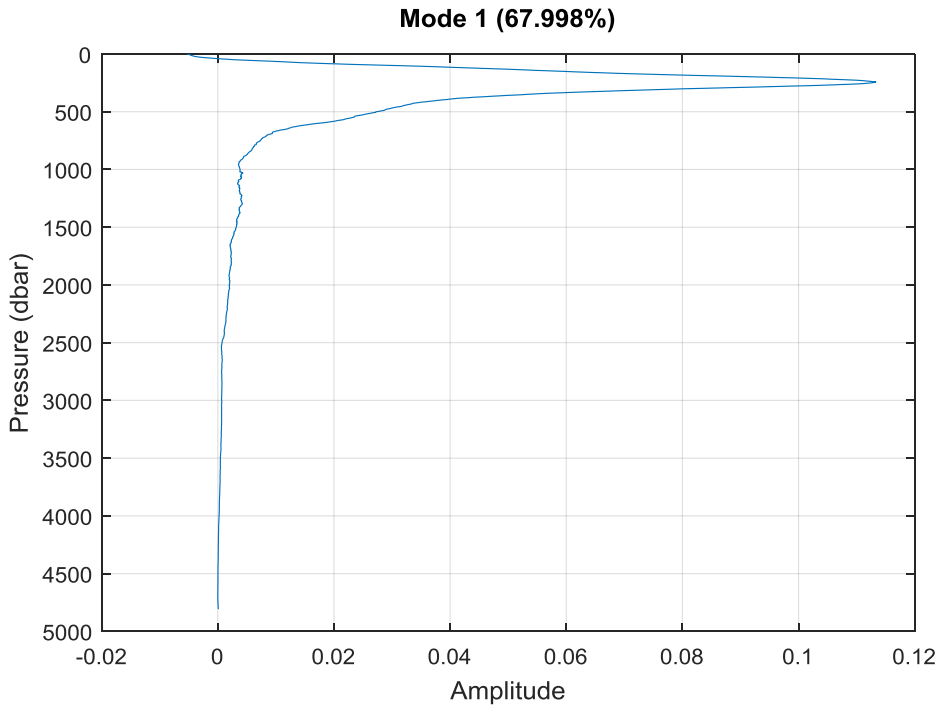

Figure 51. First mode eigenvector for the sound speed anomalies in **Figure 49**. The first mode represents almost 68% of the variance.

In a physical sense, the eigenvectors values represent the weights for each depth, the amount of sound speed variance, where the square root of the eigenvalue is the RMS sound speed change. With these defined, the eigenvector can be scaled and normalized to have a peak amplitude of 1. The eigenvalue must then be scaled appropriately to satisfy **Equations (38) and (39)** and then it becomes 14.66. Using this eigenvector and eigenvalue, we now know the sound speed can vary up to 3.83 m/s at the depth with the first EOF mode having a peak amplitude of 1.

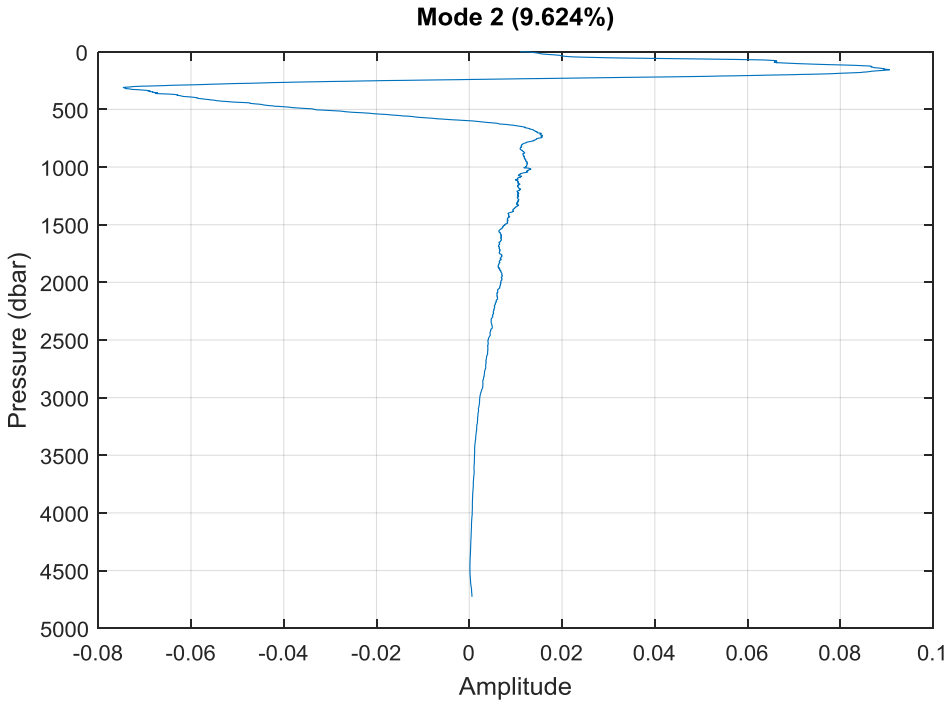

Figure 52. Second mode eigenvector for the sound speed anomalies. The second mode only represents about 9.6% of the variance.

To include this first mode in the sound speed model, the observation matrix from **Equation (20)** becomes

$$\boldsymbol{G} = \begin{bmatrix} \sum_{z=d_{11}}^{d_{12}} -\frac{v(z)s_1(z)}{c_o(z)^2} & \cdots & \sum_{z=d_{M1}}^{d_{M2}} -\frac{v(z)s_1(z)}{c_o(z)^2} \\ \vdots & \ddots & \vdots \\ \sum_{z=d_{11}}^{d_{12}} -\frac{v(z)s_N(z)}{c_o(z)^2} & \cdots & \sum_{z=d_{M1}}^{d_{M2}} -\frac{v(z)s_N(z)}{c_o(z)^2} \end{bmatrix} \quad \textbf{(40)}$$

where *v(z)* represents the first EOF eigenvector. The square root of the eigenvalue is then directly equal to the a priori sound speed uncertainty. With these adjustments made the 3-D model will solve for an estimated first mode of the sound speed field.

A similar simulation to the one in **Section 7** is modeled, but this time the observation matrix from **Equation (40)** is used. The perturbed ocean sound speed field (**Figure 43**) scales to **Figure 53**, because the sound speed uncertainty (Δc) is now equivalent to the square root of the first mode's eigenvalue (3.83 m/s). **Figure 44** shows the acoustic ray paths for this test case. An a priori sound speed field also needs to be included to compute the observation matrix. For this simulation, the sound speed field derived from a HOTS CTD cast in **Figure 35** is used. The limiting radius for this particular sound speed profile is just under 27.5 km, so the 30 km radial transmissions from **Figure 44** are adjusted to 27.45 km. The difference between these two (2.55 km) is used to reduce the latitude and longitude limits of the sound speed field to make a fair comparison between them.

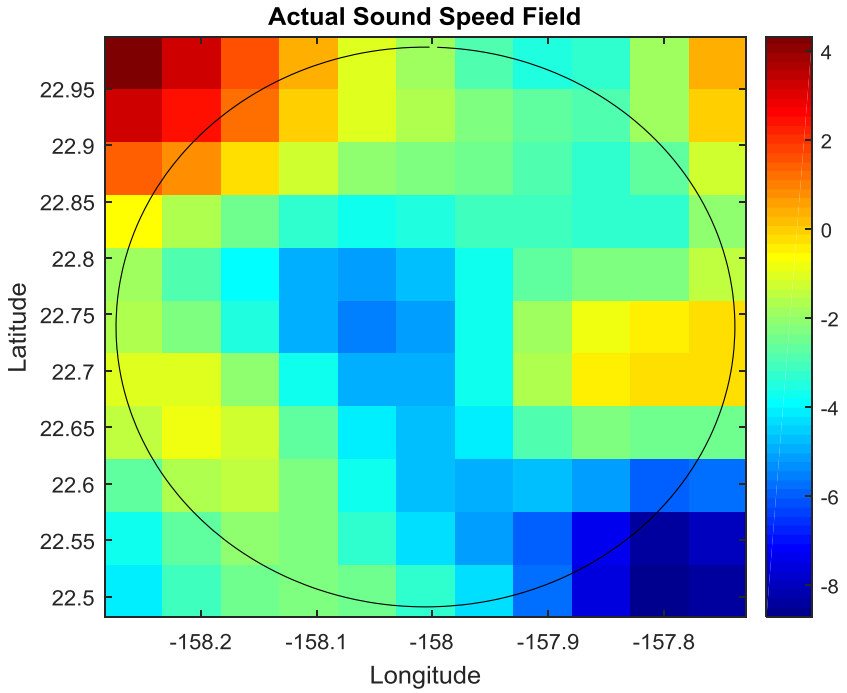

Figure 53. Sample simulation of an 11x11 ocean sound speed field (first mode). The color bar represents the sound speed perturbation (m/s) from the a priori field. Each horizontal pixel is approximately 5.5 by 5.5 km.

Figure 54 shows the travel time perturbation for each acoustic transmission. Compared to the 2-D model (**Figure 45**), these travel time perturbations are much smaller in magnitude even though

the sound speed uncertainty is much larger. This is due to the fact we are only measuring the travel time differences that arise due to the first mode EOF. Most of the travel time perturbation will be taking place in the upper 700 m of the ocean and the remaining depths will have little to no effect.

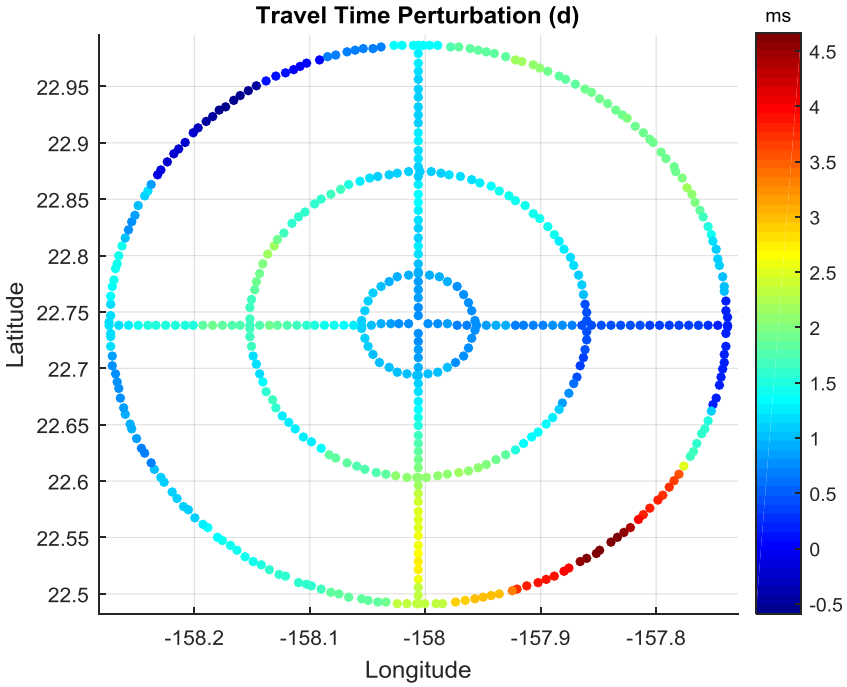

Figure 54. Travel time difference between the actual and a priori travel times (derived from range independent sound speed profile) for each acoustic transmission due to the sound speed variation from the first mode EOF.

Again, the estimated sound speed field can be calculated from **Equation (18)** and is shown in **Figure 55** (bottom left). **Figure 55** (top right) shows the difference between the true and estimated sound speed field and the largest errors occur outside of the circled area with transmissions. Compared to the 2-D model (**Figure 46**), the 3-D model has larger discrepancies when compared to its true sound speed field. This is due to the larger sound speed uncertainty (3.8 m/s compared to 1 m/s) and ultimately results in a larger sound speed perturbation field. Also, the 2-D model's discrepancies are much more uniform inside the circular area because each of those transmissions are path averaged equally. While, the 3-D model's "patchiness" results from the unequal distribution of the first mode EOF. Lastly, the RMS a posteriori errors are

given in **Figure 55** (bottom right). As expected the errors are the largest outside the range of transmissions. These errors are larger than those from the 2-D case (**Figure 46**), but again this arises from the larger a priori sound speed uncertainty for the 3-D model.

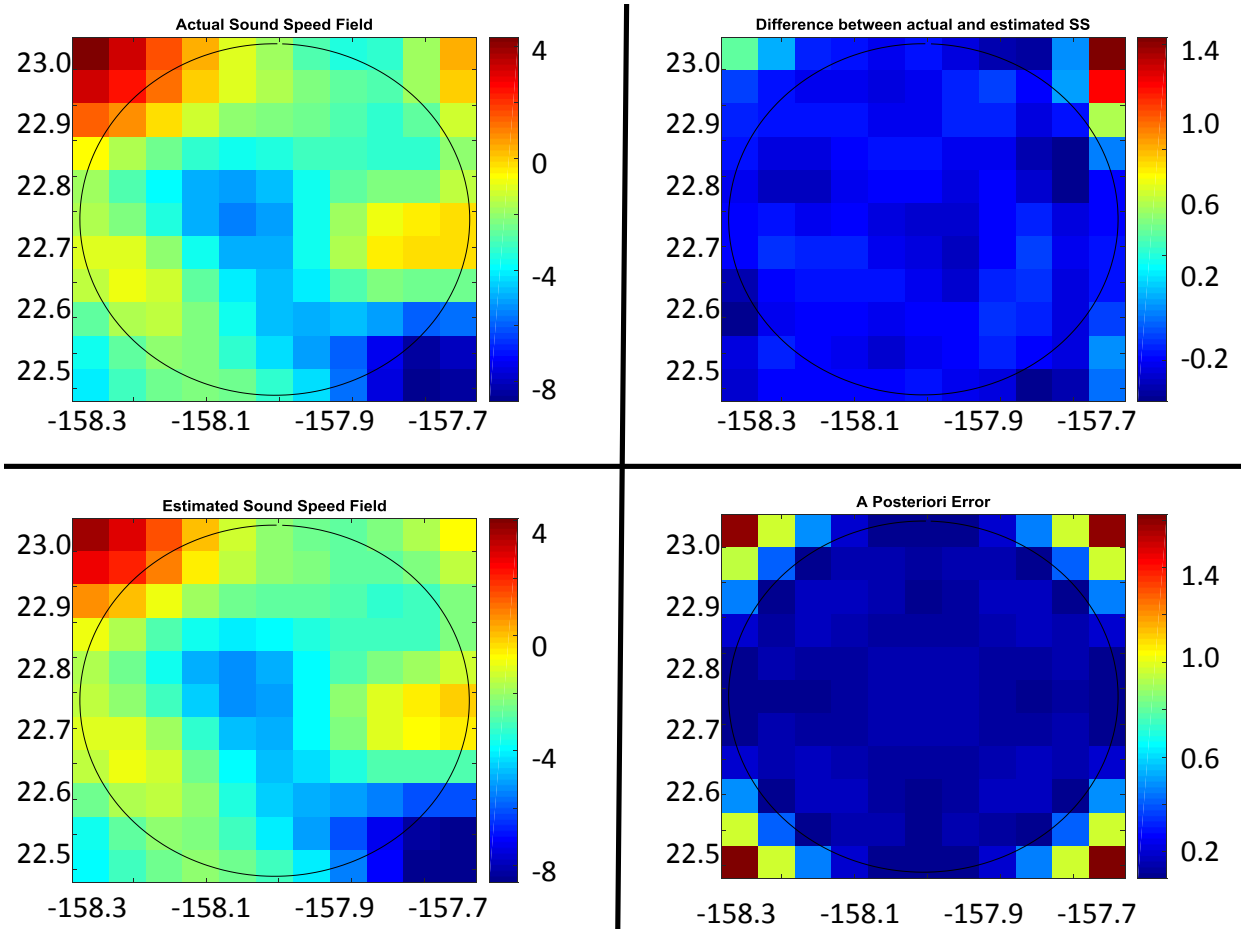

Figure 55. Estimated sound speed field for the ocean simulation in **Figure 53** and has the same scaling.

The last simulation aims to combine the 3-D model for the sound speed field with the estimation for an improved hydrophone position. Setting up this model is very similar to what has already been performed above. The main difference is in the observation matrix, where **Equation (40)** and **Equation (34)** are combined to provide information for both sound speed perturbations ($\mathbf{G}_c$) and hydrophone positioning ($\mathbf{G}_x$, $\mathbf{G}_y$, $\mathbf{G}_z$).

$$\boldsymbol{G} = [\boldsymbol{G}_c \quad \boldsymbol{G}_x \quad \boldsymbol{G}_y \quad \boldsymbol{G}_z] \tag{41}$$

Here the observation is a N by M+3 matrix where N is the number of transmissions, M is the number of pixels, and 3 represents the three degrees of freedom for the hydrophone position. The a priori model errors are combined in a similar fashion

$$\boldsymbol{P} = \begin{bmatrix} \boldsymbol{P}_c & 0 \\ 0 & \boldsymbol{P}_{xyz} \end{bmatrix} \tag{42}$$

where $\mathbf{P}_c$ is given by the Gaussian covariance matrix in **Equation (21)** and $\mathbf{P}_{xyz}$ is given with the (uncorrelated) a priori hydrophone position uncertainties in **Equation (35)**. The perturbed sound speed field and hydrophone position are calculated with **Equation (22)**. For this simulation, the sound speed uncertainty will be represented again by the first mode eigenvalue (rms of 3.8 m/s) and the hydrophone rms position uncertainty will be 10 m, 10 m, and 5 m in the x, y, and z directions, respectively. With these parameters, the sound speed field from **Figure 53** is reproduced and the simulated x, y, and z hydrophone position offsets are 25.502 m, -7.674 m, and -5.021 m, respectively. It is important to note that the pixels' sound speed perturbation and the hydrophone offsets can exceed the rms uncertainties, because **Equation (22)** uses a random normal distribution and normal distributions have infinite tails.

Figure 56 (bottom left and top right) shows the estimated sound speed and its difference compared to the true sound speed field. The model looks very similar to the case when no hydrophone offsets were included (**Figure 55**). The main difference between them occurs in the pixels at/near the hydrophone location. This is to be expected as the travel times will also differ due to the hydrophone offset and for closer transmissions this will be attributed solely to the pixels surrounding the hydrophone. **Figure 56** (bottom right) confirms this concept as the largest RMS a posteriori errors inside the circular area occur in the pixels surrounding the hydrophone's location. Meanwhile, the estimated hydrophone position offsets for x, y, and z are calculated to be 25.504 m, -7.660 m, and -4.888 m, respectively. The differences are -0.002 m, -0.014 m, and -0.133 m, respectively, consistent with (less than) their corresponding RMS a posteriori errors of 0.086 m, 0.086 m, and 0.247 m.

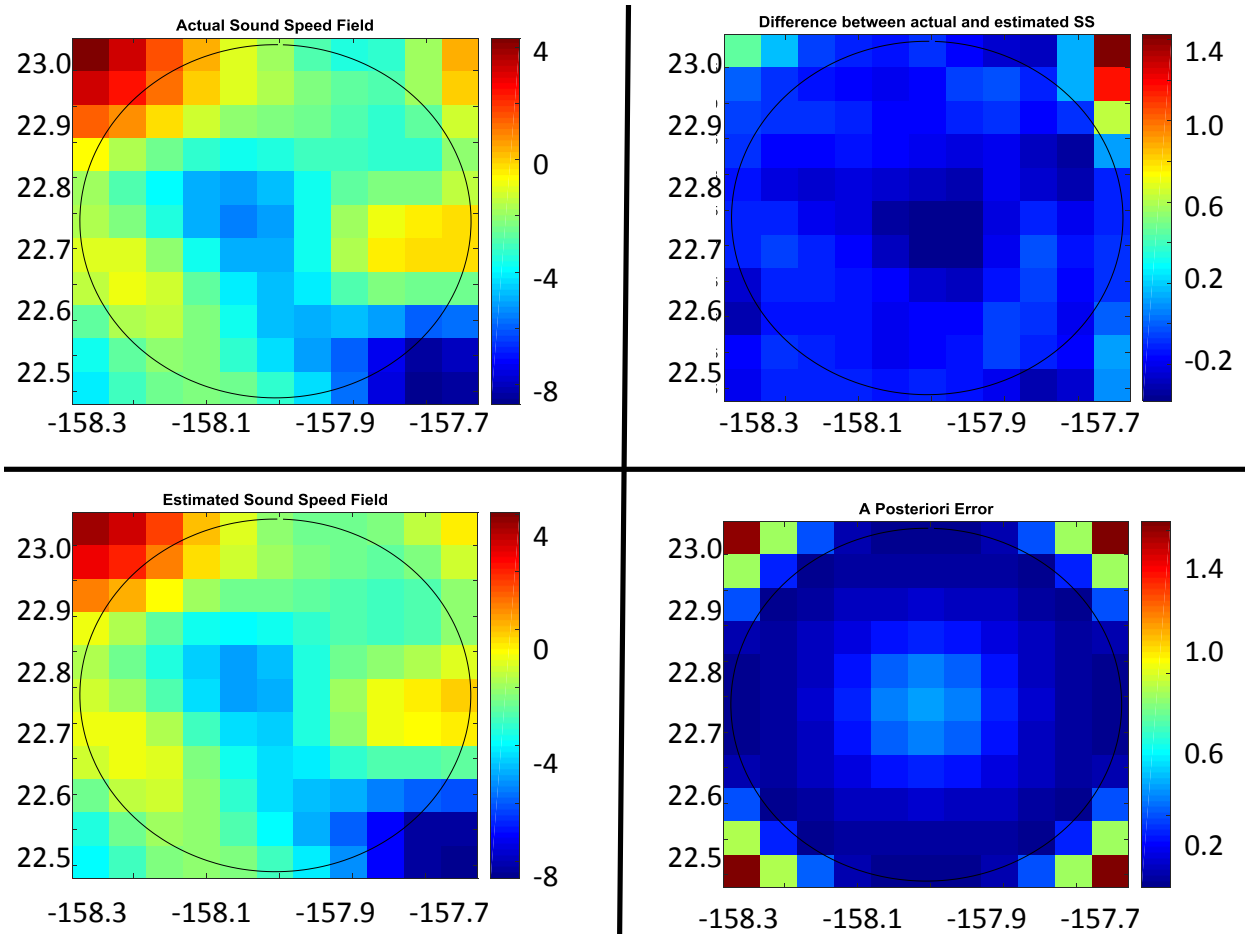

Figure 56. Estimated sound speed field for the ocean simulation in **Figure 53** when including hydrophone position offsets. The color bar represents the sound speed perturbation.

For the above simulations, a constant data error (travel time error) due to pulse width was used. When working with the real data collected and for these experiments, travel time error must also include the vessels position uncertainty. The actual travel time (d) will be affected by any offset from the true vessel position in all three directions. This travel time anomaly (B) is given

$$B = \frac{\partial d}{\partial X}\delta x + \frac{\partial d}{\partial Y}\delta y + \frac{\partial d}{\partial Z}\delta z \tag{43}$$

where δx, δy, and δz represent the offsets from the original estimated position (Cornuelle 1985). The change in travel time with respect to each direction is given by **Equations (25)**, **(26)**, and **(30)**, but instead using the ray angle and sound speed at the ship/source (θ_s and c_s) as opposed to the receiver.

The travel time anomaly variance is given as

$$B^2 = \left(\frac{\partial d}{\partial X}\right)^2 (\delta x)^2 + \left(\frac{\partial d}{\partial Y}\right)^2 (\delta y)^2 + \left(\frac{\partial d}{\partial Z}\right)^2 (\delta z)^2 \quad \textbf{(44)}$$

where the travel time anomaly in each direction is assumed to be uncorrelated, making the cross terms zero. Using these equations, at short ranges (large θ) the travel time anomaly is dominated by position uncertainty in the z direction, while at long ranges (small θ) the surface position uncertainty dominates the travel time anomaly (see **Figure 58**). Also, depending on the angle between the source and receiver (ϕ), the x and y position uncertainty will have differing weights for the travel time anomaly. The total travel time error ($\mathbf{C}_d$) matrix consists of the sum of the variances between the travel time anomaly (B) and error due to pulse width (σ_t) along the diagonal (see **Figure 58**).

With the simulations completed, the model can be used to estimate the sound speed field and hydrophone position using the January 2017 HOTS cruise acoustic data (**Section** 6). **Figure 39** shows the travel time perturbations and vessel position for the duration of this experiment. The travel time perturbations is directly used for the travel time perturbation vector, d'. The vessel position is used for ray tracing from the vessel to the hydrophone and will supply the information needed to compute the observation matrix, G (**Equation (41)**). The model error matrix (**Equation (42)**), P, remains the same from the simulation tested above. The sound speed uncertainty is determined from the first mode EOF eigenvalue and the covariance between each pixel location is Gaussian with a length scale of 20 km. The hydrophone position uncertainty is 10 m, 10 m, and 5 m in the x, y, z position, respectively. The data error matrix, C_d, is calculated using the position uncertainty of the vessel during each transmission (**Figure 32** and **Figure 33**) and the SNR for each reception (**Figure 42**). All the information needed to compute **Equation (18)** are known, so an estimated sound speed field and hydrophone position can now be calculated.

Figure 57 shows the estimated perturbed sound speed field with the acoustic paths from the vessel to hydrophone (black lines) overlaid. The estimated hydrophone offsets are 7.08 m, -7.49 m, and 17.72 m (estimated rms errors are 0.085 m, 0.055 m, and 0.226 m) for the x, y, and z position, respectively. Initially looking at these values for the sound speed field and hydrophone

positions they are implausible. The perturbed sound speed field ranges from -50 m/s to +65 m/s, which would correspond to approximately a -12 ˚C to +16 ˚C change in water temperature at the maximum first mode EOF water depth (~250 m). The hydrophone position offsets for x and y could be reasonable, but a 17.72 m offset in the z direction seems unlikely considering there is a pressure sensor at ACO. This begs the question of what is causing these inconsistencies in sound speed and hydrophone positioning estimates.

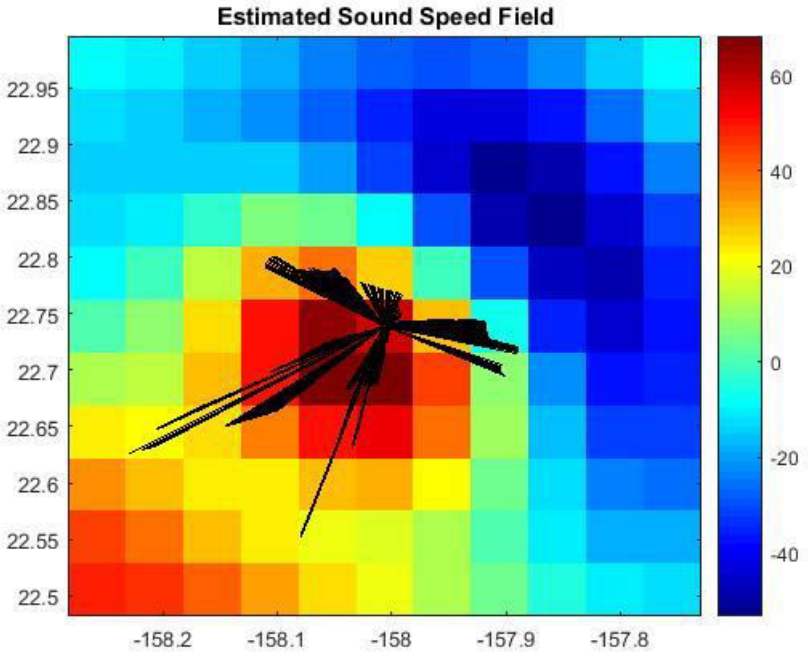

Figure 57. Estimated sound speed field during the January 2017 HOTS cruise. The color bar represents perturbations from the sound speed profile derived from the CTD cast taken during the experiment (**Figure 35**). The black lines represent the acoustic path from the vessel to the hydrophone for each transmission.

Figure 58 shows the travel time perturbations with respect to surface distance between the vessel and hydrophone for each transmission. Also in this figure are the expected travel time perturbations when including hydrophone position uncertainty and when not. There are some locations where the data falls close or within the expected travel time perturbations, but the bulk of the perturbations are much larger and do not fit within this expected region for either case. This is what ultimately allows for such large perturbations in the estimated sound speed field

(**Figure 57**) and hydrophone position offset in the z component. For the next experiment, it will be important to see if these large time perturbations are reproduced.

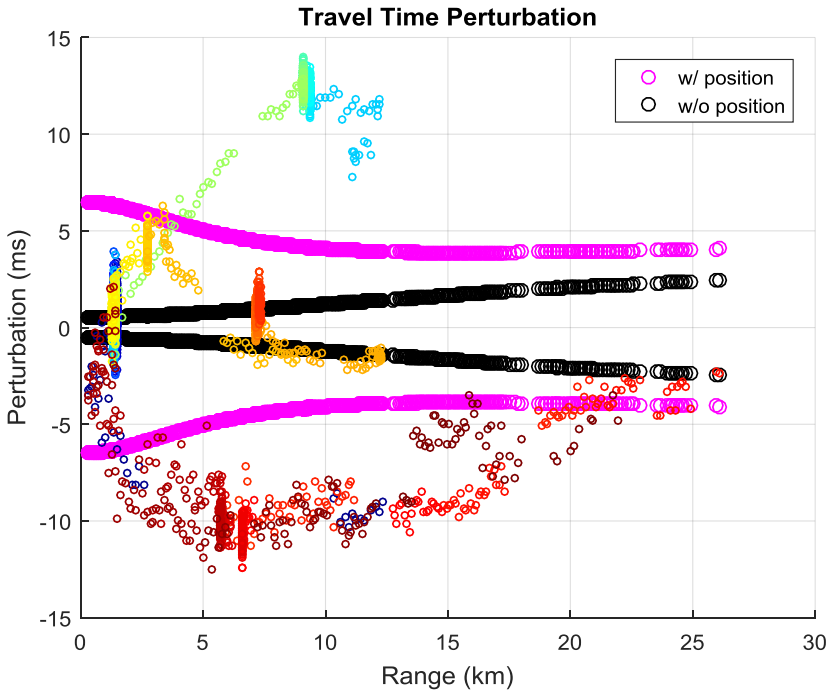

Figure 58. Travel time perturbation vs. range of vessel for the data collected from the January 2017 HOTS cruise (scattered colored dots). The expected travel time perturbation with hydrophone position uncertainty (pink) and without hydrophone position uncertainty (black) is also given for each of these points.

Figure 59 shows the data residual normalized by the travel time uncertainty with respect to the surface range for each transmission. The data residual is the difference between the actual travel time (d) and the model estimated travel time ($G\hat{m}$). This figure shows how well or not the model is able to reproduce the travel time for each acoustic transmission. Ideally all transmissions would be in between +/- 1, meaning the actual travel time and model estimated travel time agree within the travel time uncertainty (one standard deviation). Obviously this is not the case, as many of the data points fall way outside of this region. This suggests the travel times collected have too much variation and the model cannot properly resolve for this variation. Again, it will be interesting to see if this arises when collecting data from the next experiment. If so, the best

option may be averaging the total travel time for each area with a multitude of data points to prevent this behavior.

First, this will reduce travel time uncertainties and any noise present in the data. Secondly, this will allow the model to better resolve points in space that have an ample amount of transmissions. Since the fluctuation in travel time peak-to-peak was upwards of 3 ms at some locations when the vessel was stationary (**Figure 58**), the inversion and subsequently the model has a difficult time resolving for this variance in such a small location. Provided this correction the actual travel time perturbations and those predicted by the model (**Figure 59**) will converge.

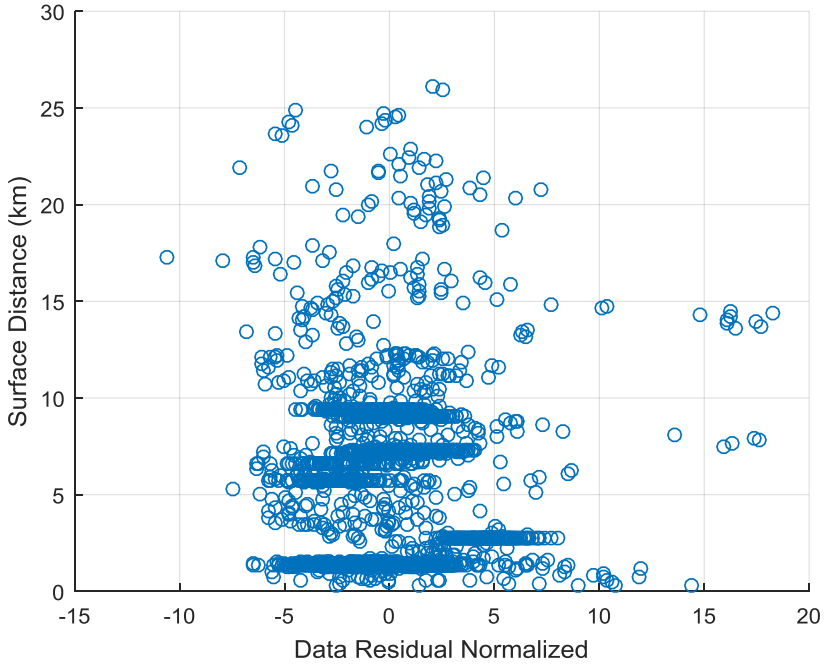

Figure 59. Plot of the difference between the actual travel times (d) and the model estimated travel times ($G\hat{m}$) normalized by the travel time uncertainty with respect to surface distance.

10. Upcoming Work

For the next experiment, the R/V *Kilo Moana* will embark on an 11 day cruise to ACO. Similar to the recent HOTS experiment (**Section 6**), transmissions will be sent for the entire duration the vessel is inside the 30 km radius around the hydrophone. This cruise will be mainly used for the recovery and deployment of instrumentation at ACO, but a few of these days will also be designated for the RAP Tomography project.

During the ACO work, the ROV will be tasked with completing the cruise objectives as it navigates around the seafloor within 10s/100s of meters of the hydrophone. Also, there will likely be a generous amount of downtime for basic ROV maintenance and possible at-sea repairs to be made. During these times, the vessel will remain more or less stationary above the hydrophone. Having this vertical acoustic path will provide a great opportunity to measure the travel time changes from the transducer to the hydrophone over a tidal cycle(s). The average sound speed for the water column at ACO is just above 1500 m/s and the tidal range is typically between 0.5 m to 1.0 m (neap and spring tides). This elevation change for the vessel through time will be seen in the positioning data provided by POS MV (**Appendix D**), resulting in a travel time difference between the extreme high and low tide between 0.333 ms to 0.666 ms (if the elevation change isn't corrected for). This would be the most conclusive test to see that we are measuring travel time changes over days correctly. As measurements are collected at increasing range, the tidal travel time signal should decrease according to the curves in **Figure 58**, because vertical changes in source/receiver position have less effect at further ranges.

This cruise will potentially decide which waveform (LFM or M-sequence) to continue using moving forward. Similar to the previous cruise, transmissions will alternate between the two signals to provide a baseline for comparison. Since we were only able to collect data for these two signals over about a day and a half, having 10+ days worth of receptions should provide sufficient data for comparisons to be made. Whichever provides the best combination of actual processing gain and arrival time resolution will be chosen as the waveform best fit for subsequent experiments.

Having dedicated ship time during this cruise will allow us the opportunity of setting particular paths for the R/V *Kilo Moana* (in contrast to paths of opportunity dictated by the HOTS project).

An ideal scenario would have the vessel run circular tracks around the hydrophone at desired radii out to our desired maximum range (30 km). Since the R/V *Kilo Moana* is capable of sailing at 12 kts, this would require about 8.5 hours of time. Decreasing the radius and/or only sailing for half the circle would significantly reduce the required allotted time (**Figure 60** and **Table 4**). Also, traversing a couple of diametrical paths in the study site would provide data for all ranges at multiple locations. Completing some of these trajectories would provide a sufficient number of acoustic paths in the volume of interest to perform a sound speed inversion with proper resolution (**Section 9**).

These radii and circumferential paths would also serve as a good test to further pinpoint the estimated location of the hydrophone at the seafloor (**Figure 2**). The symmetry of the acoustic transmissions would provide an equal error reduction in the x and y offset estimations. Also, the receptions made when the vessel is directly overhead will reduce the errors in the z estimate offsets sufficiently as well. Assuming for a constant sound speed field during the transmissions, the recorded travel times can be used to a calculate a "best" known location for the hydrophone with an associated error (**Section** 8).

Table 4. List of circular and radial paths and their corresponding total distance, time required, and approximate number of transmissions.

Radius (km)	Total Distance (km)	Time (hrs)	# of Transmissions
30	188.5	8.5	1000
15	94.25	4.25	500
10	62.8	2.8	335
5	31.4	1.4	170

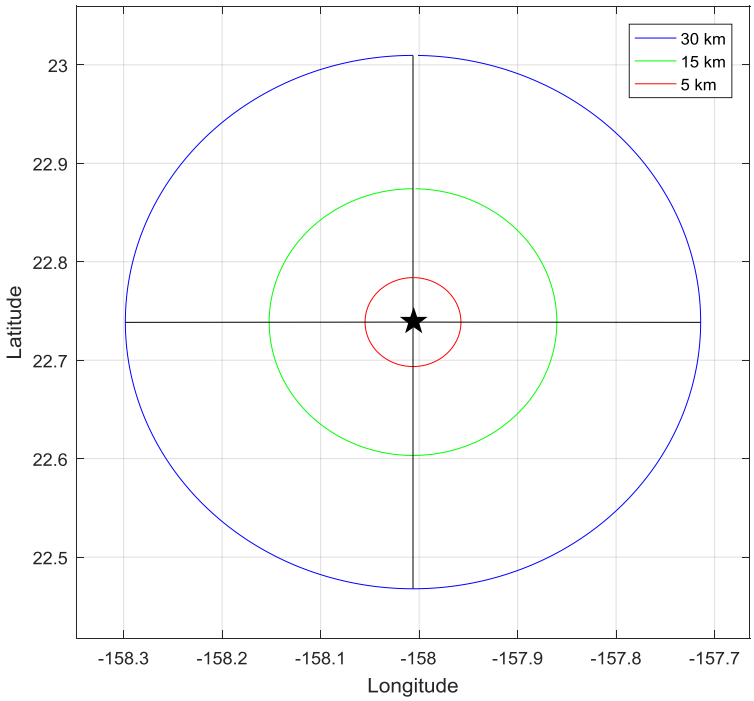

Figure 60. A few possible circular paths and two radial paths (black) that can be taken around the ACO hydrophone.

For the previous HOT cruise, a CTD cast provided the a priori sound speed profile, to determine estimated travel times and ultimately the travel time perturbation. During this cruise, expendable bathythermographs (XBTs) will be deployed in the place of a single CTD cast. An XBT is an instrument that measures the temperature profile down to a particular depth (depending on the type). These will be deployed often to help resolve changes occurring in the upper layer of the ocean and provide a time dependent a priori sound speed profile. Combining these measurements with the acoustic transmissions will provide better results when computing the inversion for the sound speed and hydrophone position estimates.

After completion of this experiment, the first thing to look for will be the SNR for the LFM and M-sequence transmissions with respect to source and receiver distance (**Figure 42**). If they are deemed insufficient for larger ranges (>15 km) changes will have to be made in order to get receptions at these larger ranges. One possibility would be to increase the duration of each signal, which will in turn increase the processing gain (**Equation (7)**). If the duration for the

signals end up increasing by a sufficient amount, Doppler shift will eventually have to be taken into account due to the movement of the vessel. Another possible way to increase the SNR would be to use another transducer. By adding a second identical power amplifier to power the second transducer or substituting a stronger power amplifier to power the two simultaneously, the power output will be doubled. While the beam pattern would be affected, it would ultimately lead to an increase in the sound pressure level (**Equation (8)**) and provide stronger receptions for the hydrophone at ACO.

11. Conclusions

This project has helped lay the groundwork for a proper RAP tomography experiment setup to accurately and precisely measure the acoustic travel time from a vessel based source to a seafloor mounted receiver. It is clear more work still needs to be done and data collected before this method can be considered for autonomous and larger scale purposes. The simulations conducted in **Sections 7 and 9** illustrate a properly functioning model that uses stochastic linear inverse theory to provide an estimated sound speed field and hydrophone position using a priori knowledge.

The inversion results for the most recent data set available produced highly unlikely sound speed estimates and is evident that the data and model are inconsistent. This will be reexamined using data collected on the next ACO cruise (June 2017). If the same inconsistencies arise then it is likely that data being collected is bad and/or the model being used is incomplete. Possible data errors could be the result of bad GPS data, travel time bias from experiment setup, non-RAP arrival contamination, or ship position error being larger than expected. While the model may have to be readjusted to accompany more degrees of freedom in the vertical direction (currently restricted to the first mode EOF), an increase/decrease of the correlation scale, and include some time-dependence.

Given these problems, the next immediate step to take will be the collection of more field data during the next ACO cruise. A main goal will be to resolve the tidal cycle using both the positioning data and through the resulting acoustic travel time changes (when not correcting for vessel altitude). This would provide the most definite test to ensure the vessel positioning and acoustic data are performing adequately and can provide sufficient resolution. Another important objective will be determining the limiting radius at which significant SNR is received at the hydrophone for both the LFM and M-sequence waveforms.

Future steps to take will be the inclusion of time-dependence in the ocean sound speed field. Currently, the model is assuming a "snapshot" view of the ocean with no changes occurring during experimentation. In real-life scenarios this is obviously not the case as eddies and other ocean phenomena are constantly traveling through the ocean, and will have some effect on the travel time perturbations through time.

Appendix A. Signal Parameters

The parameters for the M-sequence signal used in this experiment are:

Source Level	191.556 dB
Center Frequency (f_o)	4134.375 Hz
Bandwidth (BW)	1378.125 Hz
RMS Bandwidth	795.661 Hz
Digit (Q)	3 cycles = 0.725624 ms
Sequence Length (L)	31 digits
Sequence Period (Tp)	22.4943 ms
Sequence Law	45 octal (Abu-Rgheff 2007)
Sequence Initialization	00001 binary
Modulation Angle	79.8179˚

The corresponding M-sequence:

00001010111011000111111001101001

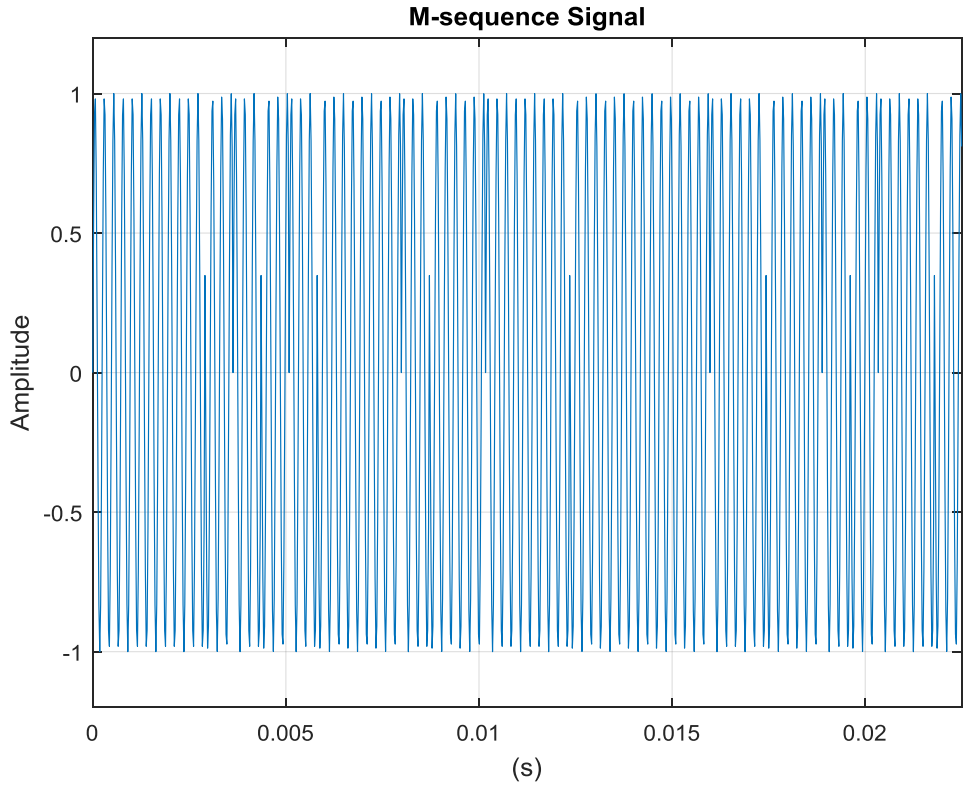

Figure 61. Computer generated M-sequence signal that is sent to the transducer.

The parameters for the LFM sweep to be used in this experiment:

Source Level	191.556 dB
Center Frequency (f_o)	4134.375 Hz
Bandwidth (BW)	1378.125 Hz
RMS Bandwidth	795.661 Hz
Signal Duration (Tp)	22.5 ms

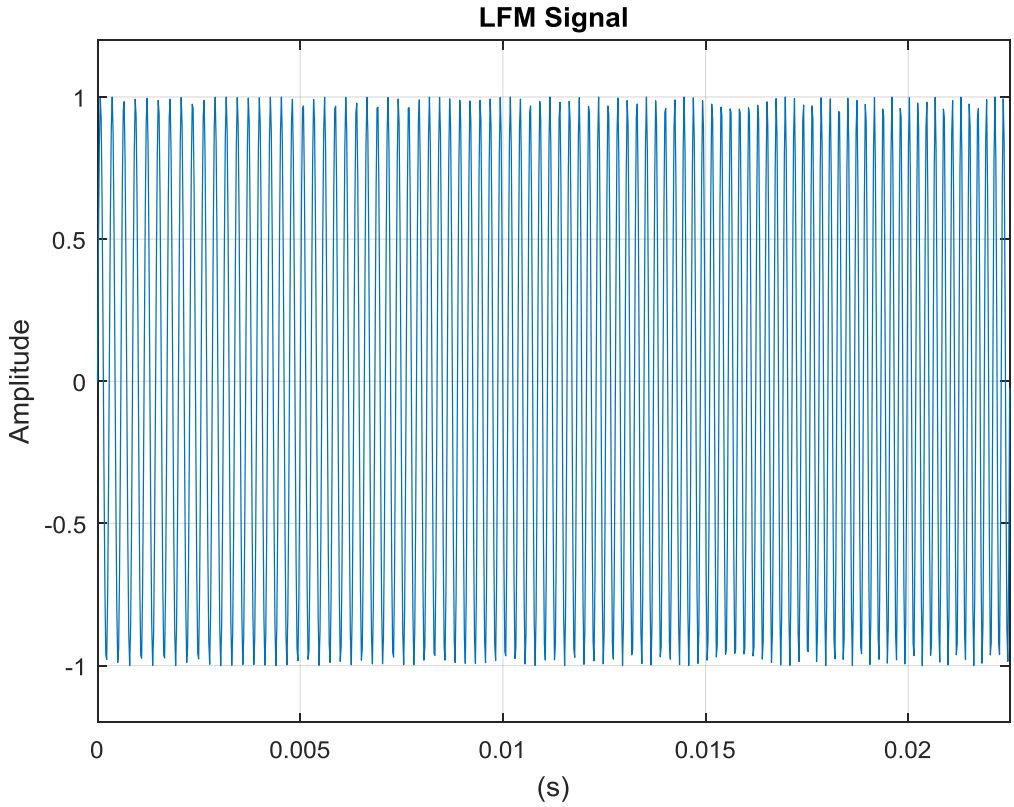

Figure 62. Computer generated LFM signal that is sent to the transducer.

Appendix B. Massa TR-1075a Specifications

The transducer is a circular piston radiating source with 1/2 wavelength diameter at 4 kHz and 80˚ conical beam angle. It is terminated with C1F2 underwater connector and mates to C1M2 underwater connector (Massa Sonic 2016).

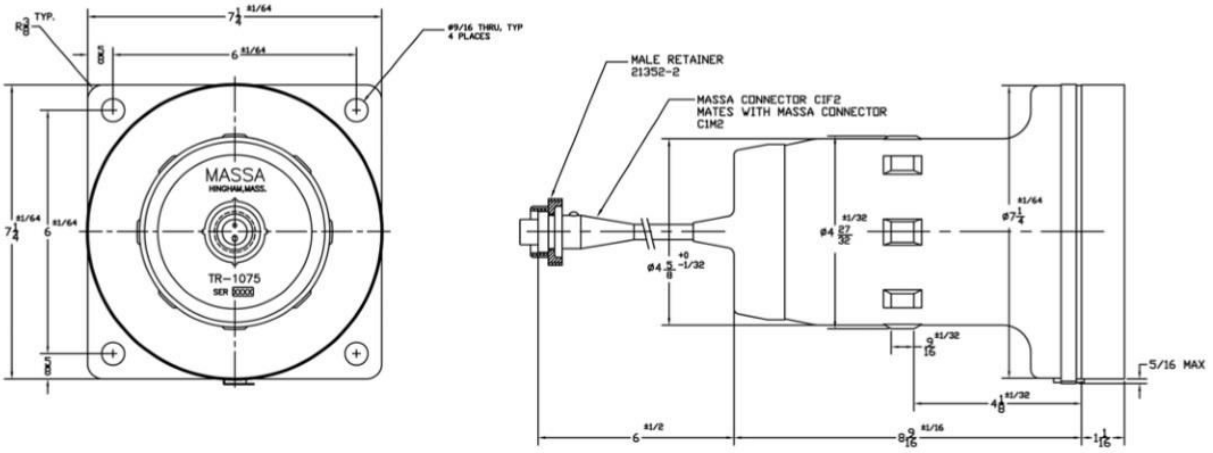

Frequency Range	2.5 - 10 kHz
Duty Cycles	600 W at 30% OR 200 W at 100%
Frequency Tuned for 0˚ Phase (Nominal)	4 kHz
Impedance Magnitude (Nominal)	100 Ω at 4 kHz
Tuning Circuit	Parallel
Weight	25 lbs

Transmitting Voltage Responses

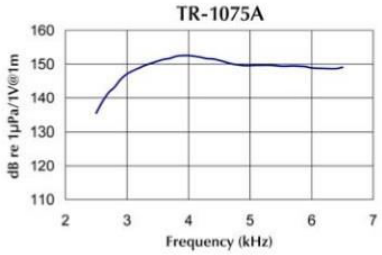

Receiving Voltage Sensitivities

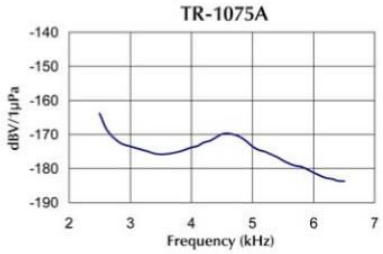

Impedance Magnitudes

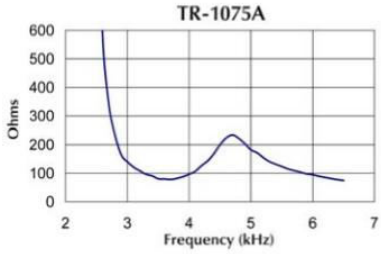

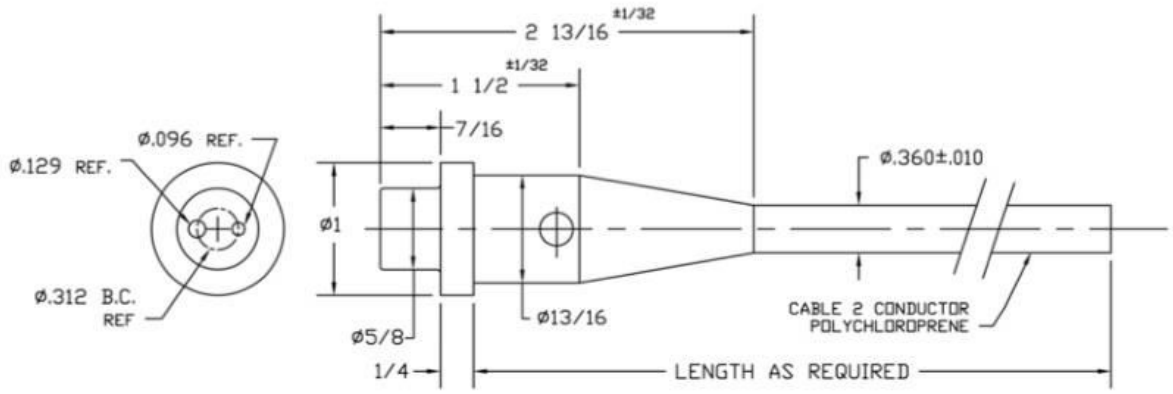

Outline Drawing of a C1M2 Male Connector for Mating to Massa Underwater Transducers
(without retaining ring)

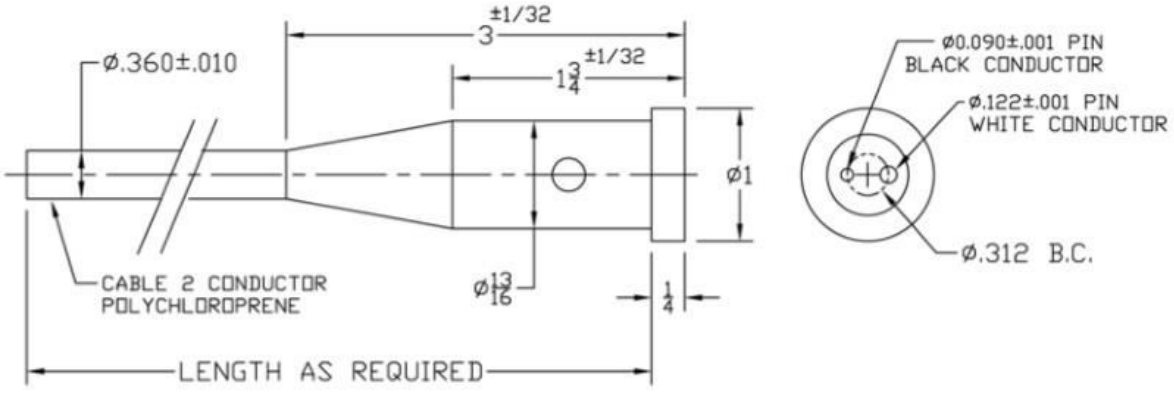

Outline Drawing of a C1F2 Female Connector Supplied on Massa Underwater Transducers
(without retaining ring)

Appendix C. HOT 289 - Cruise Log

Time (UTC)	Comments
1/23/2017 0615	Started POS-MV logging (21 51.2'N 158 15.3'W)
0651	Started LFM transmissions for 2 hours (21 52.5'N 158 15.9'W)
0726	Computer clock resynchronized with NTP server
0805	Re-started LFM transmissions for 1 hour (22 8.7'N 158 10.3'W)
0924	Clock resynchronized; started LFM for 1 hour (22 21.7'N 158 6.7'W)
1036	Clock resynchronized; started M-seq for 15 minutes (22 33.4'N 158 3.3'W)
1055	Started 15 minute LFM (22 36.5'N 158 2.9'W)
1115	Started 15 minute continuous long M-seq (22 39.7'N 158 1.5'W)
1134	Started 15 minute M-seq (22 42.9'N 158 0.6'W)
1153	Started 15 minute LFM; vessel is stationary (22 45.0'N 158 0.0'W)
1212	Started 15 minute M-seq
1233	Started 8 hour LFM
1359	Between pings 4 and 5 extra signals were registered through the reference transducer
1712	Clock resynchronized
2026	Clock resynchronized
2136	Completed 8 hour LFM
2214	5 minute LFM to icListen
2220	5 minute Mseq to icListen
2226	5 minute continuous long M-seq to icListen; icListen pulled up before finished
2232	POS-MV not functioning properly and experiencing large errors
2241	Started 2 hour LFM
2352	Clock resynchronized
1/24/2017 0100	Completed 2 hour LFM
0104	Clock resynchronized; started 15 minute continuous long M-seq
0123	Started 8 hour M-seq
0309	Clock resynchronized

0330	POS-MV starting to resynchronize with correct GPS location as vessel moves out from Station ALOHA to pump sewage
0354	POS-MV appears to be properly functioning again
0425	Stopped 8 hour M-seq; Start alternating between LFM and M-seq every 15 minute cycle
0503	Raised power of transmissions by 3 dB
0536	Clock resynchronized
0648	Clock resynchronized
0759	Clock resynchronized
0909	Clock resynchronized
1020	Clock resynchronized
1130	Clock resynchronized
1315	Clock resynchronized
1442	Clock resynchronized
1611	Clock resynchronized
2115	Clock resynchronized; Reduced transmissions by 3 dB
2209	Transmissions stopped by order
1/25/2017 1700	Knudsen echosounder is now in place of previously used power amplifier; sending transmissions through 14 transducers every 20 seconds
1721	Started 1.25 hour CW
1758	Clock resynchronized
1850	Start alternating between Chirp and CW every 15 minutes
1908	Clock resynchronized
2016	Clock resynchronized
2204	Clock resynchronized
1/26/2017 0005	Clock resynchronized
0058	Stop alternating between Chirp and CW; Send Chirp for the remaining time
0211	Clock resynchronized
0306	Transmissions completed (outside 30 km of ACO)
0314	Completed POS-MV logging

Appendix D. POS MV Data: Vessel Positioning

Overview

The R/V *Kilo Moana* is equipped with an Applanix Position and Orientation System for Marine Vessels (POS MV) OceanMaster that provides real-time accurate navigational data. This system is composed of two Global Navigation Satellite System (GNSS) receivers and antennas, an Inertial Measurement Unit (IMU), and a POS Computer System (PCS).

The PCS simultaneously retrieves the measurements made by the GNSS receivers and IMU to compute all navigational parameters and estimated errors. To produce these, a Kalman filter is used to blend the data together in a process called aided inertial navigation. When finding the vessels position the IMU provides highly accurate data in the short-term but is subject to drift over time, while the GNSS receivers have a considerable amount of noise included in the short-term but are very stable over long periods (no drift). The difference between them is computed and sent through a low-pass filter. This helps remove the short-term "noise" from the GNSS receiver data, which can then be used to remove any drift occurring in the IMU. Thus, the resulting position and estimated error includes information collected by both the GNSS receivers and onboard IMU.

The Global Navigation Satellite System (GNSS) allows a user to gain accurate and precise coordinates in real-time. A system is comprised of a GNSS antenna(s) that receive signals from orbiting satellites and a corresponding receiver(s) that collect this information to convert it into a position. There are several different functioning satellite constellations setup and run by different countries or groups of countries. For example, the GPS constellation (United States) consists of 31 satellites that fly in six different orbital planes, with each of these planes having at least 4 satellites. This ensures that any GNSS antenna will be able to receive information from at least 4 satellites at any given time, provided the antenna has a clear view of the sky (no features that can block the satellite signal). Every satellite in the GPS constellation has four very accurate clocks (clock frequency of 10.23 MHz) and are continuously transmitting two signals (L1 and L2) with differing frequencies (1.575 GHz and 1.228 GHz) and wavelengths (0.190 m and 0.244 m) at the speed of light. The constellation has an orbital radius of 26,600 km, altitude of 20,200 km, and

orbits the earth twice a day. The satellites are in constant communication with stations that are scattered around the globe. These ground stations are responsible for sending timing information to make sure each satellite is running on the same time and to track each satellites orbit through space to ensure each one knows where they are within very small errors. Other constellation systems follow the same format, but use slightly different transmitting signals and orbital altitudes. With all of this set, the satellites can provide accurate positioning and timing information for a receiving GNSS antenna to determine its position through trilateration. As satellites transmit to a given antenna, the receiver calculates the distance the antenna is from those satellites. Having these distances, the antenna is then placed on the surface of theoretical spherical shells and provided enough measurements are made a position fix is calculated where these shells meet. The calculations take into account that the signal's speed will decrease (index of refraction > 1) as it passes through the atmosphere and the atmosphere will influence the signal more the larger the angle the satellite is relative to the antenna (signal will spend a longer time in the atmosphere). Using the time delay difference for the two frequencies (higher frequency is affected less than the lower frequency), an estimation for phase advance caused by the ionosphere can be made. The troposphere effects on travel times can be negated by applying a 15 degree elevation mask, which ensures the use of satellite receptions that are closest to directly overhead. Also, calculations will employ a Kalman filter to combine all the data to provide a best single estimate for position and velocity at a given time (Oxford Technical Solutions 2017). Furthermore, the R/V *Kilo Moana* employs the services of Marinestar™ (G2) from the company FUGRO for better positioning accuracy. Their services use the satellite constellations of GPS (United States) and GLONASS (Russia) enabling the collection of more data to be used for final positioning calculations. Marinestar uses 45 ground reference stations around the Earth to determine and track each satellites precise orbit and clock errors. Also, with newer satellites being deployed that provide a larger signal and subsequent reception gain allows for better overall positioning (Visser, et al. 2016).

The POS MV system's tow GNSS receivers are referred to as the primary and secondary receivers (the designation of which is arbitrary). They are both cabled to their own antenna and must have a clear line of sight with the orbiting satellites to function properly. In the POS MV architecture, the primary receiver is responsible for the vessel positioning and velocity measurements. With the use of FUGRO (G2), they claim to provide horizontal and vertical

positioning accuracies of 0.10 m (95%) and 0.15 m (95%), respectively. It also produces a pulse per second (PPS) which provides an accurate signal for all other measurements being made. The primary and secondary receivers work together to provide the vessels heading information. The two receivers use a carrier phase differential of the L1 and L2 signals to compute their positions relative to each other and translate this into a heading for the vessel. When combined with measurements made by the IMU to account for roll and pitch, the heading is accurate to +/- 0.01˚ or better (Applanix Corporation 2016). When translating for a position that is 20 m from the antenna, this heading error will result in a 0.0035 m position error.

An inertial measurement unit (IMU) is used to calculate an object's linear and angular acceleration through time. The linear acceleration measures the acceleration in a specific direction (x, y, or z) and a linear accelerometer is typically used (excludes the force of gravity). The angular acceleration measures the rotation in a specific direction (roll, pitch, and yaw) and a gyroscope is typically used. Provided a linear accelerometer and gyroscope are positioned orthogonally in three directions, measurements will be available for all six degrees of freedom(Applanix Corporation 2016).

On the R/V *Kilo Moana* the gyroscopes and linear accelerometers are fixed in the IMU housing in a triaxial orthogonal fashion. The IMU is also fixed to the vessel and therefore these instruments will move and rotate with the vessel. This arrangement allows the IMU to calculate the vessels acceleration and angular motions in each direction. These measurements are then used to determine the current motion of the vessel. Roll and pitch measurements are accurate to 0.01˚. Errors for the gyroscope are possible through drift and random noise. Gyro drift occurs as a constant output when there is no angular motion present and this drift can be anywhere from 1-5˚ per hour for the POS MV. Random noise can occur from the internal noise characteristics of the gyroscope, resulting in a spectral noise density of $(0.07°)^2$ per hour. Errors for the accelerometer are introduced through bias and scale factor. Accelerometer bias is a constant offset in the output and changes randomly every time the IMU is powered on; these errors range from 50 to 500 μg. This range of error arises from the scale factor used on the accelerometer output and the resulting error is proportional to the sensed acceleration. For the POS MV this error ranges from 0.01% to 0.02% of the acceleration (Applanix Corporation 2016).

POS MV Data at Dock

POS MV data was logged on the R/V *Kilo Moana* at dry-dock (**Figure 75**) for a 24-hour period on March 7, 2017, with a sample rate of 2 Hz. This analysis looks at the navigational data for a reference position on the ship defined to be the vessel's granite block, which is located on the port side hull. **Figure 63** shows the initial POS MV reported error estimates for the longitude, latitude, and altitude data. The altitude is given with respect to the World Geodetic System (WGS) 84. It is apparent there are large error values at the beginning of the time record that reach almost 3 m for altitude. This can be attributed to when the POS MV was first turned on and began to synchronize itself with satellite data. Looking further in time, there is another minor peak that occurs around 18:36 and lasts for 30 seconds. These errors only reach up to ~0.35 m, but are still significantly larger than the rest of the time record that has a mean error bar of ~0.21 m as reported by the POS MV. It is unknown what exactly caused this short disturbance, but for the remaining data analysis both of these sections will be ignored.

With the bad data removed, analysis is given for the position data provided by the POS MV system and various statistics are given in **Table 5**. **Figure 64** shows the POS MV error estimates for the latitude, longitude, and altitude variables. During this stationary 24-hour time period the mean errors were 0.217 m, 0.212 m, and 0.209 m respectively. Looking closer at this figure, there are small spikes that occur sporadically for the latitude and longitude at identical times, but do not show up in the altitude data record. **Figure 65** shows a zoomed in look at one of them. We see it is one data entry causing this initial spike and then it takes about 15 s for the error estimates to return to their previous values. It is unknown what the exact cause of these is and it is strange that they do not appear in the altitude error estimates.

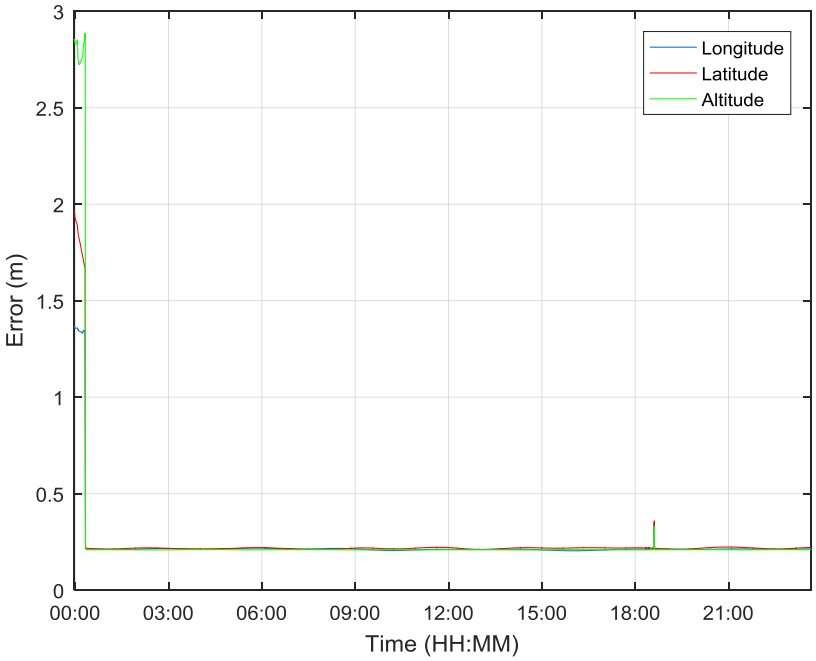

Figure 63. Initial latitude, longitude, and altitude error estimates provided by the POS MV when the R/V *Kilo Moana* was at dry-dock.

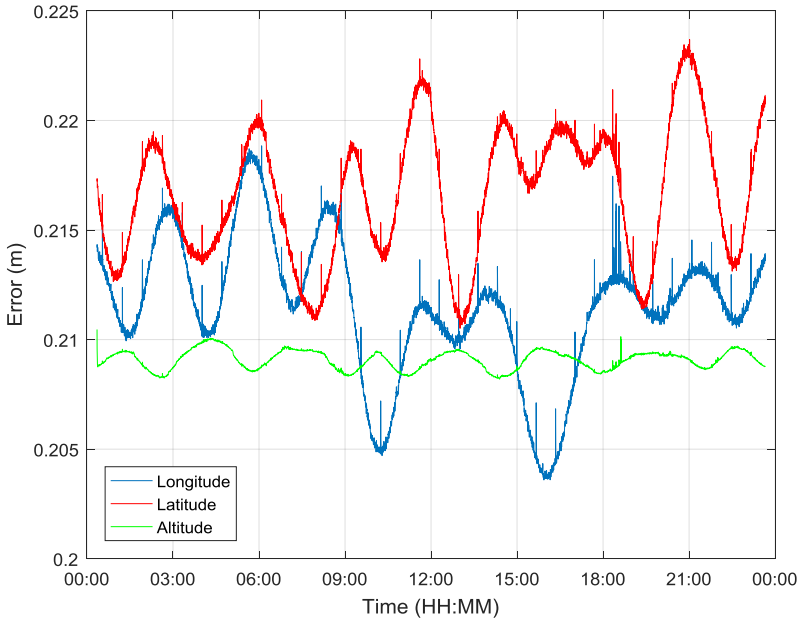

Figure 64. POS MV latitude, longitude, and altitude error estimates after the removal of the large data error estimates present in **Figure 63**.

Table 5. Summary of the statistics for longitude, latitude, and altitude for the recorded data vs. the POS MV estimated errors. The recorded data median, RMS, and confidence intervals are calculated with their mean value subtracted. While the POS MV estimated errors median, RMS, and confidence intervals are calculated with no alteration.

		Longitude (x)	Latitude (y)	Altitude (z)
	Calculated From Data			
From Data	**Mean (degrees)**	-122.26692445	38.09718696	N/A
	Mean (m)	564,277.465	4,216,851.909	-38.434
	Median (m)	-0.001	-0.001	-0.002
	RMS (m)	0.057	0.062	0.055
	CI - 50% (m)	0.039	0.042	0.038
	CI - 95% (m)	0.112	0.122	0.105
	Skew	0.024	0.011	0.000
	Kurtosis	2.938	3.116	2.926
	POS MV Reported Data			
POS MV Estimated Errors	**Mean (m)**	0.212	0.217	0.209
	Median (m)	0.212	0.217	0.209
	RMS (m)	0.212	0.217	0.209
	CI - 50% (m)	0.212	0.217	0.209
	CI - 95% (m)	0.216	0.222	0.210
	Skew	-0.445	-0.016	-0.123
	Kurtosis	3.414	2.158	2.125

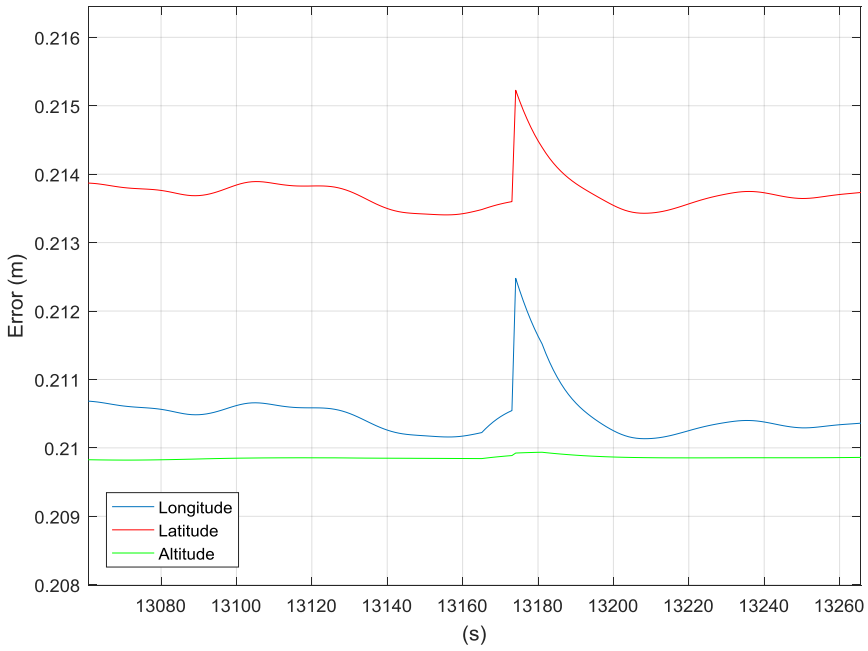

Figure 65. Zoomed in view of one of the small error estimate spikes from **Figure 64**. Spikes take about 15 s to return to their previous values (sample rate is 2 Hz).

The vessels position (longitude, latitude, and altitude) through time is illustrated in **Figure 66 - Figure 68**, respectively. These values are plotted as offsets from their mean position during the 24-hours (**Table 5**). Also, the estimated error bounds (red) (from **Figure 64**) are shown and can be used to see how well the data falls within these limits. Each plot has a few points larger than their respective error estimate. Assuming that the mean position is in fact the true position of the vessel then the error bars do not encompass every data point. While true, the points that are within these red error boundaries consist of 99.98%, 99.94%, and 99.97% of the data for longitude, latitude, and altitude, respectively. With this it is safe to assume that the error estimates provided by POS MV are extreme bounds for all points when using future datasets, but this contradicts the earlier stated specifications of 0.10-0.15 m errors. The difference between the POS MV errors and the smaller errors inferred directly from this (stationary) data will be discussed below.

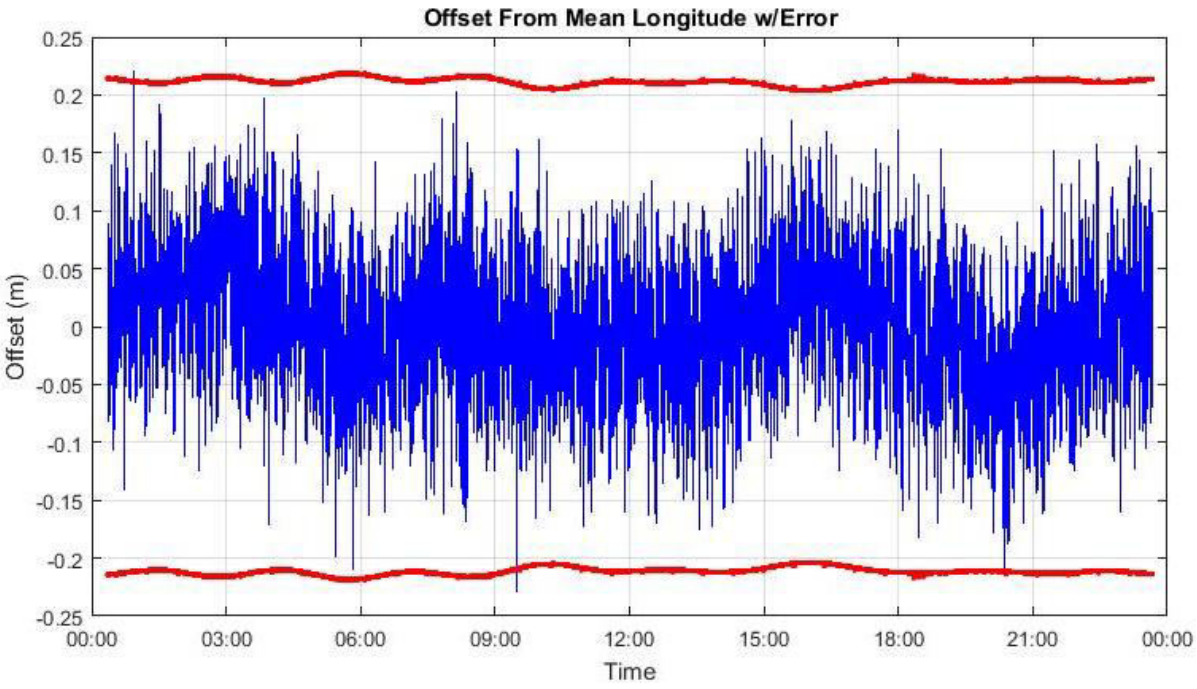

Figure 66. Offset from mean longitude (blue) with POS MV error estimate bounds (red).

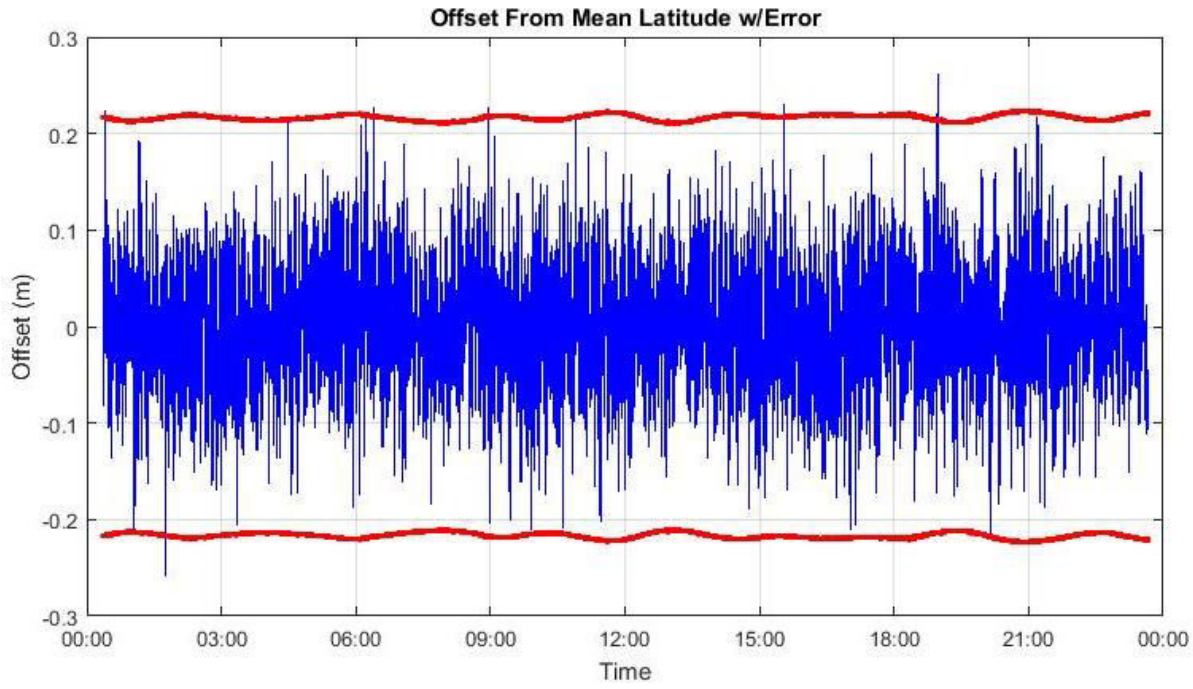

Figure 67. Offset from mean latitude (blue) with POS MV error estimate bounds (red).

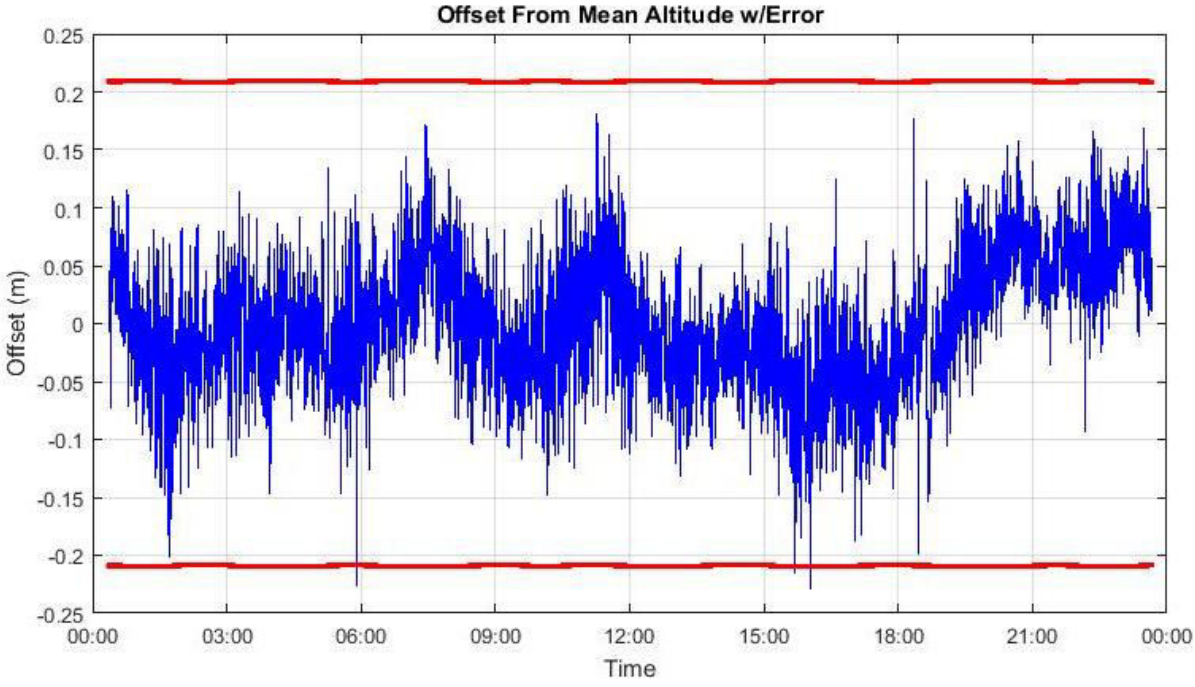

Figure 68. Offset from mean altitude (blue) with POS MV error estimate bounds (red).

Figure 69 shows the vessels latitude and longitude positions in UTM coordinates, where the mean position is 564,277.465 m E 4,216,851.909 m N in zone 10S. The RMS displacement from this mean position during this period was 0.062 m in latitude (y) and 0.057 m in longitude (x), falling well below the POS MV estimated errors seen in **Figure 64**.

Each of these parameters are examined separately to determine their individual statistics (**Figure 70 - Figure 72**). The histogram figures are separated into 410 bins (square root of the number of data points) and are plotted relative to their mean value. Each of them closely follow a normal distribution and a Gaussian function fitted to the data is shown. Two segments are denoted in the figures showing the 50% and 95% confidence intervals (CI), or intervals where 50% and 95% of the data will be located. A root mean square (RMS), median, skew, and kurtosis are given in each figure (also **Table 5**) and are calculated relative to the mean value.

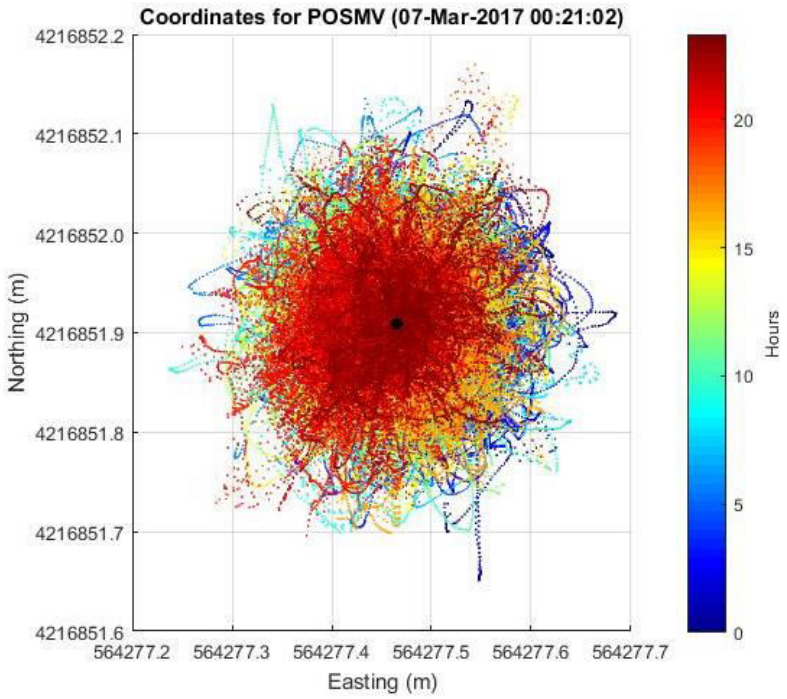

Figure 69. Vessel's surface position through time (color scale) in UTM coordinates for zone 10S. The mean position is highlighted by the black dot and is 564,277.465 m E 4,216,851.909 m N. The UTC time of the first data point is given in the title.

The RMS is computed using

$$RMS = \sigma = \sqrt{\frac{1}{N}\sum_{i=1}^{N}(x_i - \mu)^2} \quad (45)$$

where N is the number of data points in x and μ is the mean of x. The RMS here represents the typical magnitude of the values with respect to the mean, or the standard deviation for the dataset.

The skew (s) and kurtosis (κ) are calculated by

$$s = \frac{E(x-\mu)^3}{\sigma^3} \quad (46)$$

$$\kappa = \frac{E(x-\mu)^4}{\sigma^4} \quad (47)$$

where x represents the data, σ is the standard deviation of x, and E is the expected value of what is inside the parentheses. The skew is a measure of the data's asymmetry about the mean value. If the skew is negative the data is spread out more to the left and vice versa for a positive value. Therefore, data with a normal distribution has zero skew. For kurtosis, data that is normally distributed has a value of 3. Data with a larger kurtosis may indicate outliers, while data with a smaller kurtosis is less likely to have outliers (Westfall 2014). Looking at each of the variables, the kurtosis for latitude is just larger than 3 and is slightly more prone to outliers when compared to the values for longitude and altitude. This is also reflected in their RMS and CI values where latitude is the largest of the three. **Table 5** provides a statistical summary for all three variables.

When comparing the RMS values between the data recorded errors and the POS MV estimated errors, for all three variables, the POS MV provides an overestimate. The ratio between them for x, y, and z is 0.269, 0.286, and 0.263, respectively. For future use of the POS MV data at sea, these ratios will be used to scale the POS MV estimated errors into a RMS error for each direction. For example, if the POS MV estimated errors for x, y, and z are 0.220 m, 0.240 m, and 0.210 m, respectively. Then, (using the ratios above) the expected RMS errors are 0.059 m, 0.069 m, and 0.055 m, respectively.

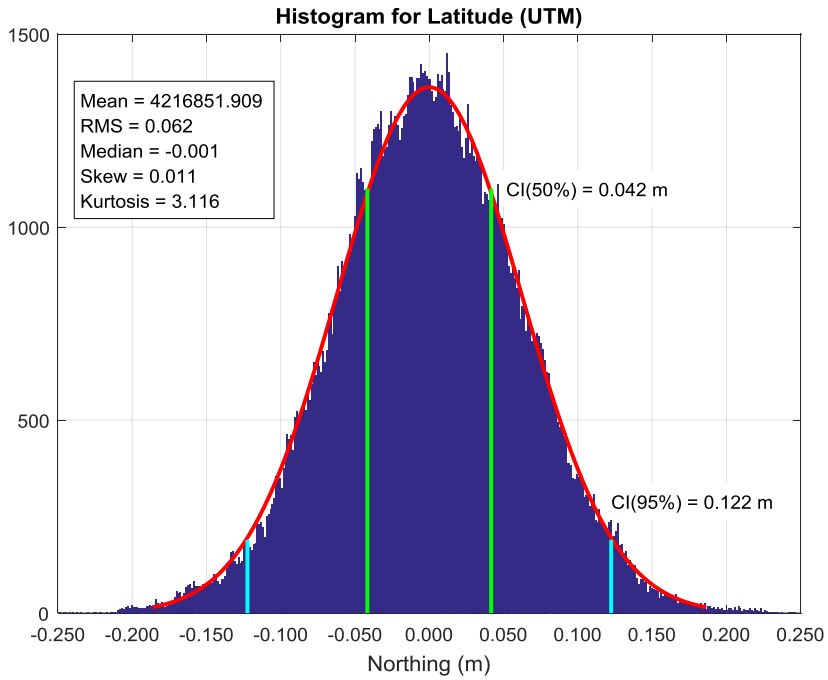

Figure 70. Latitude histogram with a fitted Gaussian function (red) overlaying the data points. The 50% and 95% confidence intervals are given with the green and cyan lines respectively. Statistics are given in the text box.

Figure 73 looks at the vessel's surface displacement in more detail. The mean position from **Figure 69** is used as the origin with all points corresponding to the distance offset from this location. The circular error probability (CEP) is a measure of the data's precision, where 50% of the data points will fall within this circular radius. The CEP was calculated to be just under 0.07 m. Similar to the CEP, R95 corresponds to the circular radius that encompasses 95% of the data points and this was determined to be 0.147 m. The error distribution is nearly circular, because the statistics (RMS, CI's, etc.) of the latitude and longitude are very similar. Also they are both nearly Gaussian, so the ratio between R95 and CEP is expected to be 2.1 according to van Diggelen (2007). The actual ratio between the two is 2.106 and agrees very well with the expected value.

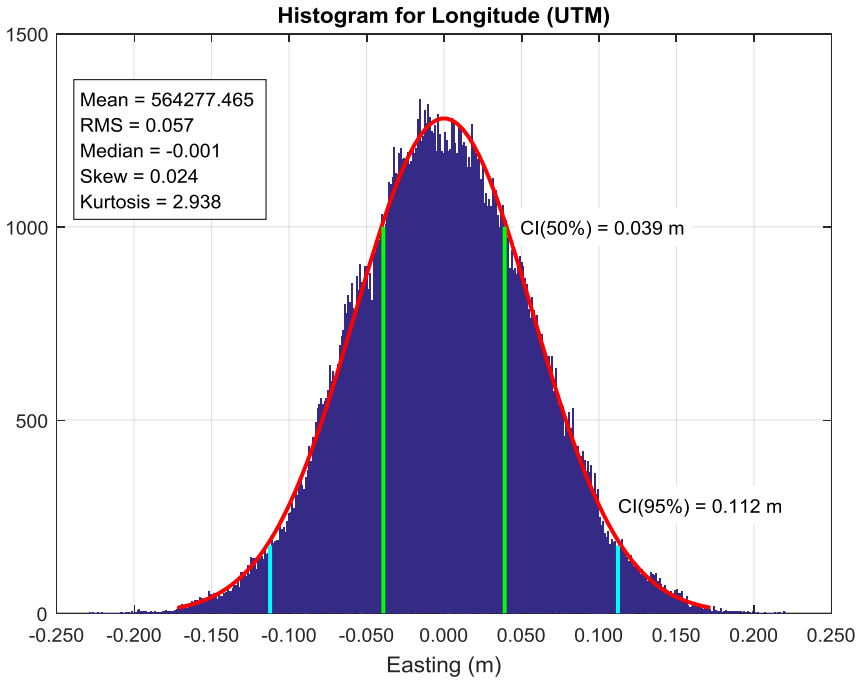

Figure 71. Longitude histogram with a fitted Gaussian function (red) overlaying the data points. The 50% and 95% confidence intervals are given with the green and cyan lines respectively. Statistics are given in the text box.

During this period POS MV was also estimating and logging the position of the transducer array. Over the course of the 24-hours the mean distance between the two positions was calculated to be 19.713 m (agreeing well with previous estimate of 19.69 m). **Figure 74** shows how this distance varied through time when compared to the mean. The POS MV's calculated distance of the two relative to each other is very consistent, with the discrepancies being on the order of less than a micrometer. With this known all the statistics calculated above for the granite block's position can be applied to the transducer.

Figure 75 provides an aerial shot of the dry-dock in San Francisco (Google Earth) with the locations for the granite block and transducer overlaid. It is important to note that at this location the geoid height is 31.881 m below mean sea level. The mean altitude for this dataset with respect to mean sea level is -6.553 m. The R/V *Kilo Moana's* full load draft is 7.6 m and the granite block is about 0.8 m above the bottom of the hull. Therefore, if the vessel was at full load in the water at this location then the granite block should be around 6.8 m below mean sea level.

This number agrees well with the -6.553 m. At ACO, the geoid height is 2.31 m above sea level and is used to convert the altitude measurements relative to mean sea level.

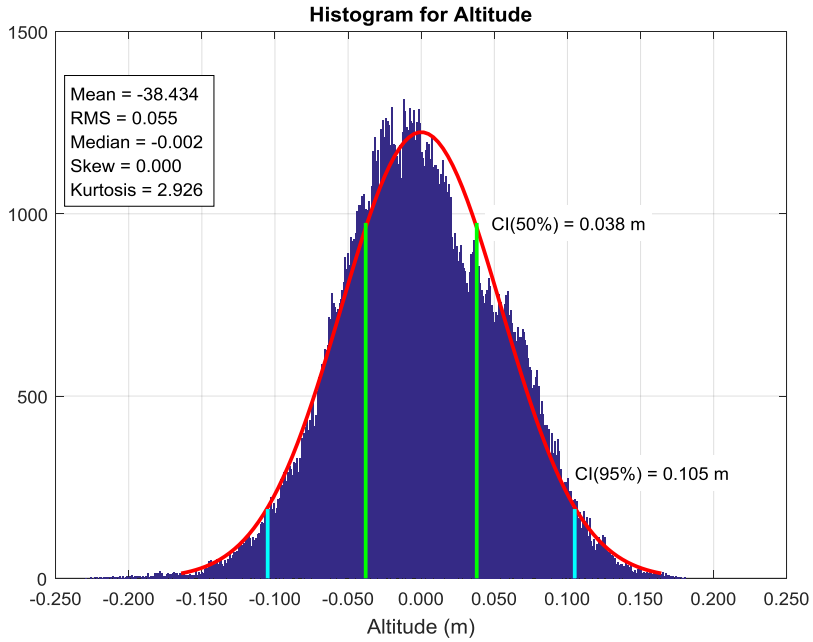

Figure 72. Altitude histogram with a fitted Gaussian function (red) overlaying the data points. The 50% and 95% confidence intervals are given with the green and cyan lines respectively. Statistics are given in the text box.

The next step we would like to take is to use the same antenna but feeding it into two different GPS receivers that are using different correction services. The difference in their positioning estimates will be an exercise to measure their accuracy and precision as well. Another thing to look for is to see whether the error estimate spikes occur again, and if so what could be causing them.

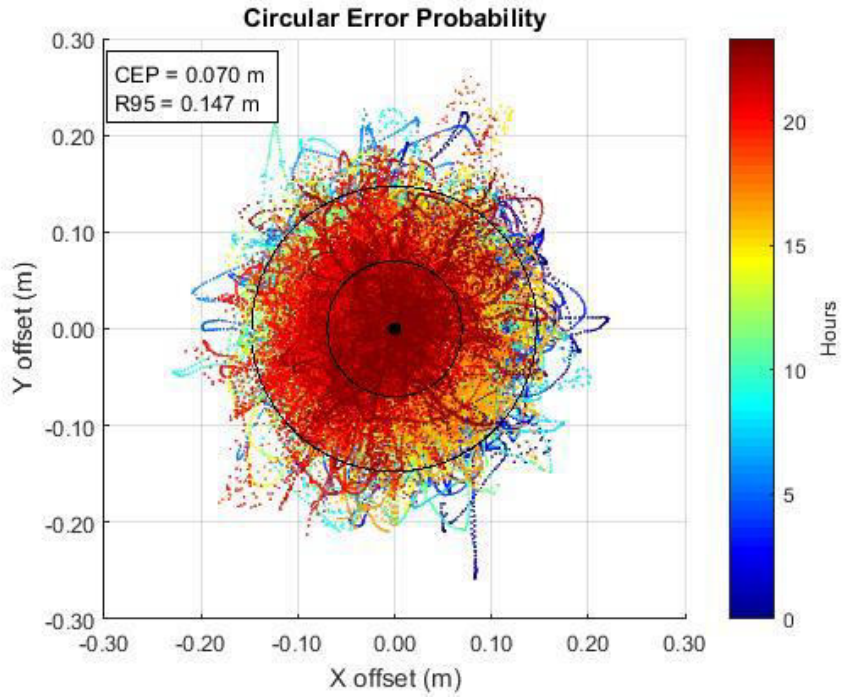

Figure 73. CEP (inner circle) and R95 (outer circle) for the stationary POS-MV data. The color scale shows the vessels position through time.

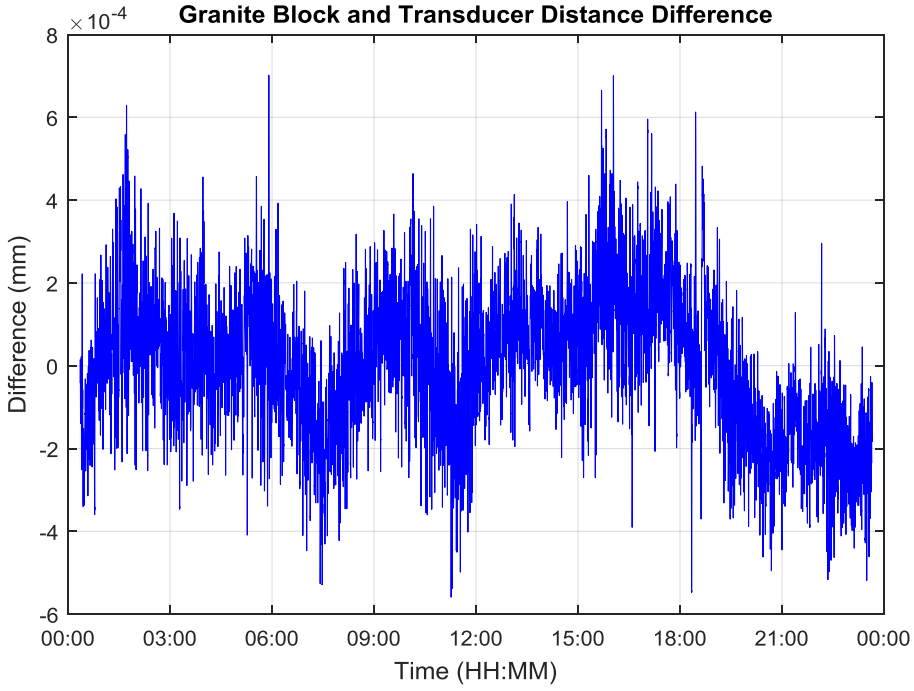

Figure 74. Difference between the granite block and transducer distance from their mean distance of 19.713 m.

Figure 75. Google Earth image of the dry-dock in San Francisco. The mean position of the granite block and transducer is given by the red pins. The bow of the R/V *Kilo Moana* is pointed towards land.

Appendix E. Scarlett 6i6 Specifications

Supported Sample Rates	44.1 kHz, 48 kHz, 88.2 kHz, 96 kHz, 176.4 kHz, 192 kHz
Frequency Response	20 Hz - 20 kHz
Dynamic Range (Input)	110 dB
Maximum Level (Input)	+16 dBu (Inputs 1-2) +22 dBu (Inputs 3-4)
Impedance (Input)	52 kΩ
Dynamic Range (Output)	108 dB
Maximum Level (Output)	+16 dBu
Impedance (Output)	94 Ω

(Focusrite 2017)

Appendix F. Proel HPX2800 Specifications

Power 8 ohm	600 W
Power 4 ohm	1000 W
Power 2 ohm	1400 W
Power BRIDGE 8 ohm	2000 W
Power BRIDGE 4 ohm	2800 W
Frequency Response	20 Hz - 20 kHz
Input Sensitivity (nominal)	0 dBu / 0.775 Vrms
Input Sensitivity (fixed gain)	+ 7.0 dBu / 1.73 Vrms
Gain	39 dB
Dimensions (W x H x D)	19" x 3.5" x 15.6"
Weight	9.2 kg (20.3 lb)

(Proel 2017)

References

Abu-Rgheff, Mosa Ali. *Introduction to CDMA Wireless Communications.* Plymouth: Academic Press, 2007.

Applanix Corporation. "POS MV V5 Installation and Operation Guide." 2016.

Burgmann, Roland, and David Chadwell. "Seafloor Geodesy." *Annual Review of Earth and Planetary Sciences* 42 (2014): 509-534.

Cornuelle, Bruce. "Simulations of Acoustic Tomography Array Performance With Untracked or Drifting Sources and Receivers." *Journal of Geophysical Research* 90 (1985): 9079-9088.

Dushaw, Brian, and John Colosi. *Ray Tracing for Ocean Acoustic Tomography.* Technical Memorandum, Seattle: Applied Physics Laboratory - University of Washington, 1998.

Focusrite. *Scarlett 6i6.* 2017. https://us.focusrite.com/usb-audio-interfaces/scarlett-6i6.

Massa Sonic. "Massa TR-1075 Sub-Bottom Profiling Transducers." Hingham, MA: Massa Products Corporation, 2016.

McDougall, T.J., and P.M. Barker. "Getting started with TEOS-10 and the Gibbs Seawater (GSW) Oceanographic Toolbox." SCOR/IAPSO WG127, 2011.

McGuire, Jeffrey, and John Collins. "Millimeter-level Precision in a Seafloor Geodesy Experiment at the Discovery Transform Fault, East Pacific Rise." *Geochemistry Geophysics Geosystems* 14, no. 10 (2013): 4392-4402.

Medwin, Herman. *Sounds in the Sea - From Ocean Acoustics to Acoustical Oceanography.* Cambridge: Cambridge University Press, 2005.

Munk, Walter, Peter Worcester, and Carl Wunsch. *Ocean Acoustic Tomography.* Cambridge: Cambridge University Press, 1995.

North, Gerald, Thomas Bell, Robert Cahalan, and Fanthune Moeng. "Sampling Errors in the Estimation of Empirical Orthogonal Functions." *Monthly Weather Review* 110, no. 7 (1982): 699-706.

Osada, Yukihito, Motoyuki Kido, Hiromi Fujimoto, and Yoshiyuki Kaneda. "Development of a Seafloor Acoustic Ranging System Toward the Seafloor Cable Network System." *Ocean Engineering* 35 (2008): 1401-1405.

Oxford Technical Solutions. *How Does a GNSS Recevier Work?* March 17, 2017. http://www.oxts.com/.

Proel. *HPX2800.* 2017. http://www.proel.com/index.php?route=product/product&product_id=5936.

Rihaczek, August. *Principles of High-Resolution Radar.* Loa Altos: Peninsula Publishing, 1985.

Spiess, Fred, David Chadwell, John Hildebrand, Larry Young, George Purcell, and Herb Dragert. "Precise GPS/Acoustic Positioning of Seafloor Reference Points for Tectonic Studies." *Physics of the Earth and Planetary Interiors* 108 (1998): 101-112.

Tarantola, Albert. *Inverse Problem Theory.* Netherlands: Elsevier Science Publishers, 1987.

van Diggelen, Frank. "GNSS Accuracy – Lies, Damn Lies and Statistics." *GPS World* 18 (2007): 26-32.

Van Uffelen, Lora, Bruce Howe, Eva-Marie Nosal, Glenn Carter, Peter Worcester, and Matthew Dzieciuch. "Localization and Subsurface Position Error Estimation of Gliders Using Broadband Acoustic Signals at Long Range." *IEEE Journal of Oceanic Engineering* 41, no. 3 (2016): 501-508.

Visser, Hans, Dariusz Lapucha, Javier Tegedor, Ole Ørpen, and Yahya Memarzadeh. *GNSS Improvements for Offshore Applications.* Houston: FUGRO, 2016.

Westfall, Peter. "Kurtosis as Peakedness, 1905–2014. R.I.P." *The American Statistician* 68 (2014): 191-195.

Wikipedia. *Satellite Navigation.* March 17, 2017. https://en.wikipedia.org/wiki/Satellite_navigation.